THE PHASE GRADIENT AUTOFOCUS ALGORITHM WITH RANGE DEPENDENT STRIPMAP SAR

by

James S. Bates

A thesis submitted to the faculty of

Brigham Young University

in partial fulfillment of the requirements for the degree of

Master of Science

Department of Electrical and Computer Engineering

Brigham Young University

December 1998

Copyright © 1998 James S. Bates

All Rights Reserved

BRIGHAM YOUNG UNIVERSITY

GRADUATE COMMITTEE APPROVAL

of a thesis submitted by

James S. Bates

This thesis has been read by each member of the following graduate committee and by majority vote has been found to be satisfactory.

19 Oct. 1998
Date

David Arnold, Chair

16 Oct 1998
Date

David Long

19 Oct 1998
Date

Brian Jeffs

BRIGHAM YOUNG UNIVERSITY

As chair of the candidate's graduate committee, I have read the thesis of James S. Bates in its final form and have found that (1) its format, citations, and bibliographical style are consistent and acceptable and fulfill university and department style requirements; (2) its illustrative materials including figures, tables, and charts are in place; and (3) the final manuscript is satisfactory to the graduate committee and is ready for submission to the university library.

19 Oct. 1998
Date

David V. Arnold
David Arnold
Chair, Graduate Committee

Accepted for the Department

Michael D. Rice
Graduate Coordinator

Accepted for the College

Douglas M Chabries
Douglas M. Chabries
Dean, College of Engineering and Technology

ABSTRACT

THE PHASE GRADIENT AUTOFOCUS ALGORITHM WITH RANGE DEPENDENT STRIPMAP SAR

James S. Bates

Department of Electrical and Computer Engineering

Master of Science

The Phase Gradient Autofocus (PGA) algorithm is widely used in spotlight mode SAR for motion compensation. The Maximum Likelihood PGA (ML PGA) algorithm has been shown to be a superior autofocus method. The PGA is restricted to high altitude aircraft. Since lower altitude SARs have significant range dependencies that cannot be ignored, the PGA could not be used. This thesis eliminates the high altitude restriction and extends the PGA for use with all spotlight SARs. The new algorithm is tested with three images. Each image has a unique quality. A desert image provides a low signal to clutter ratio with no distinct targets. An urban image tests the ability to focus bright close proximity targets and the mountain image has ares with high signal-to-clutter and areas with low signal-to-clutter. Each image was corrupted with a low frequency and high frequency motion induced low altitude phase error. The new Phase Weighted Estimation (PWE) low altitude autofocus method converged to a lower standard deviation than the ML PGA, but required more iterations.

Another limitation of the PGA is that it will only work for spotlight SAR. In this thesis, the spotlight PGA is extended to stripmap by using a conversion similar to spotlight mode. With the space frequency relationship an altered PGA is used to extend the PGA to stripmap mode SAR. The stripmap SAR, range dependant PGA allows for focusing of low altitude low cost stripmap SARs. The phase weighted estimation method is extended to range dependent stripmap. The stripmap mode estimator is most successful with high signal-to-noise images.

ACKNOWLEDGMENTS

I would like to thank everyone that has put up with me in the last few years while I have been killing myself going to school. In addition I want to thank Dr. Arnold who has been a friend as well as an adviser, and Doug Thompson who has always been willing to explain a concept or help with code. I owe great thanks to my wife. Without her patience and sacrifice I could have never succeeded. I would also like to thank all the faculty that I have dealt with over my four years at BYU. The game is now over.

Contents

Acknowledgments vii

List of Figures xvi

1 Introduction 1

1.1 Stripmap and Spotlight SAR 2

1.2 Spotlight Autofocus Algorithms 4

1.3 Range Dependent Errors: Phase Weighted Estimation 5

1.4 Stripmap SAR Phase Error Estimation 5

1.5 Contributions 5

2 Stripmap and Spotlight SARs 7

2.1 Real Aperture Radar: 8

2.1.1 LFM Chirp 8

2.1.2 Using the LFM Chirp in Real Aperture Radar with Range Compression 9

2.2 Synthetic Aperture Radar 11

2.3 Stripmap SAR 12

2.4 Spotlight Synthetic Aperture Radar 16

3 Spotlight Autofocus Algorithms and Phase Gradient Autofocus 21

3.1 Complex Shift 24

3.2 Windowing 25

3.3 Phase Gradient Estimation 26

3.3.1 Eigenvector Method 26

3.3.2 Maximum Likelihood 28

3.4 Iteration 29
3.5 Maximum Likelihood Results 30
3.5.1 Desert Image: No Significant Scatterers 31
3.5.2 Mountain Image: Some Significant Scatterers 33
3.5.3 Urban Image: Many Significant Scatterers 35

4 Range Dependent Error and Phase Weighted Estimation **39**
4.1 Range Dependent Geometry and Motion 39
4.2 Phase Weighted Estimation 42
4.3 Phase Weighted Estimation Results 48
4.3.1 Desert Image: No Significant Scatterers 50
4.3.2 Mountain Image: Some Significant Scatterers 53
4.3.3 Urban Image: Many Significant Scatterers 56

5 Stripmap Phase Estimation **63**
5.1 Alternative Stripmap Azimuth Compression Method 63
5.1.1 Create Sections (Step 1) 65
5.1.2 Chirp Multiplication (Step 2) 66
5.1.3 Fourier Transform (Step 3) 67
5.2 Applying the PWE PGA 69
5.3 Stripmap Results 70
5.3.1 Desert Image: No Significant Scatterers 74
5.3.2 Mountain Image: Some Significant Scatterers 78
5.3.3 Urban Image: Many Significant Scatterers 82

6 Conclusions **89**
6.1 Summary of Contributions 89
6.2 Future Research 90

Bibliography **92**

List of Figures

1.1 SAR Geometry Phase History Comparison 3
2.1 LFM Chirp. β is the slope of the line. 8
2.2 SAR Geometry 10
2.3 Stripmap SAR Geometry 12
2.4 Normalized Azimuth Chirp Phase 15
2.5 Azimuth Chirp of target located at the 270^{th} pixel 16
2.6 Stripmap, Spotlight SAR Geometry Comparison 17
2.7 Example Antenna hardware 18
3.1 Range Dependent SAR Geometry 22
3.2 PGA Steps 23
3.3 Example of the steps of the PGA 25
3.4 Original Desert Image 31
3.5 Phase Corrupted Desert Image 31
3.6 Restored ML Desert Image 32
3.7 Maximum likelihood phase error plot (Desert Scene, No Distinct Targets) 32
3.8 Maximum Likelihood Standard Deviation (Desert Scene, No Distinct Targets) 32
3.9 Original Mountain Image 33
3.10 Phase Corrupted Mountain Image 33
3.11 Restored ML Mountain Image 34
3.12 Maximum likelihood phase error plot (Mountain Image, Distributed Targets) 34
3.13 Maximum Likelihood Standard Deviation (Mountain Image, Distributed Targets) 34

3.14 Spotlight Urban Image 35
3.15 Spotlight Phase Corrupted Urban Image 35
3.16 Restored ML Urban Image 36
3.17 Maximum Likelihood Phase Error (Urban Image, Close Bright Targets) 36
3.18 Maximum Likelihood Standard Deviation (Urban Image, Close Bright Targets) 36
3.19 Maximum Likelihood High Frequency Phase Error (Urban Image, Close Bright Targets) 37
3.20 Maximum Likelihood High Frequency Standard Deviation (Urban Image, Close Bright Targets) 37
4.1 Range Dependent SAR Geometry 40
4.2 Transverse Motion Geometry 41
4.3 Relationship between SNR and Standard deviation 43
4.4 NRD-PWE, ML Phase Comparison (Desert Image) 50
4.5 NRD-PWE, ML Standard Deviation (Desert Image) 50
4.6 RD-PWE Phase Comparison X (Desert Image) 50
4.7 RD-PWE Standard Deviation X (Desert Image) 50
4.8 RD-PWE Phase Comparison Y (Desert Image) 51
4.9 RD-PWE Standard Deviation Y (Desert Image) 51
4.10 RD-PWE Phase Comparison Range Bin (1) (Desert Image) 51
4.11 RD-PWE Standard Deviation Range Bin (1) (Desert Image) 51
4.12 RD-PWE Phase Comparison Range Bin (300) (Desert Image) 52
4.13 RD-PWE Standard Deviation Range Bin (300) (Desert Image) 52
4.14 RD-PWE Phase Comparison Range Bin (500) (Desert Image) 52
4.15 RD-PWE Standard Deviation Range Bin (500) (Desert Image) 52
4.16 NRD-PWE, ML Phase Comparison (Mountain Image) 53
4.17 NRD-PWE, ML Standard Deviation (Mountain Image) 53
4.18 RD-PWE Phase Comparison X(Mountain Image) 53
4.19 RD-PWE Standard Deviation X(Mountain Image) 53
4.20 RD-PWE Phase Comparison Y (Mountain Image) 54

4.21 RD-PWE Standard Deviation Y (Mountain Image) 54
4.22 RD-PWE Phase Comparison Range Bin (1) (Mountain Image) 54
4.23 RD-PWE Standard Deviation Range Bin (1) (Mountain Image) . . . 54
4.24 RD-PWE Phase Comparison Range Bin (300) (Mountain Image) . . 55
4.25 RD-PWE Standard Deviation Range Bin (300) (Mountain Image) . . 55
4.26 RD-PWE Phase Comparison Range Bin (500) (Mountain Image) . . 55
4.27 RD-PWE Standard Deviation Range Bin (500) (Mountain Image) . . 55
4.28 NRD-PWE, ML Phase Comparison (Urban Image) 56
4.29 NRD-PWE, ML Standard Deviation (Urban Image) 56
4.30 RD-PWE Phase Comparison X (Urban Image) 56
4.31 RD-PWE Standard Deviation X (Urban Image) 56
4.32 RD-PWE Phase Comparison X (Urban Image) 57
4.33 RD-PWE Phase Comparison Y (Urban Image) 57
4.34 RD-PWE Phase Range Comparison Bin (1) (Urban Image) 57
4.35 RD-PWE Standard Deviation Range Bin (1) (Urban Image) 57
4.36 RD-PWE Phase Range Comparison Bin (300) (Urban Image) 58
4.37 RD-PWE Standard Deviation Range Bin (300) (Urban Image) 58
4.38 RD-PWE Phase Range Comparison Bin (500) (Urban Image) 58
4.39 RD-PWE Standard Deviation Range Bin (500) (Urban Image) 58
4.40 Spotlight NRD-PWE, ML High Frequency Phase Comparison (Urban Image) 59
4.41 Spotlight NRD-PWE, ML High Frequency Standard Deviation (Urban Image) 59
4.42 Spotlight RD-PWE High Frequency Phase Comparison X (Urban Image) 59
4.43 Spotlight RD-PWE High Frequency Standard Deviation X (Urban Image) 59
4.44 Spotlight RD-PWE High Frequency Phase Comparison X (Urban Image) 60
4.45 Spotlight RD-PWE High Frequency Phase Comparison Y (Urban Image) 60
4.46 Spotlight RD-PWE High Frequency Phase Range Comparison Bin (1) (Urban Image) 60

4.47 Spotlight RD-PWE High Frequency Standard Deviation Range Bin (1) (Urban Image) 60
4.48 Spotlight RD-PWE High Frequency Phase Range Comparison Bin (300) (Urban Image) 61
4.49 Spotlight RD-PWE High Frequency Standard Deviation Range Bin (300) (Urban Image) 61
4.50 Spotlight RD-PWE High Frequency Phase Range Comparison Bin (500) (Urban Image) 61
4.51 Spotlight RD-PWE High Frequency Standard Deviation: Range Bin (500) (Urban Image) 61
5.1 SAR Geometry Phase history Comparison 64
5.2 Urban Conventional Stripmap Compression 68
5.3 Urban New Stripmap Compression Method 69
5.4 Urban New Stripmap Compression Method Range Dependent Chirp . 70
5.5 Steps of Stripmap Phase Estimation 72
5.6 First Derivative Discontinuities 73
5.7 Stripmap Range Dependent Phase Corrupted Desert Image 74
5.8 Restored Stripmap PWE RD Desert Image 74
5.9 NRD-SPWE Phase Comparison (Desert Image) 75
5.10 NRD-SPWE Standard Deviation (Desert Image) 75
5.11 NRD-SPWE Phase Comparison (Desert Image) 75
5.12 NRD-SPWE Standard Deviation (Desert Image) 75
5.13 RD-SPWE Phase Comparison X (Desert Image) 76
5.14 RD-SPWE Phase Comparison Y (Desert Image) 76
5.15 RD-SPWE Phase Comparison Range Bin (1) (Desert Image) 76
5.16 RD-SPWE Standard Deviation Range Bin (1) (Desert Image) 76
5.17 RD-SPWE Phase Comparison Range Bin (300) (Desert Image) 77
5.18 RD-SPWE Standard Deviation Range Bin (300) (Desert Image) . . . 77
5.19 RD-SPWE Phase Comparison Range Bin (500) (Desert Image) 77
5.20 RD-SPWE Standard Deviation Range Bin (500) (Desert Image) . . . 77

5.21 Stripmap Range Dependent Phase Corrupted Mountain Image 78
5.22 Restored Stripmap Range Dependent PWE Mountain Image 78
5.23 NRD-SPWE Phase Comparison (Mountain Image) 79
5.24 NRD-SPWE Standard Deviation (Mountain Image) 79
5.25 NRD-SPWE Phase Comparison (Mountain Image) 79
5.26 NRD-SPWE Standard Deviation (Mountain Image) 79
5.27 RD-SPWE Phase Comparison X (Mountain Image) 80
5.28 RD-SPWE Phase Comparison Y (Mountain Image) 80
5.29 RD-SPWE Phase Comparison Range Bin (1) (Mountain Image) . . . 80
5.30 RD-SPWE Standard Deviation Range Bin (1) (Mountain Image) . . 80
5.31 RD-SPWE Phase Comparison Range Bin (300) (Mountain Image) . . 81
5.32 RD-SPWE Standard Deviation Range Bin (300) (Mountain Image) . 81
5.33 RD-SPWE Phase Comparison Range Bin (500) (Mountain Image) . . 81
5.34 RD-SPWE Standard Deviation Range Bin (500) (Mountain Image) . 81
5.35 Stripmap Range Dependent Phase Corrupted Urban Image 82
5.36 Restored Stripmap Range Dependent PWE Urban Image 82
5.37 NRD-SPWE Phase Comparison (Urban Image) 83
5.38 NRD-SPWE Standard Deviation (Urban Image) 83
5.39 NRD-SPWE Phase Comparison (Urban Image) 83
5.40 NRD-SPWE Standard Deviation (Urban Image) 83
5.41 RD-SPWE Phase Comparison X (Urban Image) 84
5.42 RD-SPWE Phase Comparison Y (Urban Image) 84
5.43 RD-SPWE Phase Range Comparison Bin (1) (Urban Image) 84
5.44 RD-SPWE Standard Deviation Range Bin (1) (Urban Image) 84
5.45 RD-SPWE Phase Range Comparison Bin (300) (Urban Image) 85
5.46 RD-SPWE Standard Deviation Range Bin (300) (Urban Image) . . . 85
5.47 RD-SPWE Phase Range Comparison Bin (500) (Urban Image) 85
5.48 RD-SPWE Standard Deviation Range Bin (500) (Urban Image) . . . 85
5.49 NRD-SPWE High Frequency Phase Comparison (Urban Image) . . . 86
5.50 NRD-SPWE High Frequency Standard Deviation (Urban Image) . . . 86

5.51 NRD-SPWE High Frequency Phase Comparison (Urban Image) . . . 86
5.52 NRD-SPWE High Frequency Standard Deviation (Urban Image) . . . 86
5.53 RD-SPWE High Frequency Phase Comparison X (Urban Image) . . . 87
5.54 RD-SPWE High Frequency Phase Comparison Y (Urban Image) . . . 87
5.55 RD-SPWE High Frequency Phase Range Comparison Bin (1) (Urban Image) . . . 87
5.56 RD-SPWE High Frequency Standard Deviation Range Bin (1) (Urban Image) . . . 87
5.57 RD-SPWE High Frequency Phase Range Comparison Bin (300) (Urban Image) . . . 88
5.58 RD-SPWE High Frequency Standard Deviation Range Bin (300) (Urban Image) . . . 88
5.59 RD-SPWE High Frequency Phase Range Comparison Bin (500) (Urban Image) . . . 88
5.60 RD-SPWE High Frequency Standard Deviation Range Bin (500) (Urban Image) . . . 88

Chapter 1

Introduction

Movement in aircraft has been a major cause of phase errors in radar images since the introduction of Synthetic Aperture Radar (SAR) more than thirty years ago. The history of SAR is discussed in detail in two books written by Walter G. Carrara and Ron S. Goodman and Ronald M. Majewski [1], and Charles V. Jakowatz and Daniel E. Wahl and Paul H. Eichel and Dennis C. Ghiglia and Paul A. Thompson [2]. The Phase Gradient Autofucus (PGA) helps correct phase errors. This paper expands the PGA algorithm originally developed by P. H. Eichel and C. V. Jakowatz, Jr. [3] [4] from its restriction to high altitude spotlight SARs, to low altitude stripmap SAR. This expansion is made in two steps.

The first step introduces range dependent phase errors into spotlight SAR. When SARs are flown at low altitudes, the change in look angles from the farthest range point to the nearest range point becomes significant. The assumption of having constant phase errors in all range bins [3] [4] used in the PGA becomes invalid. A new estimation step produces an algorithm capable of estimating a range dependent, two parameter phase error. This algorithm is introduced as Phase Weighted Estimation (PWE).

The next step is extending the algorithm to stripmap data. This step has been attempted once before by C. V Jakowatz, Jr. [5]. Dr. Jakowatz did not attempt range dependent images. A different approach, with a new stripmap to spotlight converter and altered PGA, produces an estimator that is capable of estimating phase error functions in stripmap, and spotlight SAR. This estimator is easily extended to low and high altitude phase errors. In the following sections I will present tutorial

information and giva an outline of this thesis.

1.1 Stripmap and Spotlight SAR

Chapter 2 discusses the basics of stripmap and spotlight SAR. Synthetic Aperture Radar (SAR) has become a widely used remote imaging technique. Recent advances in radio frequency devices, analog to digital converters, computers and digital signal processors have made high resolution SAR possible at a lower cost. SARs do not need optical illumination and have the unique ability to penetrate foliage, sand or soil as demenstrated by D. W. Holcomb [6]. Using the advantages of SAR, many useful applications have been developed in many research areas. These applications generally require very high resolution.

SARs are carried aboard constant velocity moving transport vehicles. SARs use the induced phase change from the radar back scatter, to compress, or create an image by signal processing methods as discussed in detail by David C. Munson, JR. and Robert L. Visentin [7]. Much like a blurred photogragh to moving a camera while taking a picture, the resultant SAR image is blurred by unknown movements of the carrying device, known as the radar platform. When a unknown phase change caused by non-uniform platform motion, is present in the collected data, the image is not created properly and is de-focused. Movements in the SAR platform create phase errors in the image [1]. These phase errors limit the resolution.

Spotlight and stripmap SAR are similar in that they both use a known phase history to create images. However, the acquisition and processing of the data are quite different for these two modes. Spotlight SAR uses a movable antenna that is steered to illuminate a single stationary spot on the ground for the entire acquisition time. The known phase change chirp, caused by the moving antenna, usually contains a bandwidth that is too wide to be sampled directly because of the long exposure time. In this case the azimuth chirp is frequently removed with high frequency hardware. The cost of the steerable antenna and dechirp hardware make the spotlight SAR quite expensive and difficult to implement in low cost systems. The processing required to create the spotlight image is the Fourier transform of the received dechirped data

[1]. Thus, the phase history of the spotlight image is contained in the inverse Fourier transform of the image. This relationship between the image and the phase history is key to the application of the PGA.

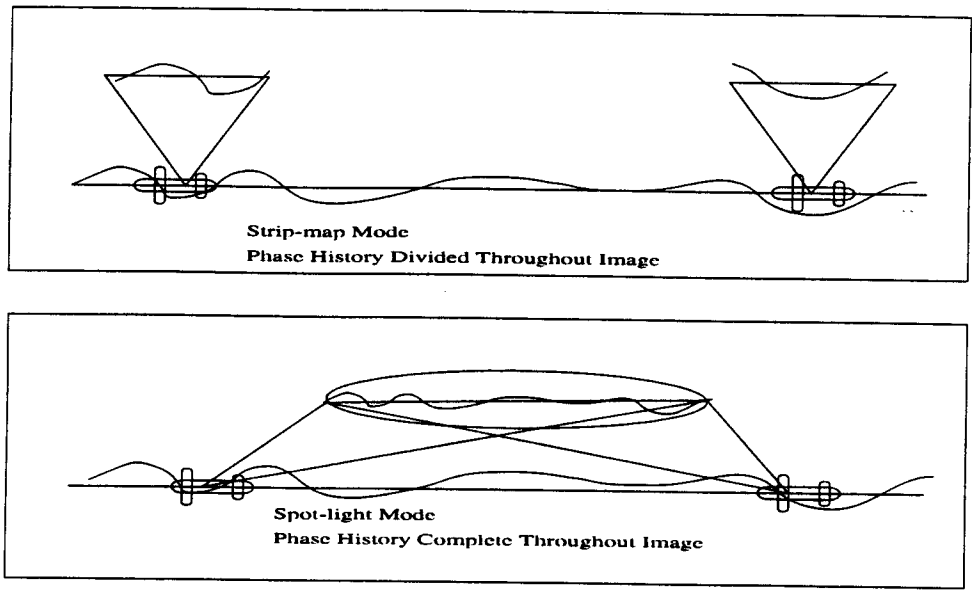

Figure 1.1: SAR Geometry Phase History Comparison

Stripmap SAR does not have a movable antenna [7], and the illuminated area changes during acquisition as shown in Fig. 1.1. With a shorter illumination time the stripmap SAR generally has a narrower bandwidth. Additionally, the chirp is not centered on a stationary point, making it difficult to remove the chirp in hardware. For these reasons the data is generally sampled directly. Stripmap SAR systems have been shown to create reasonable images at low cost by D. G. Thompson and D. V. Arnold [8]. Stripmap SAR is mechanically and electronically easier to configure, maintain and use than spotlight SAR [1]. The image formation processing consists of a calculated expected chirp convolved with each range line of data to compress and create an image. With the fully compressed image data and the range compressed data both referenced to the time domain, (as opposed to the fully compressed image data

in Frequency domain as in the spotlight case) the PGA cannot be applied directly.

1.2 Spotlight Autofocus Algorithms

To obtain high resolution images, the effects due to vibrations and movements of the radar platform must be removed. In most systems an inertial navigational unit (INU) is used to measure the movement of the platform [1]. Although these devices measure the general motions of the radar platform (generally an aircraft), they do not account for all of the movement and vibration that takes place at the antenna. Other phase errors, including electromagnetic propagation and atmospheric effects that are unmeasurable with an INU also degrade the resolution. To obtain the highest resolution, all movement and other phase errors must be compensated for in the final image. Three main algorithms have been developed to remove these phase. The first algorithm is referred to as inverse filtering [2] and uses bright known targets to sharpen the whole image using the bright target as a reference. The second algorithm is called map drift [2] and models the phase errors as being a low order polynomial. This method restricts the errors that may be compensated. Both of these methods have met with limited success, due mainly to the limited images and SAR types that may be used with them.

The third method is image-independent, and is called the Phase Gradient Autofocus (PGA) Algorithm [4]. The term autofocus refers to the ability of the algorithm to focus the image using only the data itself. The PGA has been shown to be a very robust algorithm that can estimate errors found in urban images with bright close targets, or an image with no bright targets such as a desert. The PGA does not use a phase error model so both high and low order phase errors may be estimated accurately. The PGA was originally developed for spotlight SAR and has been very successful.

In this thesis the four main steps in the PGA algorithm are all used in the range dependent stripmap model [4][3]. The four steps defined in this thesis are center shifting, windowing, phase estimation and iteration.

1.3 Range Dependent Errors: Phase Weighted Estimation

The PGA has also been used extensively in high flying aircraft, but never in low altitude systems because the PGA makes the narrow beam assumption. This approximation assumes that the range look angle does not change significantly over the image. Low altitude spotlight or stripmap SARs can not use this algorithm. The contribution of this thesis is the development of a more general PGA that may be used with all images regardless of the SAR system and altitude used. The Phase Weighted Estimation PGA (PWE PGA) proposed here differs from the original PGA primarily in the phase estimation step.

1.4 Stripmap SAR Phase Error Estimation

The PGA has never (until now) successfully been ported to range dependent or stripmap SAR. Stripmap to spotlight converters have been developed in the past by Yeo TS, Tan NL, Lu YH and Zhang CB [9] and M. Soumekh [10]. These algorithms are complicated and can not be easily used with range dependent data. A new compression algorithm will compress stripmap SAR images to give a spotlight like frequency-space relationship. With this compression used, the stripmap image data may used with an altered PWE PGA autofocus algorithm. The altered PWE PGA differs only in the circular shift step. The results for the derivation of the range dependent stripmap PGA are shown and compared with those of the conventional PGA. The results show that the phase error is estimated comparably to spotlight non-range systems.

1.5 Contributions

The contributions of this thesis include; the derivation of the low altiude SAR model, deriving the phase error estimator at low range called Phase Weighted Estimation, expanding the PGA to stripmap, and expanding the Phase Weighted Estimation to low altitude stripmap. These contributions are discussed more in the conclusion section.

Chapter 2

Stripmap and Spotlight SARs

Since the early 1930's, radar has been used to find a target's location, speed and heading. The resolution of a radar system is defined in the azimuth and range directions. In the early 1950's Carl Wiley first developed the concept of processing normal radar data to achieve high resolution at the, Goodyear Aircraft Corporation [2]. Wiley called these resolution enhancement techniques "Doppler beam sharpening". Today these ideas are called Synthetic Aperture Radar (SAR).

Since it's conception, many uses for SAR have been found. Much of the funding for SAR research is found in three areas. These three areas are military, environmental and topographical. SAR was originally developed as an all-weather, day or night imaging system. The military originally funded development of SAR imaging systems for the reconnaissance, surveillance and targeting of enemy weapons. Throughout this development, different types of SAR were developed, each with its own advantages and disadvantages. The two types that will be discussed here are stripmap and spotlight. Stripmap was introduced in the early 1950's by Wiley and spotlight was first introduced by Walker in 1980 [2]. In the 1980's, environmental uses of SAR systems started to expand. Uses such as finding oil spills, measuring rain forest acreage, and other measuring of changing environmental effects have become widespread. Using two receiving antennae, the z-axis can be resolved by comparing the phase of both images. The resulting images can have sub-meter resolution in all three dimensions making very accurate topographical maps. SAR also has the ability to see through foliage and dry sand. Archaeologists have found it to be a very useful tool [8].

2.1 Real Aperture Radar:

Real Aperture Radar (RAR) is the precessor to SAR. RARs range realization generally use a Linear Frequency Modulated (LFM) chirp to increase the bandwidth. The definition of the LFM chirp, with the mathematical model [11] is given below.

2.1.1 LFM Chirp

A pulsed LFM signal sent from the RADAR is called a chirp. The frequency / time relationship of a LFM chirp is shown in Fig. 2.1 and is described by

$$LFM(t) = cos(\beta t^2) \qquad 0 < t < T. \tag{2.1}$$

β is the 'chirp rate' and is defined as the rate at which the frequency increases. From

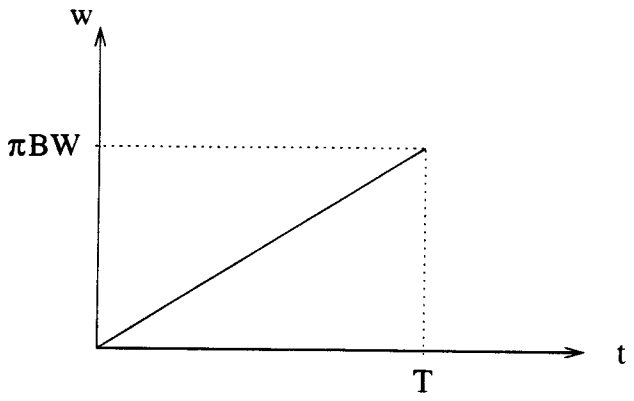

Figure 2.1: LFM Chirp. β is the slope of the line.

Eq. (2.1) it can be seen that the phase of the chirp is given by $\theta = \beta t^2$. The frequency is determined by $\theta' = 2\beta t$. The LFM chirp bandwidth, BW, is determined by the maximum θ', which occurs at $t = T$, to give $BW = 2\beta t$. Solving for β in radians where BW is in Hz yields

$$\beta = \frac{BW\pi}{T}. \tag{2.2}$$

β is graphically illustrated in Fig. 2.1 where β is the slope of the line.

2.1.2 Using the LFM Chirp in Real Aperture Radar with Range Compression

The LFM chirp is mixed with the RF signal and then sent. The received signal can be modeled as a time delayed, attenuated signal of the original chirp. Let the range distance and amplitude of a given return be represented by the distance $R_0 = \frac{t_o c}{2}$ and amplitude A_k. The received signal is then

$$r(t) = A_k \frac{1}{2} \left(\cos\left[w_c(t - t_0) - \beta(t - t_o)^2\right] + \cos\left[w_c(t - t_o) + \beta(t - t_o)^2\right] \right). \quad (2.3)$$

The return signal is then base banded, filtered and the real and imaginary parts are extracted using a Hilbert transform. The resulting equation is

$$\begin{aligned} & \frac{1}{4} A_k \left(\underbrace{\exp\left[jw_o t - j\beta(t - t_o)^2 - jw_c t_o\right]}_{A} + \underbrace{\exp\left[jw_o t + j\beta(t - t_o)^2 - jw_c t_o\right]}_{B} \right) \\ = \; & \frac{1}{4}(A + B). \end{aligned} \quad (2.4)$$

Range is resolved using a matched filter approach. The received signal is correlated with the original LFM chirp. Fast Fourier transform techniques are usually used to reduce computations in this process. The correlation is the same as the convolution function with the time of one of the terms negated. The results give a *sinc* function centered at $t = t_0$. The derivation is seen below (for details see [11]).

$$h(t) = \underbrace{\exp(jw_o t - j\beta t^2)}_{C} + \underbrace{\exp(jw_o t + j\beta t^2)}_{D} \quad (2.5)$$

$$= C + D \quad (2.6)$$

$$g(t) = s(t) \otimes h^*(t) \quad (2.7)$$

$$\mathcal{F}(g(t)) = G(w) = S(w)H(-w) \quad (2.8)$$

$$g(t) = \int_{-\infty}^{\infty} s(t + \tau) h^*(\tau) d\tau \quad (2.9)$$

$$g(t) \simeq \int AC + BD \quad (2.10)$$

$$= A_k 2T \exp(-jw_c t_o + jw_o t) sinc[\beta T(t - t_o)] cos[\beta T(t - t_o) - \beta(t - t_o)^2]$$

$$\beta = \frac{\tau\beta}{T} \quad (2.11)$$

This process is called compression. In the range direction the *sinc* function in Eq. (2.11) shows that the resolution is inversely proportional to the chirp's bandwidth.

The range resolution Δy is given by

$$\Delta y = \frac{c}{2BW}. \tag{2.12}$$

Where c is the speed of light and BW is the bandwidth of the system. An optional view is that the range resolution is determined by the bandwidth of the chirp. This is because as the frequencies in the time domain widen the *sinc* becomes narrower in the frequency domain. In Fig. 2.2, a plane at height H, above the earth's surface

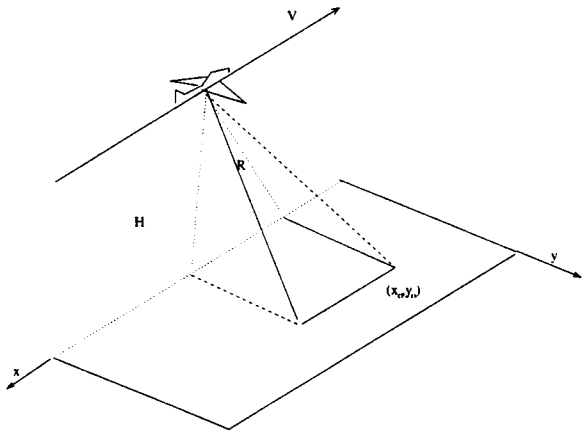

Figure 2.2: SAR Geometry

has a resolution of Δx in the azimuth direction and a resolution of Δy in the range direction. As the plane travels higher into the sky, the height of the aircraft H widens the beamwidths area of effect has on the ground. The wavelength λ affects the beamwidth because an antenna's electrical size is proportional to the wavelength associated with it. Therefore, as the wavelength gets smaller the antenna's electrical size relative to its wavelength gets bigger. It can then be shown that the resolution is inversely related to the size of the antenna, the height of the platform, and the

wavelength as described by

$$\Delta x = \frac{H\lambda}{L}. \tag{2.13}$$

This principle is illustrated using the actual specifications of the NASA Seasat satellite [2]. Using Eq. (2.13) for the azimuth resolution, the following parameters are set for the NASA Seasat satellite: H = 800 kilometers, λ =0.235m and $\Delta x = 5.5$. Solving for the length of the antenna L, the result is an unrealizable 34 kilometers. This style of radar is named real aperture radar (RAR) because the calculated antenna size is the actual size needed to achieve the desired resolution.

2.2 Synthetic Aperture Radar

As a solution to the problem of antenna size, Synthetic Aperture Radar (SAR) was developed in the late 1960's. Synthetic Aperture Radar (SAR) describes a radar imaging system that uses motion and signal processing to achieve high resolution in the azimuth direction. By mounting a SAR antenna on a moving object (land vehicle, aircraft or satellite), high resolution images may be taken with a relatively small antenna. Synthetic Aperture refers to the equivalent size of the antenna required to achieve the same resolution without the combination of motion and data processing.

Two different modes of SAR have been developed. Each uses a combination of hardware and signal processing to obtain high resolution images. These two SAR modes "stripmap" and "spotlight" will be discussed hereafter. Stripmap and spotlight modes each have their advantages and disadvantages.

Stripmap has the ability to take long constant image strips. With this ability, SAR can be used for navigation systems regardless of weather or lighting conditions with a real time processor. Examples of applications that use this type of radar include missile guidance systems, auto-pilot and large-area surveys [12].

Spotlight illuminates only one spot during the whole data collection time. Spotlight has superior resolution and noise suppression. Image processing and autofocus algorithms are also computational easier to implement. For a finite circular spot on the ground, relatively high resolution is obtained.

wavelength as described by

$$\Delta x = \frac{H\lambda}{L}. \tag{2.13}$$

This principle is illustrated using the actual specifications of the NASA Seasat satellite [2]. Using Eq. (2.13) for the azimuth resolution, the following parameters are set for the NASA Seasat satellite: H = 800 kilometers, λ =0.235m and $\Delta x = 5.5$. Solving for the length of the antenna L, the result is an unrealizable 34 kilometers. This style of radar is named real aperture radar (RAR) because the calculated antenna size is the actual size needed to achieve the desired resolution.

2.2 Synthetic Aperture Radar

As a solution to the problem of antenna size, Synthetic Aperture Radar (SAR) was developed in the late 1960's. Synthetic Aperture Radar (SAR) describes a radar imaging system that uses motion and signal processing to achieve high resolution in the azimuth direction. By mounting a SAR antenna on a moving object (land vehicle, aircraft or satellite), high resolution images may be taken with a relatively small antenna. Synthetic Aperture refers to the equivalent size of the antenna required to achieve the same resolution without the combination of motion and data processing.

Two different modes of SAR have been developed. Each uses a combination of hardware and signal processing to obtain high resolution images. These two SAR modes "stripmap" and "spotlight" will be discussed hereafter. Stripmap and spotlight modes each have their advantages and disadvantages.

Stripmap has the ability to take long constant image strips. With this ability, SAR can be used for navigation systems regardless of weather or lighting conditions with a real time processor. Examples of applications that use this type of radar include missile guidance systems, auto-pilot and large-area surveys [12].

Spotlight illuminates only one spot during the whole data collection time. Spotlight has superior resolution and noise suppression. Image processing and autofocus algorithms are also computational easier to implement. For a finite circular spot on the ground, relatively high resolution is obtained.

2.3 Stripmap SAR

The hardware in stripmap SAR is similar to the real aperture radar mentioned earlier, except for the storage devices used to store the parameters needed for azimuth compression. The needed parameters are platform velocity, position, antenna beamwidth, sample rate and the phase and amplitude of each return. Figure 2.3 shows the geometry for stripmap SAR. The range compression is the same as for the case of the real aperture radar using a matched filter technique. The range resolution for stripmap SAR is

$$\Delta y = \frac{c}{2BW}. \tag{2.14}$$

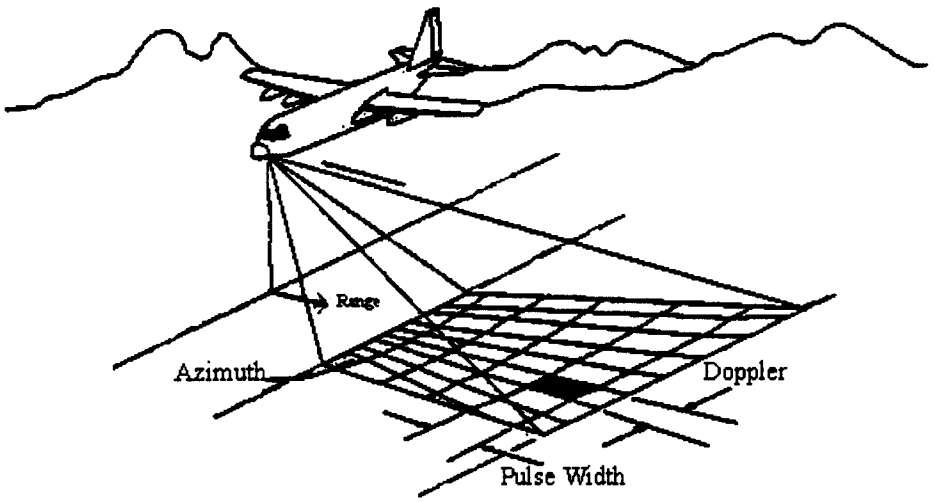

Figure 2.3: SAR Geometry for a Stripmap SAR

Azimuth compression was implemented by using the same type of matched filter processing in the azimuth direction that is used in the range direction. This was accomplished by forming a motion related function that is strongly correlated at only one point. One useful property of the LFM chirp introduced earlier is that

its autocorrelation function is a very narrow *sinc* as can be seen in Eq. (2.11). A function similar to the LFM chirp is found in the Doppler frequency of a target referenced to the movement of the platform. The range compressed data is correlated in the azimuth direction with the derived azimuth chirp. Therefore, compression in the azimuth direction becomes similar to compression in the range direction. The range data in Eq. (2.11) is compressed when $t = t_0$. The range compressed data is then expressed by

$$g(t_o) = A_k 2T \exp(-jw_c t_o + jw_o t_o)\ rect(-T/2 < t < T/2). \tag{2.15}$$

Where w_c is the carrier and w_o is the modulation. The *rect* represents the window of the antenna pattern on the ground.

Let the range distance for a given return be represented by the distance $R(t_o) = (t_o c)/(2)$. Since $w_c >> w_o$, the $w_o t_o$ term can be neglected $-w_c t_o + w_o t_o \simeq -w_c t_o$. Now a change of variables from t_0 to t sets t to the time measured in terms of the azimuth sample rate or PRF (pulse repetition frequency). The coefficients of $R(t)$ are dependent on the location of the target. Equation (2.15) may be represented as

$$\begin{aligned} g(t) &\simeq A_k 2T \exp(-jw_c t_o) rect(-T/2 < t < T/2) \\ &= A_k 2T \exp\left(\frac{4\pi R(t)}{\lambda}\right) rect(-T/2 < t < T/2). \end{aligned} \tag{2.16}$$

Derivation of the Quadratic Phase Term

The range to the target in Fig. 2.2 is found by geometry to be,

$$R(t) = \sqrt{x(t)^2 + y(t)^2 + H(t)^2} \qquad -T/2 < t < T/2. \tag{2.17}$$

Where t is the azimuth sample time, $x(t)$, $y(t)$ and $H(t)$, are the distances to the target in the x, y, and z planes respectively. T is determined by azimuth antenna beamwidth. In the motionless ideal case, $y(t)$ and $H(t)$ are constants, and $x(t) = x_o - vt$, where v is the velocity of the aircraft, to give:

$$R(t) = \sqrt{(x_o - vt)^2 + y_o^2 + H_o^2}. \tag{2.18}$$

Let $R_o = \sqrt{x_o^2 + y_o^2 + H_o^2}$ be the nominal minimum distance to the target. Solving for x_o and substituting into $R(t)$ gives:

$$R(t) = \sqrt{R_o^2 - 2x_o vt + (vt)^2}. \tag{2.19}$$

Expanding the above equation by a Taylor series expansion about $t = 0$ gives,

$$R(t) = R_o - \frac{x_o vt}{R_o} + \frac{v^2}{2R_o}(1 - \frac{x_o^2}{R_o^2})t^2 + \frac{xv^3}{2R_0^3}(1 - \frac{x_o^2}{R_o^2})t^3 + \ldots \tag{2.20}$$

Expanding around zero sets $x_o = 0$ and causes $R(t)$ to simplify to

$$R(t) = R_o + \frac{v^2 t^2}{2R_o} - \frac{v^4 t^4}{8R_0^3}. \tag{2.21}$$

Inserting the first two terms of Eq. (2.21) into Eq. (2.16) gives the phase Ψ

$$\begin{aligned} \Psi(t) &= 4\pi \frac{R(t)}{\lambda} \\ &\simeq \frac{4\pi R_o}{\lambda} + \frac{2\pi v^2 t^2}{\lambda R_o} rect(-T/2 < t < T/2). \end{aligned} \tag{2.22}$$

Equation (2.22) represents the azimuth chirp for each range bin. This azimuth chirp is the quadratic phase response for movement in the azimuth direction for a given constant range target. The normalized phase response of Eq. (2.22) is shown in Fig. 2.4.

Since the frequency is the derivative of the phase, an intuitive way to understand azimuth compression is to look for positive and negative Doppler frequencies in the received signal.

$$Doppler\ Frequency = \frac{4\pi v^2 t}{\lambda R_o} rect(-T/2 < t < T/2) \tag{2.23}$$

An azimuth chirp is composed of the Doppler frequency for each scatterer. When the scatterer is in front of the plane the Doppler frequency is positive and when the scatter is behind the plane the Doppler frequency is negative. This steady change of the Doppler frequency from high positive frequency to zero and then to high negative frequency creates a chirp similar to the LFM chirp used in the range direction. The point where the Doppler frequency is zero corresponds to the point

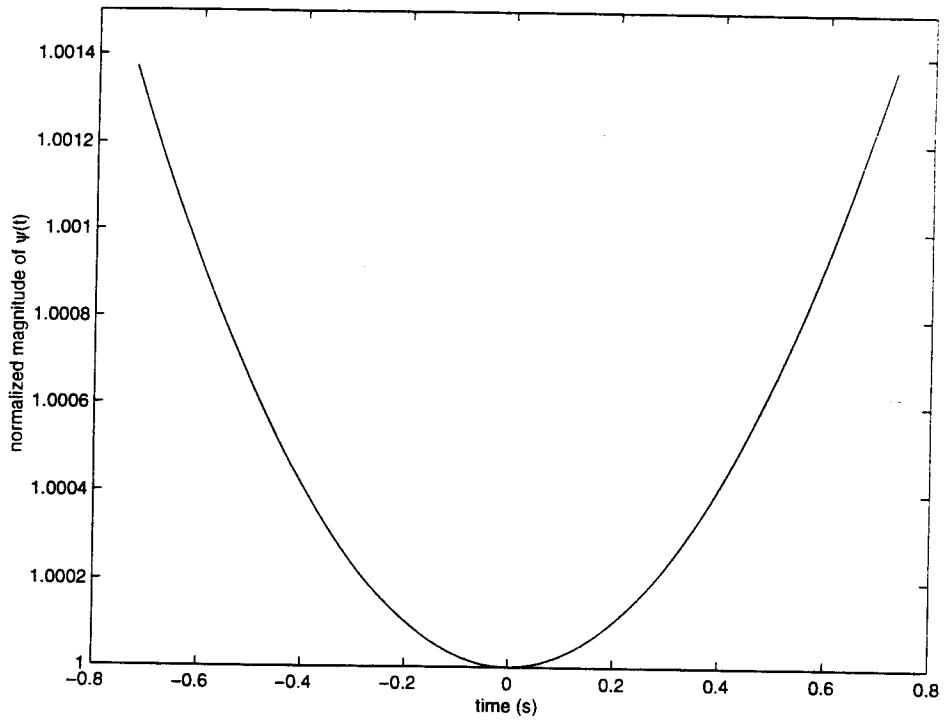

Figure 2.4: The normalized phase change of a target, referenced to a constant velocity moving vehicle for stripmap SAR. The range change causes a quadratic phase pattern.

where the azimuthal blurred image should be compressed. This azimuth chirp is then used with a matched filter in the azimuth direction to produce high resolution.

The improvement in the azimuth resolution is considerable. Using the Synthetic Aperture increases the resolution significantly when compared to the real aperture case. In the example of the Seasat satellite, using the azimuth compression, the azimuth resolution is 5.5 meters, while the antenna is only 11 meters long. Comparing this to a real aperture with the same resolution, an antenna of over 34 kilometers is needed. The tradeoffs are the required storage and processing.

Stripmap mode requires the derivation of the azimuth chirp or quadratic phase expected for each range bin in the image. This chirp is then correlated with each corresponding range bin. This difficulty in azimuth resolution is the hinderance for Stripmap auto-focusing techniques.

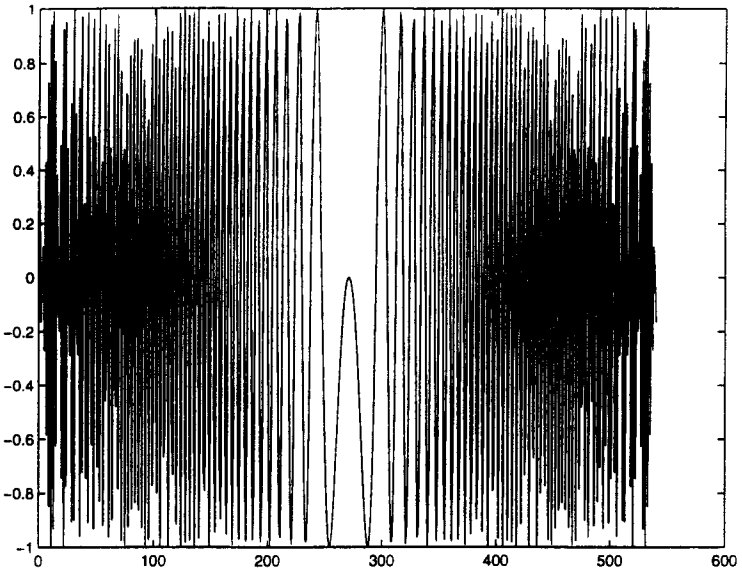

Figure 2.5: Azimuth Chirp of target located at the 270^{th} pixel

2.4 Spotlight Synthetic Aperture Radar

Spotlight SAR (SSAR) is motivated by the same desire for high azimuth resolution as stripmap SAR. A comparison between the spotlight and stripmap data collection methods is shown in Fig. 2.6. SSAR uses the same range compression techniques used in stripmap SAR. SSAR uses a steerable antenna to focus on one spot on the ground like a spotlight.

In stripmap mode, the antenna is stationary and the length of the azimuth chirp varies with different range lines. In the spotlight mode, the antenna is connected to a gimble which steers it to illuminate a stationary spot on the ground as shown in Fig. 2.7. As the plane moves, the spotlight is maintained on the same spot. This gives almost a 180 degree view of the same spot on the ground. The steering of the antenna provides a longer exposure time, thus providing many samples of the same area. With the antenna constantly changing direction to focus on the same spot, the resulting antenna pattern is very large. Equation (2.23) shows that the maximum chirp frequency is restricted by the *rect* created by the antenna beamwidth. In

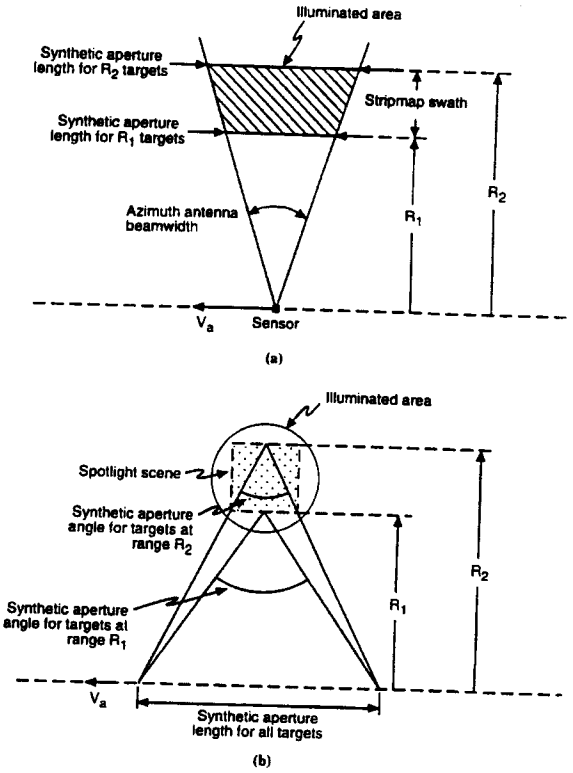

Figure 2.6: (top) Stripmap SAR has a constantly changing coverage area. The stripmap range swath is restricted by the range gateing of the system. The stripmap azimuth swath is restricted by antenna beamwidth and the desired bandwidth of the system. (bottom) Spotlight SAR uses a spotlight like antenna to focus on one spot continually requiring a gimble to continually move the antenna to the focus center. The size of the spot is restricted by the antenna pattern. [1]

spotlight mode the *rect* spans the whole data collection time. Consequently the *rect* may be dropped from the equation to yield

$$Doppler\ Frequency = \frac{4\pi v^2 t}{\lambda R_o}. \tag{2.24}$$

The maximum Doppler frequency is now dependant on the length of the collection time. This gives extremely high bandwidths that have the ability to produce very high resolution images. Therefore, the obtainable resolution in the spotlight images is higher than in the stripmap images. Because of the high bandwidth of the

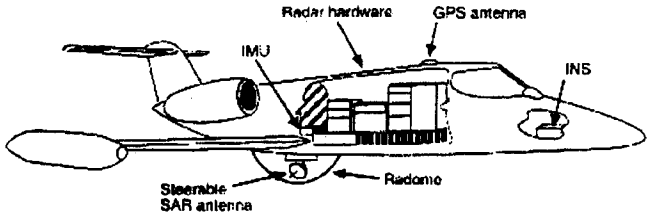

Figure 2.7: Example Antenna hardware

chirps produced in spotlight data, the data usually cannot be sampled directly. The rotating antenna allows the center of the image to be stationary. By centering the conjugate of the chirp in the middle of the image and mixing it with each received signal, the high bandwidth chirp may be removed in hardware easing the sampling frequency requirements. A chirp is still present at every point in the image. By centering the conjugate of the chirp in the middle of the image and multiplying the range compressed image, an azimuth position dependent frequency remains for each pixel. To show this development, an image with two pixels A and B will be introduced. One pixel will be located at the center of the image and the other pixel will be located at azimuth time (corresponding to position) t_2.

$$\begin{aligned} c(t) &= e^{\frac{2\pi v^2 t^2}{\lambda R_o}} \\ g_m(t) &= A_m\delta(t)e^{j\theta_A} + B_m\delta(t-t_2)e^{j\theta_B} \end{aligned} \tag{2.25}$$

The azimuth chirp is $c(t)$, and θ_A and θ_B correspond to the inherent phase of each target A and B respectively. If we start with the initial range compressed data, the return for each pixel $r(t)$ is represented by its amplitude, phase and azimuth chirp as,

$$r(t) = g_m(t) \otimes c(t). \tag{2.26}$$

To show the hardware dechirp step, $r(t)$ is multiplied by $c^*(t)$ centered in the image to yield a new $r'(t)$,

$$r'(t) = [(A\delta(t)e^{j\theta_A} + B\delta(t-t_2)e^{j\theta_B}) \otimes c(t)]c^*(t). \tag{2.27}$$

Implementing the convolution steps, the above equation reduces to:

$$
\begin{aligned}
r'(t) &= [Ac(t)e^{j\theta_A} + Bc(t-t_2)e^{j\theta_B}]c^*(t) \\
r'(t) &= [Ae^{j\frac{-2\pi v^2(t)^2}{\lambda R}+\theta_A} + Be^{j\frac{-j2\pi v^2(t-t_2)^2}{\lambda R}+\theta_B}]c^*(t) \\
r'(t) &= [Ae^{j\frac{-2\pi v^2(t)^2}{\lambda R}+j\theta_A} + Be^{j\frac{-2\pi v^2(t-t_2)^2}{\lambda R}+j\theta_B}]e^{j\frac{2\pi v^2(t)^2}{\lambda R}} \\
r'(t) &= [Ae^{j\theta_A} + Be^{j\frac{-2\pi v^2(t-t_2)^2}{\lambda R}+j\theta_B}e^{j\frac{2\pi v^2(t)^2}{\lambda R}}] \\
r'(t) &= [Ae^{j\theta_A} + Be^{j\frac{-2\pi v^2}{\lambda R}(2t_2t+t_2^2)+\theta_B}] \\
r'(t) &= [Ae^{j\theta_A} + Be^{j\frac{-2\pi v^2 t_2^2}{\lambda R}+\theta_B}e^{j\frac{-2\pi v^2}{\lambda R}(2t_2t)}].
\end{aligned}
\tag{2.28}
$$

Observing the above equation, it is seen that the only t dependant phase term is a linear term of the B scatterer. From basic Fourier transform theory, we see that the $e^{j\frac{-2\pi v^2}{\lambda R}(2t_2t)}$ term will result in a shift in the frequency domain. This property is used for azimuth compression. Each azimuth pixel will be shifted in proportion to its distance from center. The Fourier transform results in

$$
\begin{aligned}
a(t) &= \mathcal{F}\{Ae^{j\theta_A} + Be^{jc_1t_2^2+j\theta_B}e^{j(c_1 2t_2t)}\} \\
a(t) &= Ae^{j\theta_A} + Be^{jc_1t_2^2+j\theta_B}e^{(j\omega t_2)}.
\end{aligned}
\tag{2.29}
$$

Where $a(t)$ is the azimuth compressed or the image domain. SSAR has a very simple compression algorithm when compared to the stripmap mode SAR. This advantage reduces computation and allows easy access to the important phase history.

Chapter 3

Spotlight Autofocus Algorithms and Phase Gradient Autofocus

In the previous chapter, the derivation of ideal spotlight and stripmap compression was presented. Many factors inhibit the actual image from being ideal. The main problem is unknown phase variations in the scattered return. The causes of this phase error is mainly from movements in the radar platform, but other interferences in the propagation of the electromagnetic waves also cause errors. In both the spotlight and stripmap modes the compression algorithms use the phase changes created from the movement of the radar to compress the images as seen in Eqs. (2.4) and (2.30). In Eq. (2.18), $H(t)$ and $y(t)$ are assumed to be constants. In low resolution radar these assumptions will hold. However, in high resolution images, with the resolution on the order of 1m or less, vibrations and movements of the radar platform cause significant blurring. If the movements in those two directions are included in Eq. (2.18) then the resulting azimuth chirp could be substantially different. Even when using a motion measuring device like an IMU, the vibrations of the antenna and the propagation effects are unknown. These random movements make the direct compensation impossible. These movements and phase disturbances will be referred to as phase errors. The phase errors treated in this chapter will be restricted to high altitude spotlight SAR system phase errors described next..

If the H in Fig. 3.1 is much greater than the $R_0 - R_1$ (swath width) when the changes in look angle $\Delta\theta$ may be neglected

$$\Delta\theta = \tan^{-1}\frac{R_0}{H} - \tan^{-1}\frac{R_1}{H} \simeq 0. \tag{3.1}$$

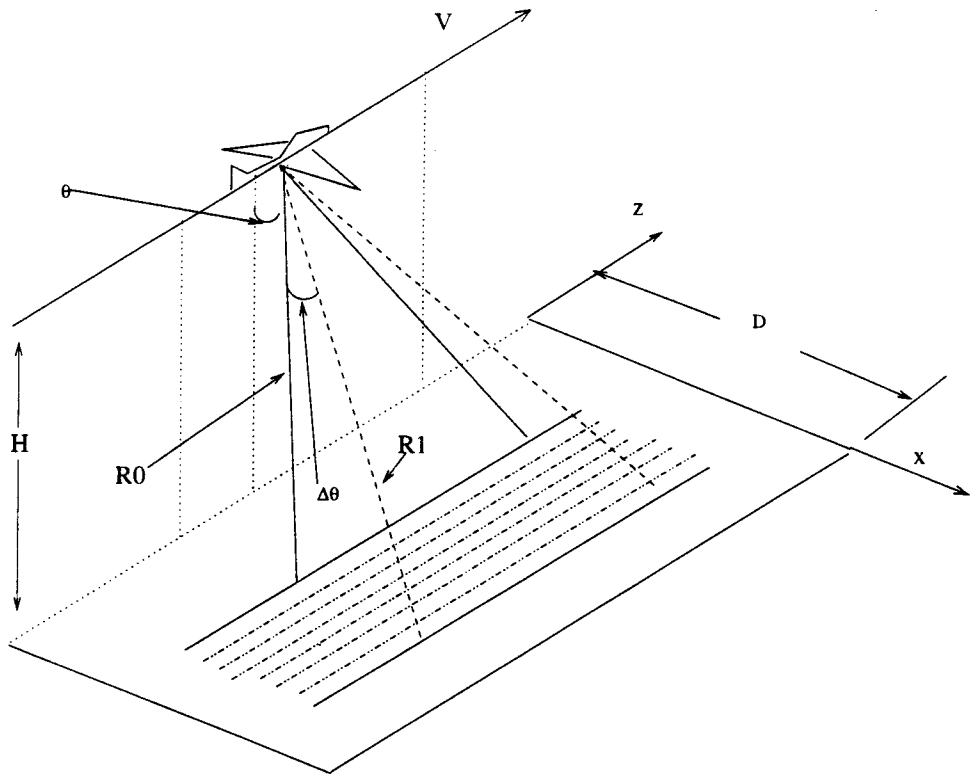

Figure 3.1: Range Dependent SAR Geometry

Most spotlight systems satisfy the height restraint given above. In high altitude spotlight systems the phase error can be approximated as being the same for all range lines. Several phase error estimators have been developed, but only one has shown exceptional results on all types of images and phase errors. This phase estimator is called Phase Gradient Autofocus (PGA). Two other algorithms were used before the PGA. The first is called inverse filtering [2]. Inverse filtering uses bright known targets and finds the transform function which transforms it into a delta function. This algorithm may only be used with images that have bight point targets. The second algorithm called map drift [2] models the errors as being a low order polynomial. This method limits the errors that may be compensated. Both of these methods have had limited success, due to the limited images and SAR types that may be used with them.

The PGA was first introduced by Charles V. Jakowatz in 1988 [4]. The PGA has four major steps. The four steps are: center shifting, windowing, phase gradient estimation and iteration. A flow chart of this is presented in Fig. 3.2. Several different estimators have been developed for the phase gradient estimator step. The optimal estimator for the PGA model is Maximum Likelihood.

Maximum Likelihood PGA assumes that the phase error is constant with range and estimates the error in the azimuth direction. Therefore, it cannot be used with low altitude systems. A more complete approach to this problem is developed in Chapter 4.

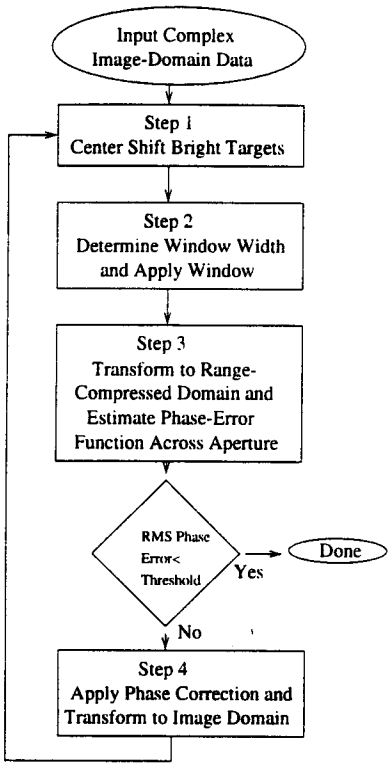

Figure 3.2: PGA Steps The PGA has four main steps. The first shifting step is to remove the phase modulation used in compression, the second is to window out phase noise from far scatterers, the third is to estimate the phase gradient, and the last step is iteration.

The PGA will be presented with a point target in range bin n placed in the compressed image at azimuth point ω_0. The spotlight compression is the same as was derived in the previous chapter, except that a unknown phase error is introduced. In the spotlight image domain a scatterer is represented by

$$G_n(\omega) = A_n\delta(\omega - \omega_0)]e^{j\theta_A} \otimes E(\omega), \tag{3.2}$$

where $E(\omega)$ is the Fourier transform of the phase error function, $G_n(\omega)$ is the image domain of the n_{th} range bin, A_t is the amplitude of the scatterer, and θ_A is the phase of the scatterer. The range compressed image is achieved by taking the inverse Fourier transform of Eq. (3.2). The point target is represented in the range compressed time domain by

$$g_n(t) \;=\; A_n e^{-j(\omega_0 t + \phi_e(t) + \theta_A)}, \tag{3.3}$$

where A_t, ω_0 and θ_A are the magnitude, frequency and phase of the signal respectively, and $\phi_E(t)$ is the phase error from the motion of the platform.

3.1 Complex Shift

In the image domain, the important phase history is evident in all pixels because spotlight mode focuses on one spot during the whole data acquisition. This constant focusing removes the band limitation.

The purpose of phase shifting is to remove the modulation out of the signal and to use the brightest signal on each constant range line. The brightest point contains the least clutter noise shown in Chapter least phase variance as shown in Chapter 4. The equation is discretized with N range lines and M azimuth lines. When each maximum amplitude A_n in each constant range line is shifted to zero frequency, then the $e^{\omega_0 t}$ phase term is eliminated to give

$$g_n(m) = A_n e^{-j(\phi_e(m) + \theta_A)}. \tag{3.4}$$

The $\phi_e(m)$ term in Eq. (3.4), which is the phase error from the movement of the aircraft, is the only function dependent on azimuth (time) remaining.

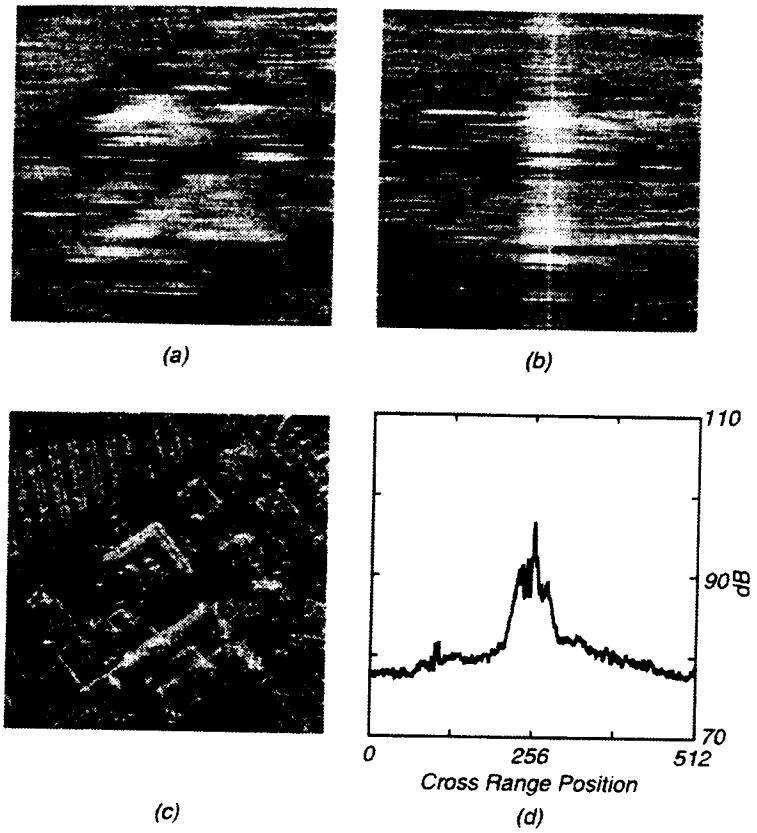

Figure 3.3: Example of the steps of the PGA: (a)Blurred image, (b)Circular Phase Shift, (c)Restored Image, (d)Window size [2].

3.2 Windowing

The next step is to window around the shifted brighter points in each range line. After shifting the brightest point on each constant range line to zero frequency, the rest of the points on each range line are modeled as Gaussian white noise. This model is almost accurate, but not completely because of possible correlation of the targets on the ground. However, this model works very well for most cases. All other targets left in the image create noise in the phase when the inverse Fourier transform is taken. With the position-frequency relationship of the scatterers, the scatterers

that are farthest from the brightest shifted point create the highest frequency noise. The windowing filters out the high frequency noise. Care must be taken as the window size is chosen, to not window out some of the phase error frequencies.

This step of windowing can be represented by a weighting function of $W(\omega)$. When this function is multiplied then the unwanted high frequency noise is zeroed out. As the window length decreases, the high frequency components are decreased creating a more accurate phase estimation. The inverse Fourier transform of the shifted windowed image domain is

$$g(t) = A_t e^{j(\theta_A + \phi_e(t))} \otimes w(t) + \eta(t). \tag{3.5}$$

where $w(t)$ represents the inverse Fourier transform of the window function. If the window size is chosen accurately then w(t) can be dropped without loss of accuracy to yield,

$$g(t) = A_t e^{j(\theta_A + \phi_e(t))} + \eta(t). \tag{3.6}$$

The function $g(t)$ represents a magnitude multiplied by a complex exponential. This complex exponential contains the motion phase error $\phi_e(t)$ which is a function of time and an inherent phase constant θ_A.

3.3 Phase Gradient Estimation

There are two main options for phase estimation. The phase estimation is done in the range compressed domain. The most common method, Maximum likelihood (ML), will be discussed. Equation 3.6 shows that the phase error and a phase constant remain in each pixel. ML isolates the phase error, takes the derivative, and then integrates it. Maximum likelihood is derived from a special case of the eigenvector method. The eigenvector method will be introduced, along with the ML, and examples will be used to demonstrate its success.

3.3.1 Eigenvector Method

The eigenvector method [4] is the basis for the maximum likelihood method discussed in the next section. Using the model introduced earlier, each point in the

image is modeled as a scatterer with Gaussian white noise created from the mutually independent, identically distributed targets spread in both the range and azimuth directions:

$$g_n(m) = A_n e^{j(\theta_A + \phi_e(m))} + \eta(n, m). \tag{3.7}$$

These points are then included in vectors that expand in the azimuth direction,

$$\text{Data vector: } \mathbf{X}_n^T = [g_{n1}, ..., g_{nN}]. \tag{3.8}$$

The logarithm of the conditional probability density can be taken because the samples are i.i.d, to simplify the problem as,

$$\ln \mathbf{p}(\mathbf{X}|\Phi) = -N \ln[\pi_M|\mathbf{C}] - \sum_{n=1}^{N} \mathbf{x}_n^H C^{-1} \mathbf{x}_n. \tag{3.9}$$

C is the covarience matrix for each range line of data and Ψ is a vector of phase errors represented as

$$\Phi = [0, \phi_{e2}, \ldots, \phi_{eM}]. \tag{3.10}$$

The general definition of the covarience is used with the model to find the covarience matrix,

$$\mathbf{C} = \sigma_n^2 \mathbf{I} + \sigma_a^2 \mathbf{v}\mathbf{v}^H. \tag{3.11}$$

I is the identity vector and $\mathbf{v}$ is the phase only vector described below,

$$\text{Phase estimate vector: } \mathbf{v}^T = [1, e^{j\psi_{e2}}, \ldots, e^{j\psi_{eN}}]. \tag{3.12}$$

The maximum likelihood estimator for the phase error vector Φ is based on finding the value of Φ that maximizes Eq. (3.9). The result of the maximization can be found in detail in [4]. The solution to maximize Eq. (3.9) is found to be the same as maximizing

$$Q_3 = \mathbf{v}^H \hat{\mathbf{C}} \mathbf{v}. \tag{3.13}$$

3.3.2 Maximum Likelihood

In 1993 a method for maximum likelihood estimation of phase errors was published [4]. This process is superior because it does not assume a high signal to clutter ratio, and eliminates the bias problem. The Maximum likelihood is a special case of the eigenvector method.

The SAR image is again constructed of N range lines and M azimuth columns. After center shifting and windowing the same model used previous gives

$$g_n(m) = A_n e^{j(\theta_A + \phi_e(m))} + \eta(n,m). \tag{3.14}$$

The ML derivation is found by taking the special case of the eigenvector method with M=2. This case of the eigenvector method estimates the phase gradient with two pixels. In this case Eq. 3.13 is represented as

$$\mathbf{Q_3} = \frac{1}{N}[1 \; e^{-j\psi}] \begin{bmatrix} \sum_{n=1}^{N} |g_{n,m}|^2 & \sum_{n=1}^{N} g_{n,m} g_{n,m+1}^* \\ \sum_{n=1}^{N} g_{n,m}^* g_{n,m+1} & \sum_{n=1}^{N} |g_{n,m+1}|^2 \end{bmatrix} \begin{bmatrix} 1 \\ e^{j\phi_e} \end{bmatrix} \tag{3.15}$$

The maximum likelihood is solved by finding the values of ψ that maximizes $\mathbf{Q_3}$. Multiplying the matrices results in

$$\begin{aligned} \mathbf{Q_3} &= \sum_{n=1}^{N} (g_{n,m} g_{n,m+1}^* e^{j\psi} + g_{n,m}^* g_{n,m+1} e^{-j\psi}) \\ &= \left| \sum_{n=1}^{N} g_{n,m} g_{n,m+1} \right| \cos\left[\Delta\psi - \angle \left(\sum_{n=1}^{N} g_{n,m}^* g_{n,m+1} \right) \right]. \end{aligned} \tag{3.16}$$

Setting $\Delta\psi = \angle \left(\sum_{n=1}^{N} g_{n,m}^* g_{n,m+1} \right)$ creates a maximum of $\cos(0) = 1$. Thus the maximum likelihood solution is

$$\Delta\psi = \angle \left(\sum_{n=1}^{N} g_{n,m}^* g_{n,m+1} \right). \tag{3.17}$$

An intuitive approach follows:

The maximum likelihood results in finding the averaging of all the lines then taking the phase difference. The phase difference may be found by multiplying the current pixel with the conjugate of the neighboring pixel,

$$\Delta\phi = \angle[\bar{g}_{n,m-1}\bar{g}^*_{n,m}], \tag{3.18}$$

which gives,

$$g_{n,m}g^*_{n,(m-1)} = (A_n e^{j(\theta_A+\phi_{e\,m})} + \eta_{n,m})((A^*_n e^{-j(\theta_A+\phi_{e\,m-1})} + \eta^*_{(n,m-1)}). \tag{3.19}$$

Averaging all the constant range lines reduces the noise because each of these lines are uncorrelated with all other lines and also uncorrelated with the phase error. Thus, the phase error is estimated. The cross correlation of the noise with the scatterer is calculated by the expectation of the scatterer by the expectation of the noise. The auto correlation of the noise is a delta function since it is assumed that the noise can be modeled as white Gaussian. This is useful because the only variable left will be the phase difference, weighted by its magnitude. The result is

$$< |A_n|^2 e^{j(\phi_{e\,(n,m)}-\phi_{e\,(n,m-1)})} > . \tag{3.20}$$

To derive the phase function the above equation can be written as

$$\widehat{\Delta\phi} = \angle \sum_{n=1}^{N} [\bar{g}_{n,m-1}\bar{g}^*_{n,m}] \tag{3.21}$$

The entire aperture phase error is then estimated by integrating the $\hat{\Delta\phi}(m)$

$$\hat{\phi_{n,m}} = \sum_{n=2}^{N} \widehat{\Delta\phi}_{n,m};\ \widehat{\Delta\phi}_{1,m} = 0 \tag{3.22}$$

This result is the same as the special case of the eigenvector method.

3.4 Iteration

The last step is iteration. The windowing function of step 2 produces an iterative step. The wider the window, the higher frequency noise that is entered into the phase. As one estimate of the phase is made and corrected, the phase error frequency content decreases. The window is narrowed to lower the noise in the phase estimation step and a better phase estimate is obtained. This process is repeated until the estimated phase error difference between steps reaches a lower threshold.

3.5 Maximum Likelihood Results

To demestrate the versatility of the Maximum Likelihood PGA, three types of images have been chosen. The three images are a desert image with no distinct targets Figs. 3.4 through 3.8, a mountain scene with distributed targets Figs. 3.9 through 3.13, and an urban image with bright targets in close proximity Figs. 3.14 through 3.20. The ML PGA showed excellent results in all types of images and phase errors. A high frequency phase error was applied to the urban image in Figs. 3.19 3.20, to simulate high frequency vibrations at the antenna or trigger jitter in the A/D converter. The high frequency errors were estimated and compensated comparably to the low frequency errors. The results are seen in the following figures.

3.5.1 Desert Image: No Significant Scatterers

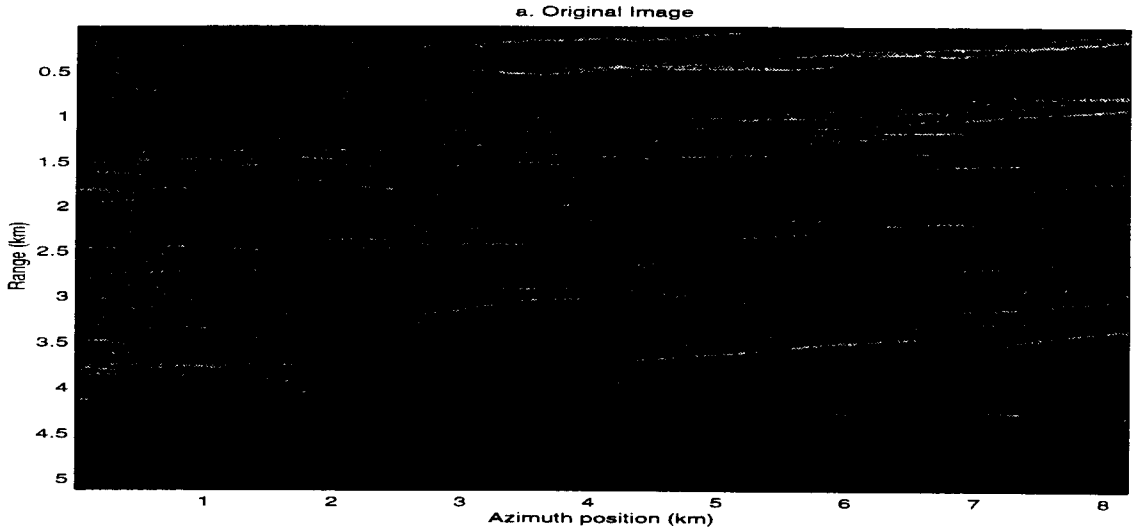

Figure 3.4: The original, focused SAR image of the desert.

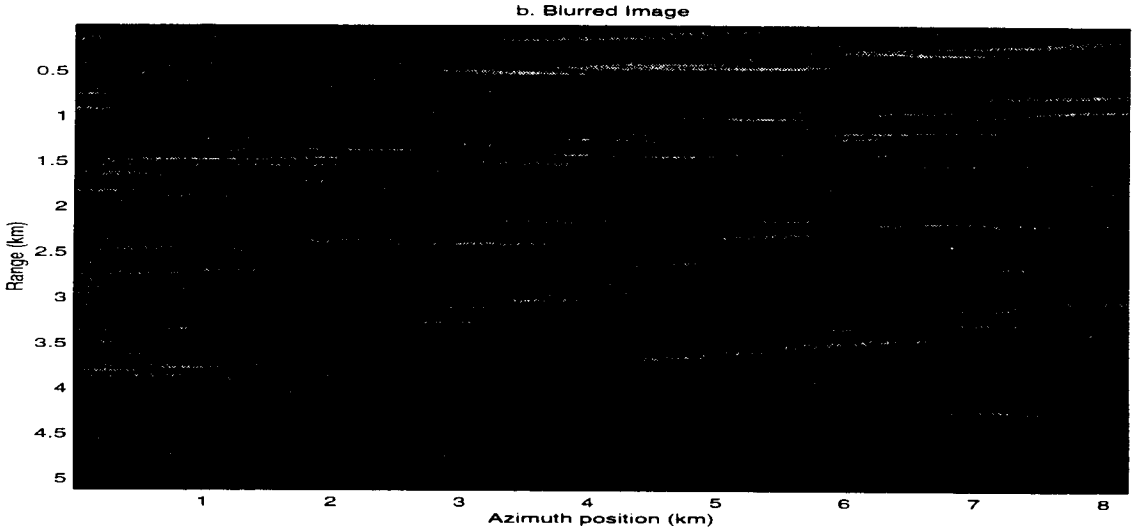

Figure 3.5: The phase corrupted desert image.

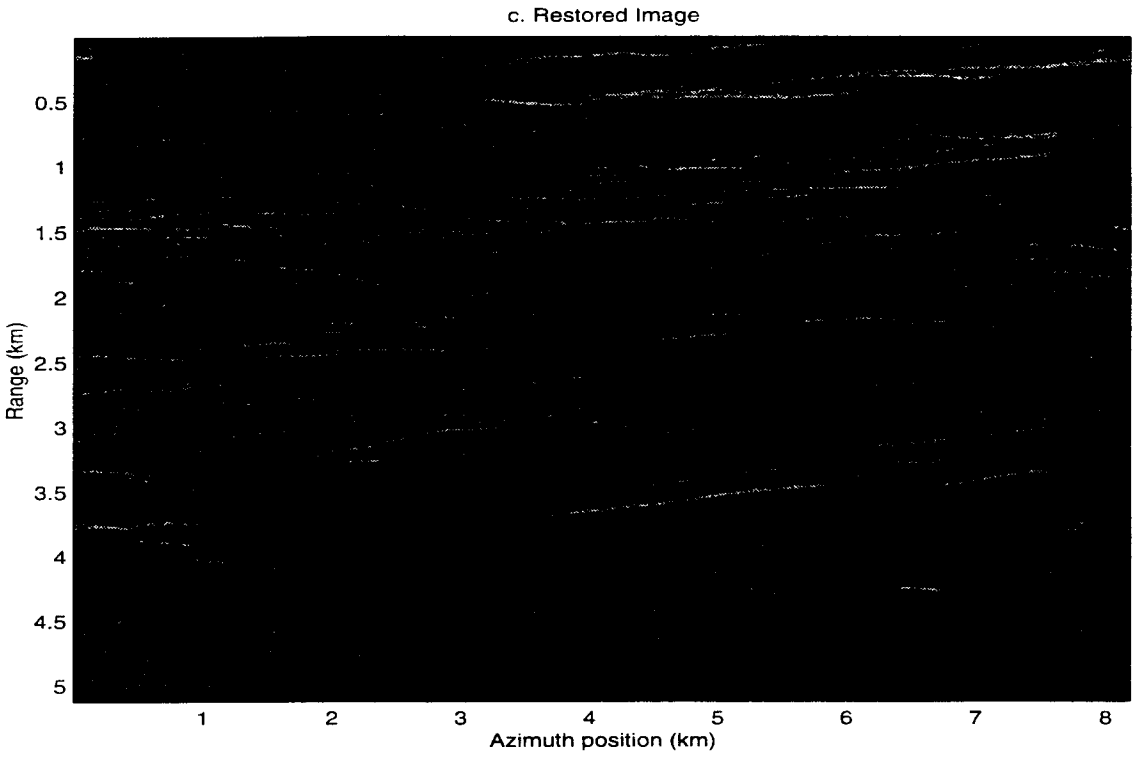

Figure 3.6: The restored desert image using the ML PGA algorithm.

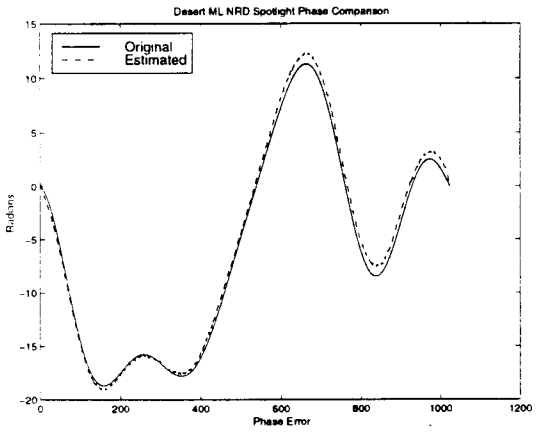

Figure 3.7: The maximum likelihood autofocus algorithm shows excellent results within the first couple of iterations. This desert image has no significant targets.

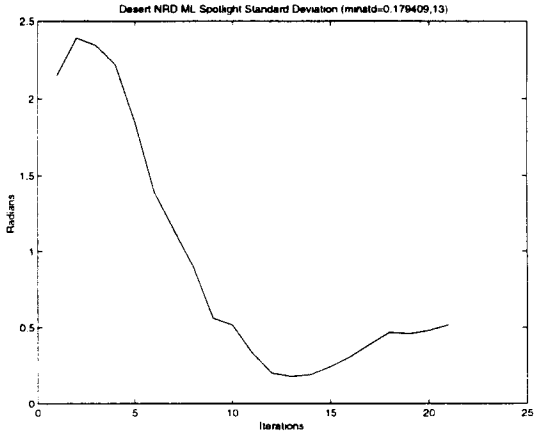

Figure 3.8: The Standard Deviation from the true phase error for the desert image shows excellent results.

3.5.2 Mountain Image: Some Significant Scatterers

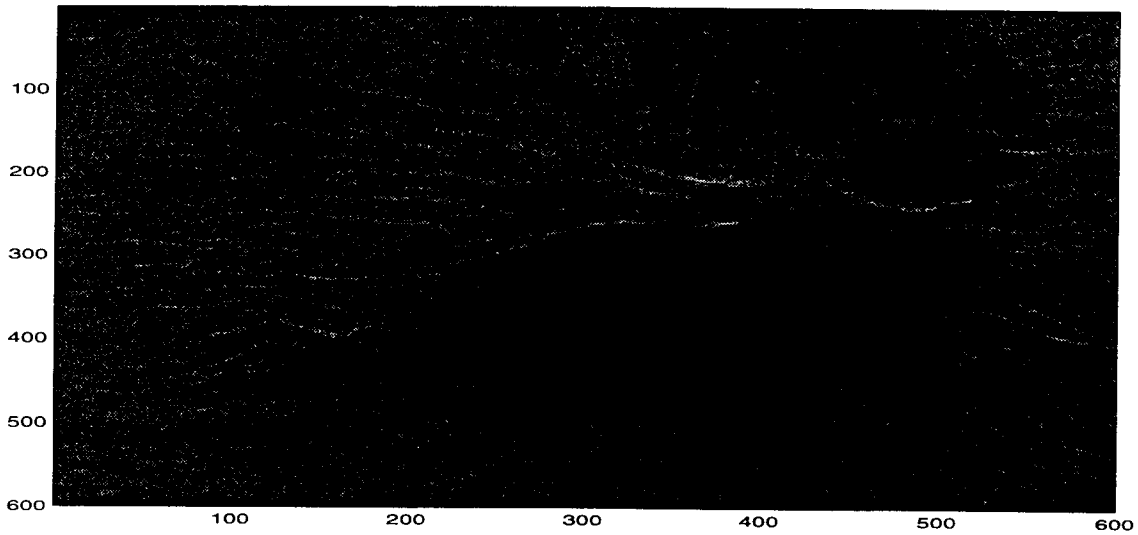

Figure 3.9: The original, focused SAR image of a mountain.

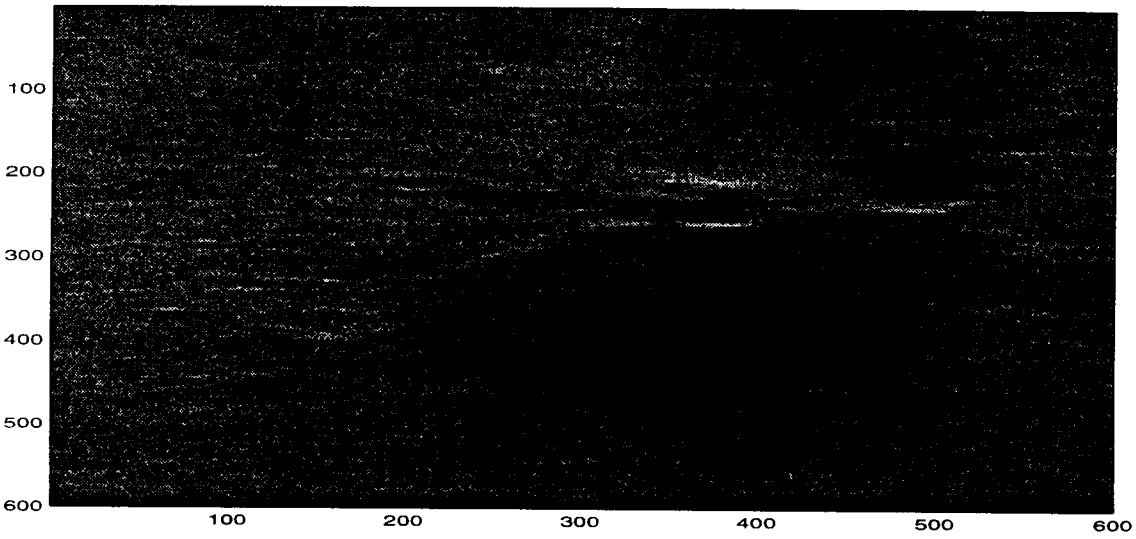

Figure 3.10: The phase corrupted mountain image.

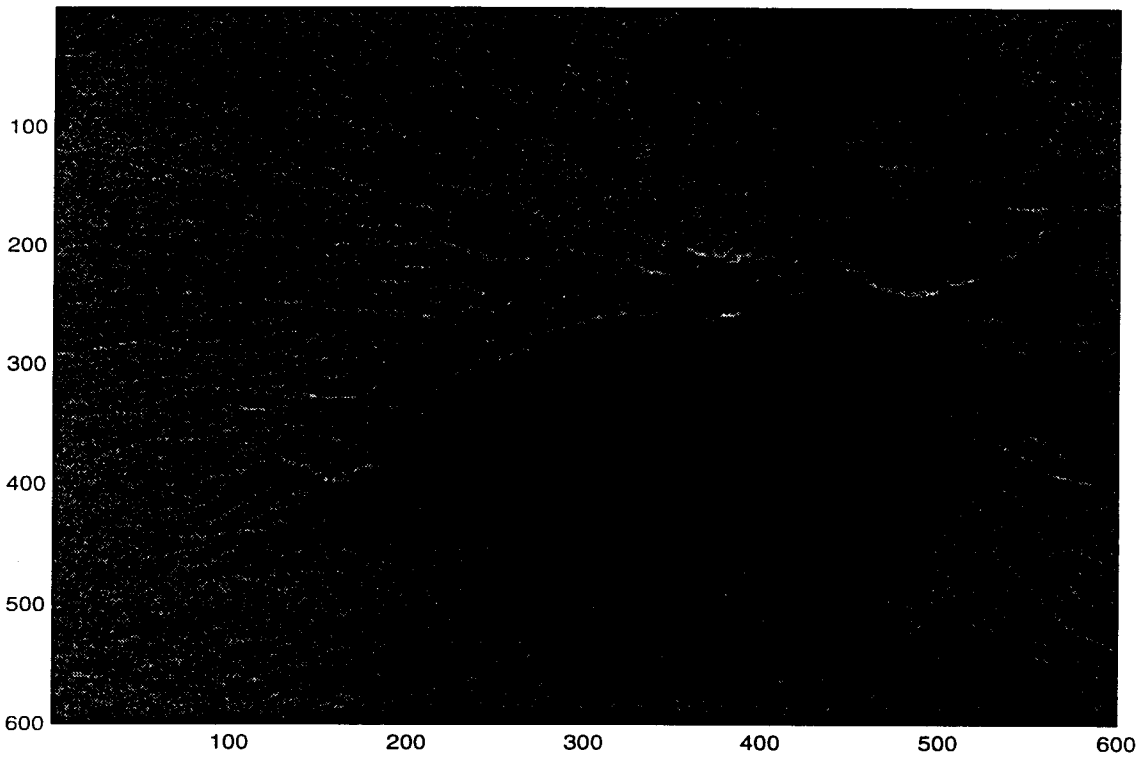

Figure 3.11: The restored mountain image using the ML PGA algorithm.

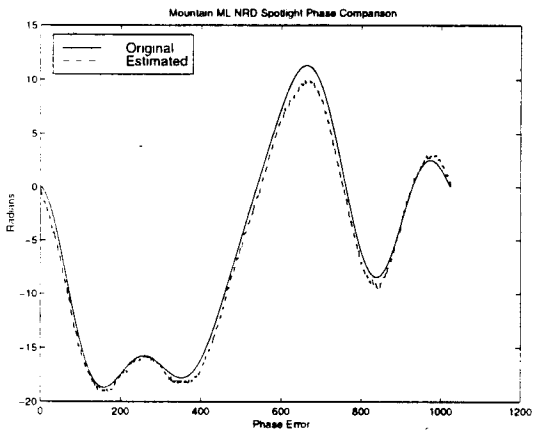

Figure 3.12: The maximum likelihood autofocus algorithm shows excellent results within the first couple of iterations. This mountain image has distributed targets.

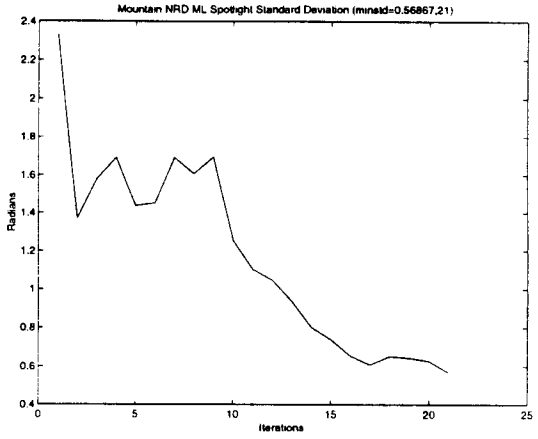

Figure 3.13: The Standard Deviation from the true phase error. This mountain image has distributed targets.

3.5.3 Urban Image: Many Significant Scatterers

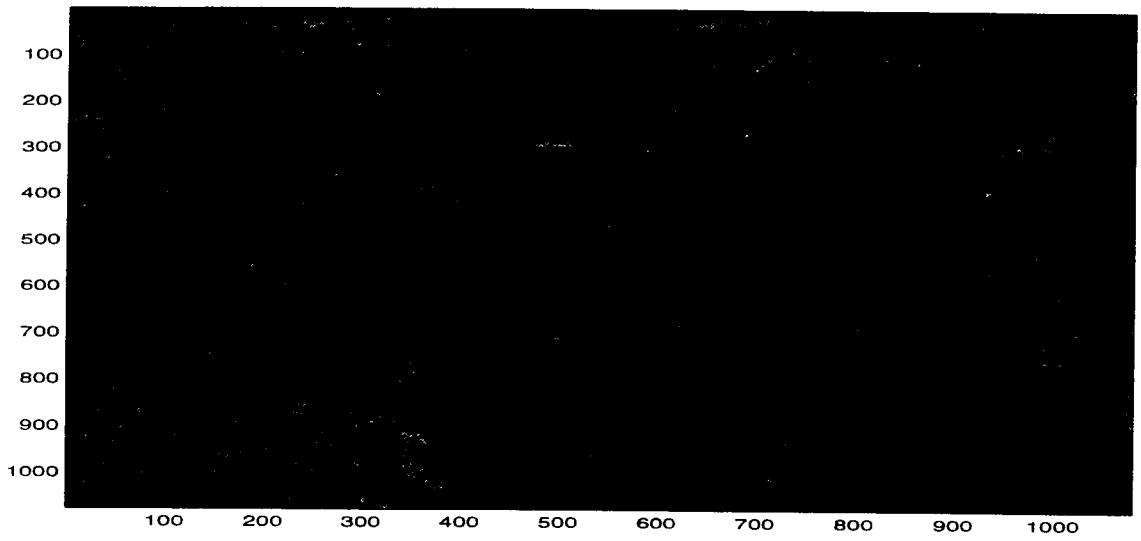

Figure 3.14: Urban image.

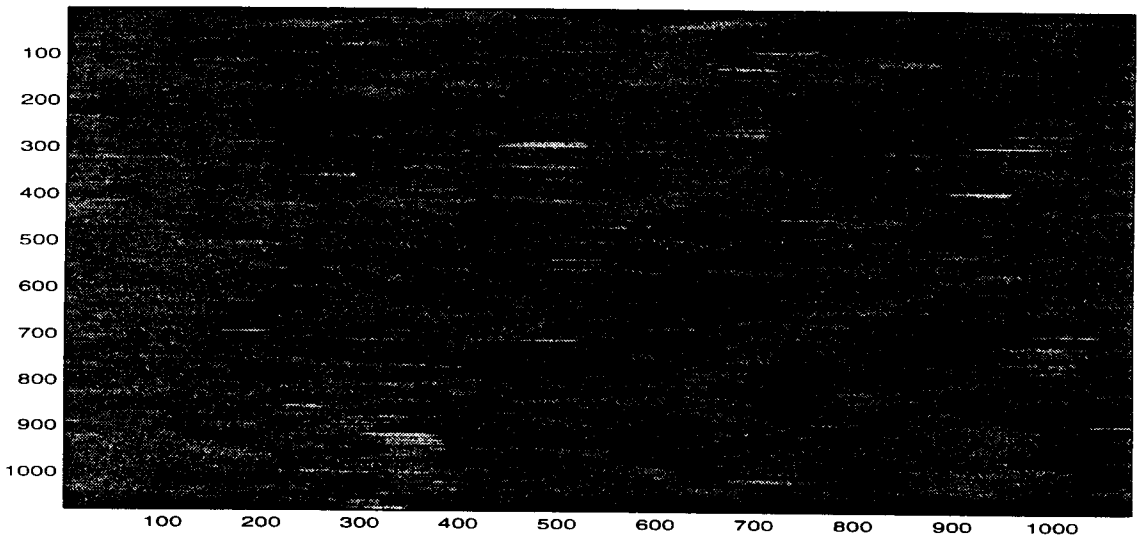

Figure 3.15: Blurred spotlight non-range dependent urban image.

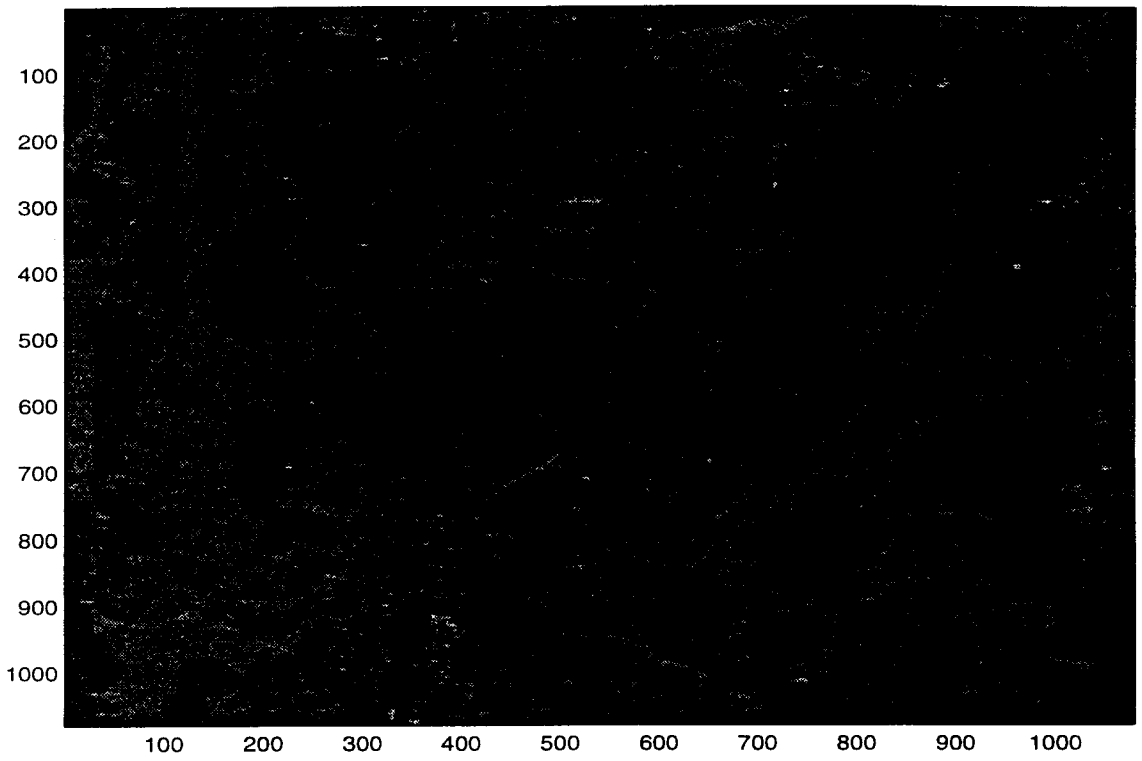

Figure 3.16: The restored urban image using the ML PGA algorithm.

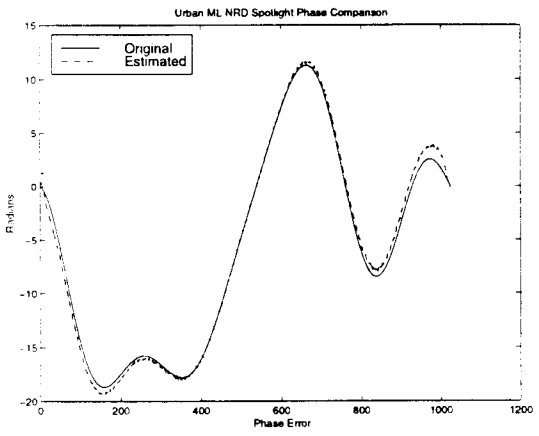

Figure 3.17: The maximum likelihood autofocus algorithm shows excellent results within the first couple of iterations. This urban image has bright targets in close proximity.

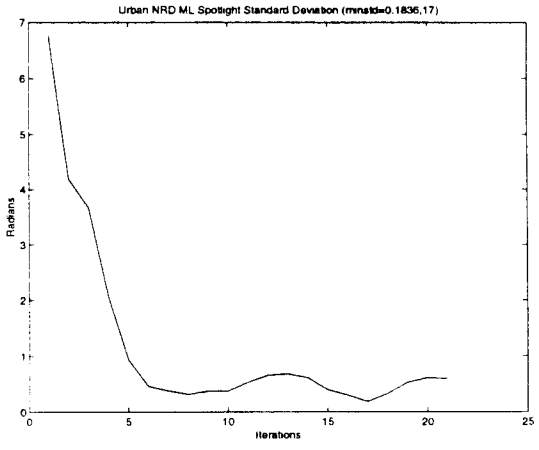

Figure 3.18: The Standard Deviation from the true phase error. This urban image has bright targets in close proximity.

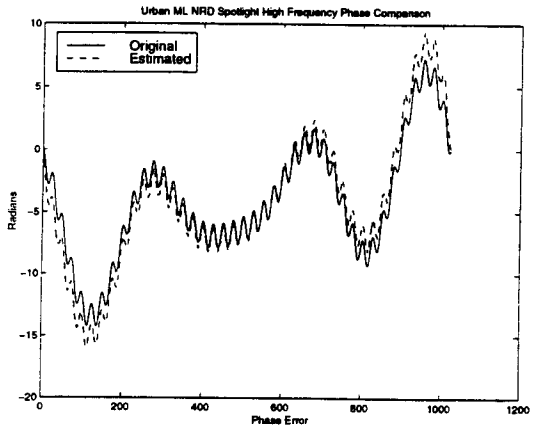

Figure 3.19: The maximum likelihood autofocus algorithm shows excellent results even with a high frequency phase error within the first couple of iterations. This urban image has bright targets in close proximity.

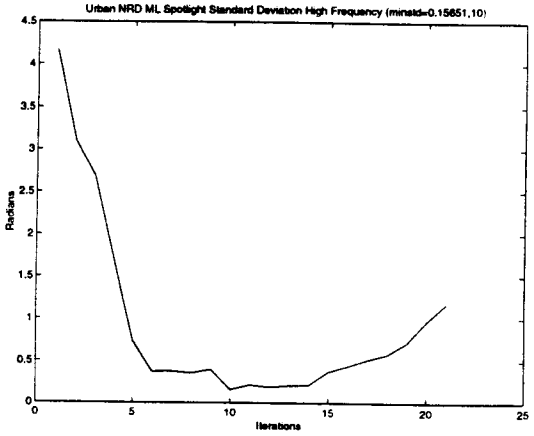

Figure 3.20: The Standard Deviation for the high frequency phase error. This urban image has bright targets in close proximity.

Chapter 4

Range Dependent Error and Phase Weighted Estimation

Range dependent phase errors can not be estimated with the PGA introduced in Chapter 3. ML PGA assumes that the phase error is constant along the range direction and varies in the azimuth direction. If a high altitude narrow beam assumption can not be made, then the averaging step of the ML PGA Eq. (3.21) will not estimate the gradient phase error accurately. The algorithm will not average correctly giving erroneous results. A new phase estimation step was developed using the derived phase change caused by the low altitude geometry of the system. This method is called Phase Weighted Estimation (PWE).

4.1 Range Dependent Geometry and Motion

Figure 4.1 shows an airplane as the radar platform, flying at altitude H, in the z direction, with the closest range as $R0$ and the farthest range as $R1$. If H is much larger than the closest range distance subtracted from the farthest range distance $R_0 - R_1$, then the changes in look angle $\Delta\theta$ may be neglected:

$$\Delta\theta = \tan^{-1}\frac{R_0}{H} - \tan^{-1}\frac{R_1}{H} \simeq 0. \tag{4.1}$$

Most SAR systems satisfy the height restraint given above. However, a low-altitude SAR system like YSAR [8] with highly varying incidence angles will exhibit range-dependent effects in the phase errors. This section describes the cause of these range dependent effects.

The angle θ may be derived from the change in the range from the closest range to the farthest range. Using the geometry in Fig. 4.1, the incidence angle is

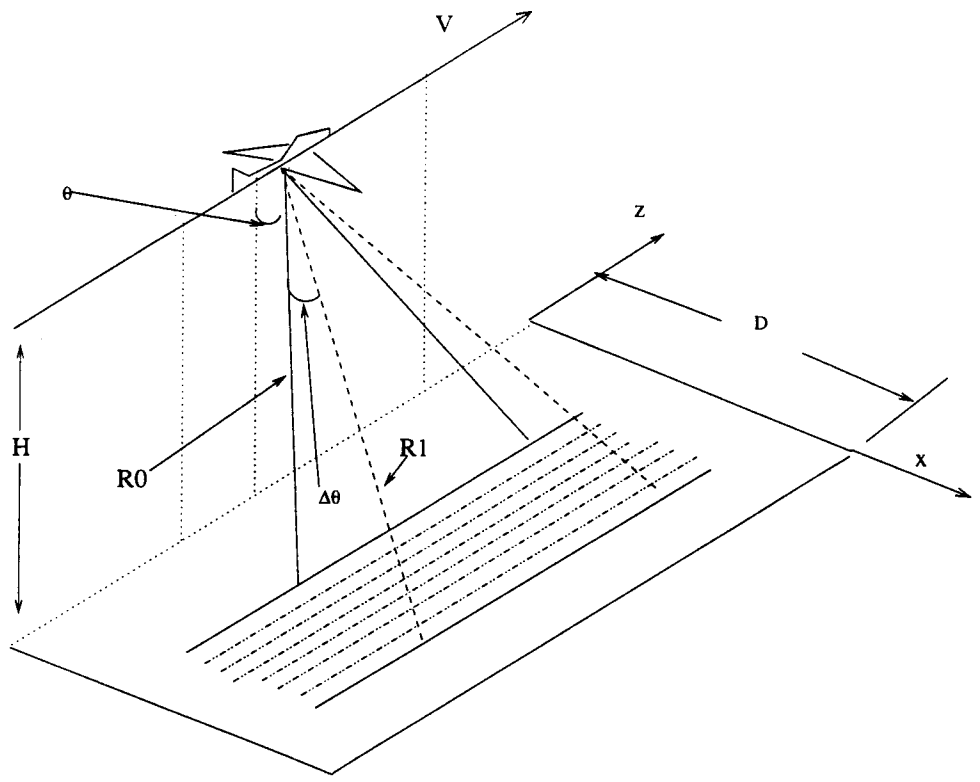

Figure 4.1: An airplane as the radar platform, flying at altitude H, in the z direction, with the closest range as $R0$ and the farthest range as $R1$ is shown. If H is much larger than the closest range distance subtracted from the farthest range distance $R_0 - R_1$, then the changes in look angle $\Delta\theta$ may be neglected

written for the n_{th} range bin as

$$\theta_n = \cos^{-1}\left(\frac{H}{R_0 + \Delta R}\right). \tag{4.2}$$

Assume the instrument platform is flying with constant velocity in the direction of increasing z, with the nominal trajectory following $x = y = 0$, as shown in Fig. 4.1. Then the phase error due to the trajectory variance is written by

$$\phi(t, \theta) = \frac{4\pi}{\lambda}(R_0 - R_1). \tag{4.3}$$

Using basic trigonometry R_0 is rewritten in terms of H and D as

$$R_0 = \sqrt{H^2 + D^2}. \tag{4.4}$$

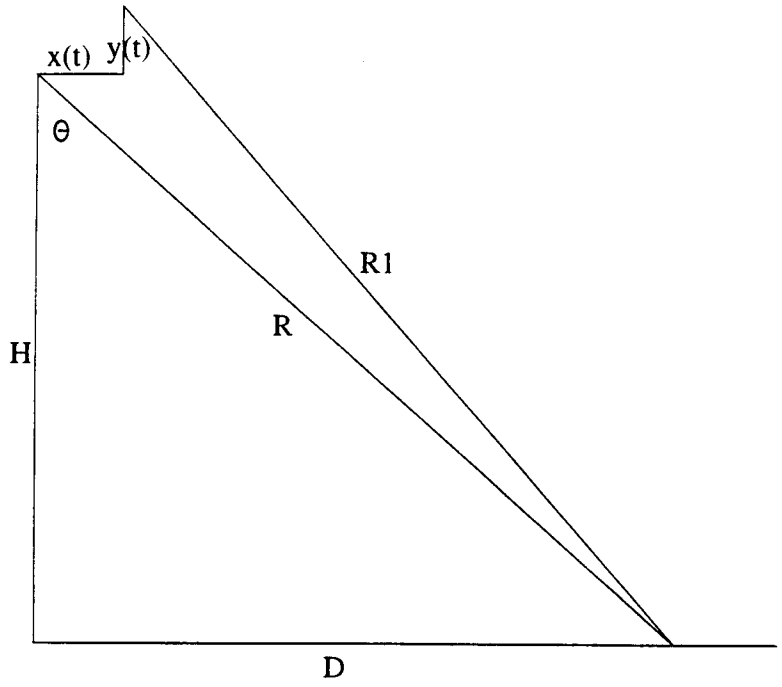

Figure 4.2: A Transverse Motion Geometry for the Range Dependent SAR shown in Fig. 4.1

R_1 is written, expanded and factored giving

$$\begin{aligned} R_1 &= \sqrt{(H+y(t))^2+(D-x(t))^2} \\ &= \sqrt{H^2+2Hy(t)+y^2(t)+D^2-2Dx(t)+x(t)^2} \\ &= \sqrt{H^2+D^2}\sqrt{1+\frac{2Hy(t)+y^2(t)-2Dx(t)+x(t)^2}{H^2+D^2}}. \end{aligned} \tag{4.5}$$

Assuming $H >> y(t)$ and $D >> x(t)$ allows two approximations. The fist approximates $\frac{x(t)^2}{H^2+D^2}$ and $\frac{y(t)^2}{H^2+D^2} \approx 0$, and the second states that if $a << 1$ then $\sqrt{1+a} \approx 1+\frac{a}{2}$ by a two term Taylor expansion. Thus, R_1 can be approximated as,

$$\begin{aligned} R_1 &\approx \sqrt{H^2+D^2}\sqrt{1+\frac{2Hy(t)-2Dx(t)}{H^2+D^2}} \\ &\approx \sqrt{H^2+D^2}\left(1+\frac{Hy(t)-Dx(t)}{H^2+D^2}\right). \end{aligned} \tag{4.6}$$

Then by using the definition of cos and sin, R_1 may be written as

$$R_1 \approx R_1 + y(t)\cos(\theta) - x(t)\sin(\theta) \tag{4.7}$$

$$\phi(t,\theta) = \frac{4\pi}{\lambda}(-x(t)\sin(\theta) + y(t)\cos(\theta)). \tag{4.8}$$

Now we have two parameters of phase error to estimate for each azimuth position: $\hat{\phi}_x = -\frac{4\pi}{\lambda}x(t)$ and $\hat{\phi}_y = \frac{4\pi}{\lambda}y(t)$.

4.2 Phase Weighted Estimation

The maximum likelihood method is known to be optimal for the noise model used [4]. Thus, a logical first approach would be to apply this method to the range-dependent problem. In the ML approach, the argument of the summed target responses across all range bins is used as the estimated angle of the phase error, as shown in Eq. (3.17). The sum located inside the angle in Eq. (3.17) inhibits direct implementation the range dependence found in Eq. (4.8). The ML range dependent derivation does not seem to have a closed solution.

To overcome this problem, a new algorithm which allows a simple closed form solution to estimate the phase gradient for a range-dependent version was found. The phase error of the image is convolved with phase noise from two different sources from the movement of the platform. The first source is thermal noise, and the second source is phase errors created from nearby scatterers that is treated as noise. The thermal phase noise may be found by representing two azimuth adjacent responses, modeled with independent phase noise. The relationship between the SNR and the standard deviation of the phase noise between two pixels is shown in Fig. 4.3. The standard deviation derived from the PDF, which is a function of the correlation of the two responses, is a function of the SNR. The PDF was originally developed for application in interferometry, but may be used with any two returns that have independent noise and a spatial relationship. For a detailed development, see [13].

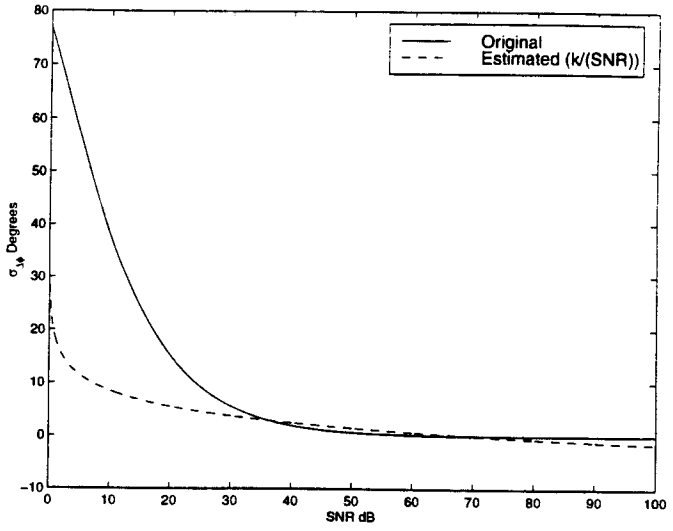

Figure 4.3: The relationship between the SNR and standard deviation between two independent returns is seen to be nearly linear for an SNR above 30dB.

Figure 4.3 was computed numerically by using thermal phase correlation γ given by,

$$\gamma = \frac{1}{1 + SNR^{-1}}, \tag{4.9}$$

in the PDF [13] given by,

$$\begin{aligned} \text{pdf}(\phi) &= \frac{1-|\gamma|^2}{2\pi} \frac{1}{1-|\gamma|^2\cos^2(\phi-\phi_o)} \times \\ &\left\{1 + \frac{|\gamma|\cos(\phi-\phi_o)\cos^{-1}[-|\gamma|\cos(\phi-\phi_o)]}{[1-|\gamma|^2\cos^2(\phi-\phi_o)]^{1/2}}\right\}. \end{aligned} \tag{4.10}$$

ϕ is the phase difference of the two pixels and ϕ_o is defined by

$$\phi_o = \arg\{\gamma\}. \tag{4.11}$$

Observing Fig. 4.3 reveals that the variance of ϕ is inversely related to the SNR, for SNR values more than 30db. The approximation for phase variance is given by,

$$\sigma^2_{\Delta\phi} \approx \frac{k}{SNR} \tag{4.12}$$

Where k is an arbitrary constant.

The second source of phase variance is due to close proximity scatterers. These scatterers are often modeled as white noise. A relationship of the scatterers is introduced below.

The data model used in the ML PGA, models all scatterers, except the center shifted largest magnitude pixel, as white noise. This model when used in the ML PGA provides a good phase estimation for the 1st derivative,

$$\frac{\partial \angle(\phi_e(t))}{\partial t} = \frac{\partial \angle(r(t))}{\partial t}. \tag{4.13}$$

An example of the non-white scatterers can be seen when two prominent scatterers, A and B, are seen in the spotlight case shown below:

$$r(t) = [Ae^{j\theta_A} + Be^{j\frac{-2\pi v^2 t_2^2}{\lambda R}+\theta_B}e^{j\frac{-2\pi v^2}{\lambda R}(2t_2 t)}]e^{j\phi_e(t)}. \tag{4.14}$$

The response of two targets located within the same azimuth line in the spotlight case is represented in Eq. (4.14). A is the first scatterer which has been center shifted to remove the linear phase term and B is second with θ_A and θ_B as the inherent phase of A and B respectively, and ϕ_e is the phase error. The first derivative is taken to show the resulting relation for the phase noise introduced.

The total angle of the scatterer is found by taking the *arctan* of the imaginary over the real parts of Eq. (4.14),

$$\begin{aligned} \angle r(t) &= \tan^{-1}\left(\frac{imag}{real}\right) \\ & tan^{-1}\left(\frac{(A\sin(\theta_A+\phi_e(t)) + B\sin(\theta_B + c_1t_2^2 + c_1t_2t + \phi_e(t)))}{(A\cos(\theta_A+\phi_e(t)) + B\cos(\theta_B + c_1t_2^2 + c_1t_2t + \phi_e(t)))}\right). \end{aligned} \tag{4.15}$$

The first derivative of the phase is taken to give

$$\frac{\partial \angle(r(t))}{\partial t} = \partial\phi(t) + \frac{Bc_1t_2A\cos(\theta_A - c_1 + \theta_B - c_1 2t_2 t) + B^2c_1t_2}{2AB\cos(\theta_A - c_1 + \theta_B - c_1 2t_2 t) + A^2 + B^2}. \tag{4.16}$$

The first derivative shows that the dominant term will be $\frac{\partial\phi(t)}{\partial t}$ only if $A >> B$ and t_2 is small. In this case the A^2 term will dominate when the phase is estimated. With the model of two adjacent pixels given above, the term t_2 is forced to be small, thus the equation reduces to the estimate of the derivative of the phase error. The

majority of the noise may be modeled as the thermal noise discussed above. Using the model of the thermal noise the model given is.

$$\sigma^2_{\Delta\phi} = \frac{1}{SNR}. \tag{4.17}$$

Accordingly, the new method weights the phase measurements by the magnitude of the corresponding pixel. This construction avoids the problems of the angle taken after the sum in Eq. (3.17) and is easily extended to the range dependent case. This method is called Phase Weighted Estimation (PWE). The PWE is optimal in the weighted least squares sense. The least squares data model is

$$\mathbf{Y} = \mathbf{X}\Delta\Phi_\mathbf{e} + \epsilon\,, \tag{4.18}$$

where $\mathbf{Y}$ is the column vector with the measured angle differences, $\mathbf{X}$ is a column of ones, $\Delta\phi_\mathbf{e}$ is the phase estimate and ϵ is a column of phase noise. Let $g_{n,m}$ denote the image in the range-compressed domain, with n indicating the range bin and m the azimuth bin. The phase gradient, denoted $\Delta\phi_{n,m}$, is

$$\Delta\phi_{n,m} = \angle[\bar{g}_{n,m-1}\bar{g}^*_{n,m}] \tag{4.19}$$

With Y, X, and $\Delta\Phi_e$ given by

$$\mathbf{Y} = [\Delta\phi_1\ \Delta\phi_2\ \ldots\ \Delta\phi_N]^T \tag{4.20}$$

$$\mathbf{X} = [1\ 1\ \ldots\ 1]^T \tag{4.21}$$

$$\widehat{\Delta\Phi_e} = [\widehat{\Delta\phi_{e\,1,m}}\ \widehat{\Delta\phi_{e\,2,m}}\ \ldots\ \widehat{\Delta\phi_{e\,N,m}}]^T. \tag{4.22}$$

The matrix $\mathbf{L}$ consists of the weights. $\mathbf{L}$ is a linear transformation such that

$$\begin{aligned} \epsilon^* &= \mathbf{L}\epsilon \\ V(\epsilon^*) &= \mathbf{L}V\epsilon\mathbf{L^T} = k^2\mathbf{I}. \end{aligned} \tag{4.23}$$

If

$$\mathbf{L} = \begin{bmatrix} l_1 & 0 & \ldots & 0 \\ 0 & l_2 & \ldots & 0 \\ \vdots & \vdots & \ddots & \vdots \\ 0 & 0 & \ldots & l_N \end{bmatrix}$$

then

$$\begin{bmatrix} l_1 & 0 & \dots & 0 \\ 0 & l_2 & \dots & 0 \\ \vdots & \vdots & \ddots & \vdots \\ 0 & 0 & \dots & l_N \end{bmatrix} \begin{bmatrix} \sigma_1^2 & 0 & \dots & 0 \\ 0 & \sigma_2^2 & \dots & 0 \\ \vdots & \vdots & \ddots & \vdots \\ 0 & 0 & \dots & \sigma_N^2 \end{bmatrix} \begin{bmatrix} l_1 & 0 & \dots & 0 \\ 0 & l_2 & \dots & 0 \\ \vdots & \vdots & \ddots & \vdots \\ 0 & 0 & \dots & l_N \end{bmatrix} = \begin{bmatrix} \sigma^2 & 0 & \dots & 0 \\ 0 & \sigma^2 & \dots & 0 \\ \vdots & \vdots & \ddots & \vdots \\ 0 & 0 & \dots & \sigma^2 \end{bmatrix}.$$

Multiplying the above equation and equating vectors gives,

$$\sigma_i^2 l_1^2 = k^2. \tag{4.24}$$

Solving for l gives,

$$l = \sqrt{\frac{k^2}{\sigma_i^2}}. \tag{4.25}$$

Substituting the model in Eq. (4.17) gives,

$$l = \sqrt{SNR}. \tag{4.26}$$

If the gradient of the phase is found using the ML technique used in the previous chapter, then the resultant pixel g_d, with the phase as the first difference, is given by,

$$\begin{aligned} g_{d\,n,m} &= |g_{n,m-1} g_{n,m}^*| e^{\angle (g_{n,m-1} g_{n,m}^*)} \\ \Delta\phi &= \angle [g_{n,m-1} g_{n,m}^*] \end{aligned} \tag{4.27}$$

Assuming the magnitude of neighboring pixels is approximately the same, the power measurement SNR is proportional to $g_{d\,n,m}$ and gives,

$$\mathbf{L} = \begin{bmatrix} \sqrt{|g_{d\,1,m}|} & 0 & \dots & 0 \\ 0 & \sqrt{|g_{d\,2,m}|} & \dots & 0 \\ \vdots & \vdots & \ddots & \vdots \\ 0 & 0 & \dots & \sqrt{|g_{d\,N,m}|} \end{bmatrix}. \tag{4.28}$$

Implementing the linear transformation gives

$$\mathbf{Y}^* = \mathbf{X}^* \Phi_{\mathbf{e}} + \epsilon^*, \tag{4.29}$$

where $\mathbf{Y}^* = \mathbf{LY}$ and $\mathbf{X}^* = \mathbf{LX}$. The least-squares estimators of the parameters are given by

$$\mathbf{X^T L^T L X}\hat{\theta} = \mathbf{X^T L^T L Y}. \tag{4.30}$$

If the data set is nonzero then $\mathbf{X^T L^T L X}$ is nonzero. The inverse is guaranteed exist because $\mathbf{X^T L^T L X}$ is non-zero scaler. The estimated parameter $\widehat{\Delta\Phi_e}$ is given by

$$\widehat{\Delta\Phi_e} = \{\mathbf{X^T L^T L X}\}^{-1}\mathbf{X^T L^T L Y}. \tag{4.31}$$

Substituting the variables in this equation gives the solution for $\widehat{\Delta\phi_n}$ as

$$\widehat{\Delta\phi}_{e\,m} = \frac{\sum_{k=1}^{N}\left(|(g_{n,m}g^*_{n,m-1})|\angle(g_{n,m}g^*_{n,m-1})\right)}{\sum_{k=1}^{N}|(g_{n,m}g^*_{n,-1})|}. \tag{4.32}$$

This algorithm is easily extended to the range-dependent case by curve fitting $\mathbf{X}$ to the range dependent model derived in Eq. (4.8). The phase weighting of the inverse of the SNR remains the same. Range curve fitting is added, and a system of equations indexed by range bin n models the phase curve of the image. Let $\widehat{\Delta\phi}_{\mathbf{m}}$ be the 2×1 vector of phase estimates, and $\mathbf{X}$ be the Nx2 matrix made up of the *sine* values in the first column and the *cosine* values in the second:

$$\widehat{\Delta\phi}_{\mathbf{m}} = \left[\widehat{\phi}_{x,n} \quad \widehat{\phi}_{y,n}\right]^T, \tag{4.33}$$

$$\mathbf{X} = \begin{bmatrix} \sin(\theta_0) & \cos(\theta_0) \\ \sin(\theta_1) & \cos(\theta_1) \\ \vdots & \vdots \\ \sin(\theta_N) & \cos(\theta_N) \end{bmatrix}. \tag{4.34}$$

Following the same steps as before, the weighted phase gradient is represented by

$$\widehat{\Delta\Phi_m} = \{\mathbf{X^T L^T L X}\}^{-1}\mathbf{X^T L^T L Y}. \tag{4.35}$$

If the data set is nonzero then $\mathbf{X^T L^T L X}$ is nonzero, and a solution exists. The solution is not unique, but it is not required to be. Any solution that estimates the phase error gradient at all range bins is sufficient. This gradient is then integrated and applied in the same way as in the original PGA algorithm in chapter 3.

4.3 Phase Weighted Estimation Results

The new PWE range dependant PGA algorithm was tested using synthetic phase errors on three different images. Each image has unique characteristics to thoroughly test the new algorithm. The three images are a desert image with no prominent scatterers Figs. 4.4 through 4.15, a mountain image with distributed targets of varying amplitudes Figs. 4.16 through 4.27, and an urban scene with many bright scatterers in close proximity Figs. 4.28 through 4.51. The spotlight PGA was shown to give good results with all three images. The non-range dependent PWE is compared to the ML for comparison.

The original, corrupted and restored images are all similar to those presented in Chapter 3 because of the accuracy with which the algorithm estimated the phase. To compare the results to the ML, the original images were first blurred with the non-range dependent phase error and then restored with the ML PGA and PWE PGA. In Figs. 4.16, 4.17, 4.28, 4.29, 4.4, 4.5 the applied phase error is compared with the maximum likelihood and the phase weighted estimation. For these tests, the PWE has a final better convergence than the ML algorithm, but has a significantly slower convergence rate, requiring more iterations. The three images are blurred with the range dependent phase error model derived in Eq. (4.8). Using the range dependent PWE, the errors are removed with the same accuracy as the non-range dependent maximum likelihood PGA. The estimated and applied phase errors for ϕ_x and ϕ_y are shown in Figs. 4.18 through 4.15. The ϕ_x and ϕ_y sometimes vary from the original error, but the combinations in the different range lines are accurate below one radian standard deviation.

A high frequency phase error was applied to the urban image to test the high frequency estimation of the algorithm. The high frequency was estimated to the same accuracy of the low frequency phase errors as shown in Figs. 4.40 through 4.51.

4.3.1 Desert Image: No Significant Scatterers

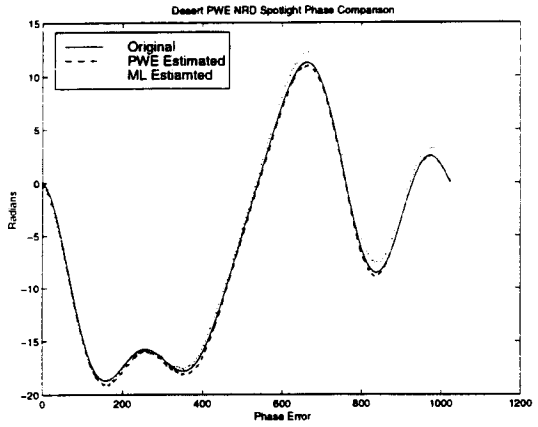

Figure 4.4: Phase error comparison. Non-range dependent PWE, ML spotlight desert image.

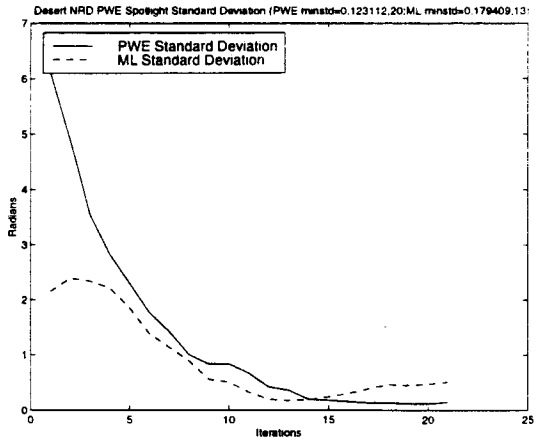

Figure 4.5: The standard deviation. Non-range dependent PWE, ML spotlight desert image.

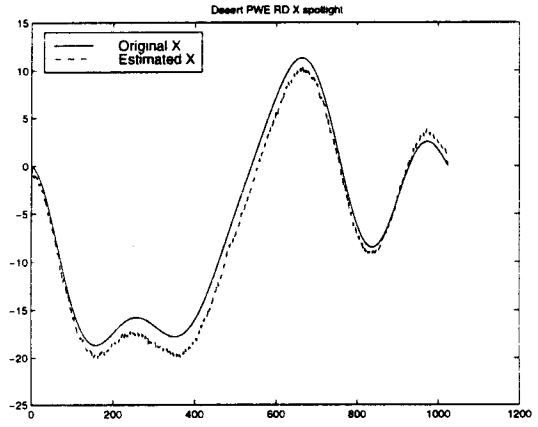

Figure 4.6: Phase error comparison. Range dependent PWE X spotlight desert image.

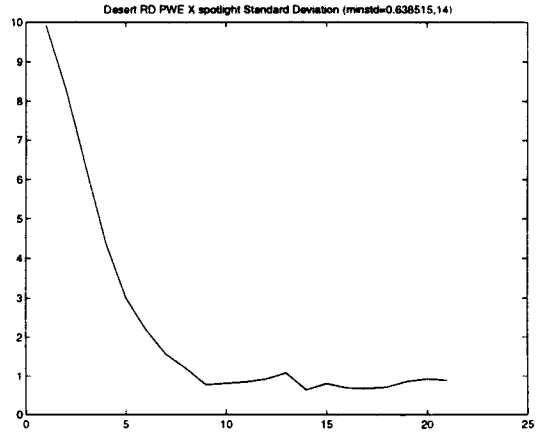

Figure 4.7: The standard deviation. Range dependent PWE X spotlight desert image.

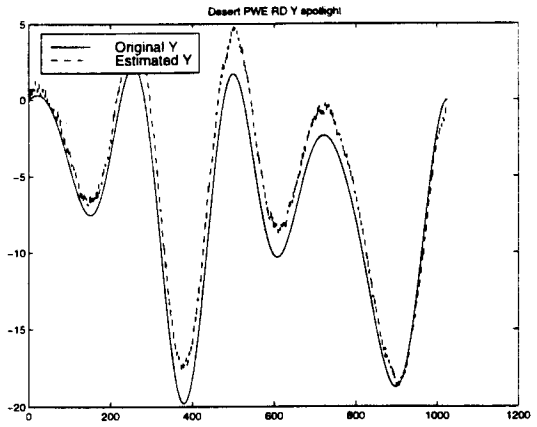

Figure 4.8: Phase error comparison Y. Range dependent PWE spotlight desert image.

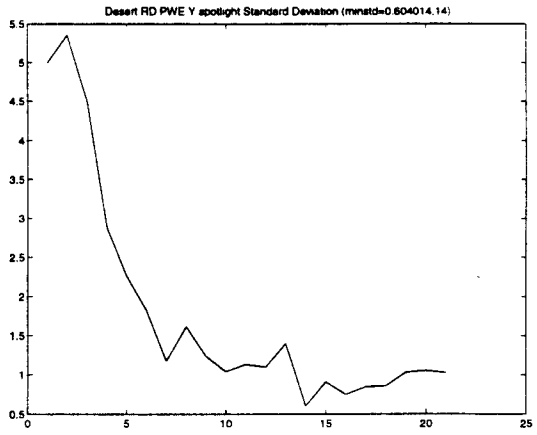

Figure 4.9: Phase standard deviation Y. Range dependent PWE spotlight desert image.

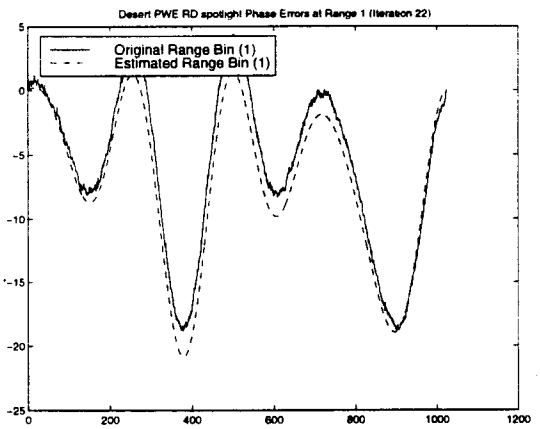

Figure 4.10: Phase error comparison. Range dependent PWE spotlight desert image. (Range Bin 1)

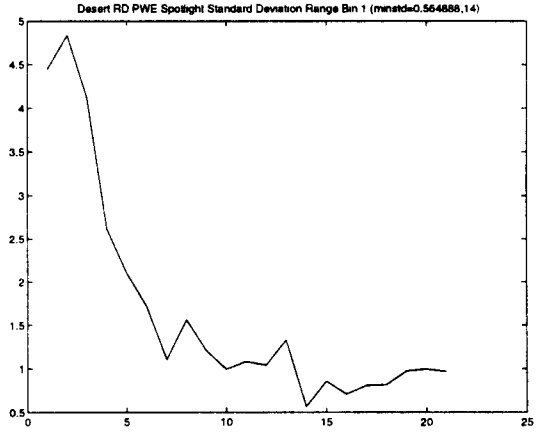

Figure 4.11: The standard deviation. Range dependent PWE spotlight desert image. (Range Bin 1)

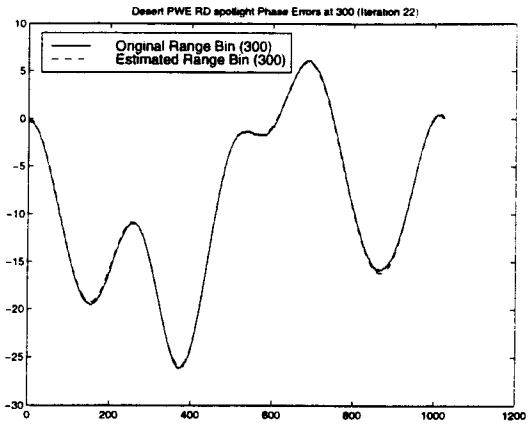

Figure 4.12: Phase error comparison. Range dependent PWE spotlight desert image. (Range Bin 300)

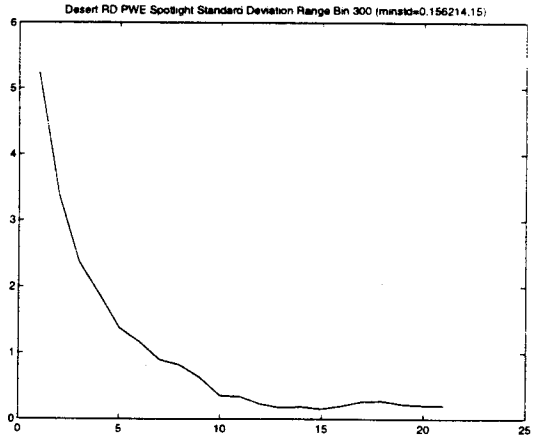

Figure 4.13: The standard deviation. Range dependent PWE spotlight desert image. (Range Bin 300)

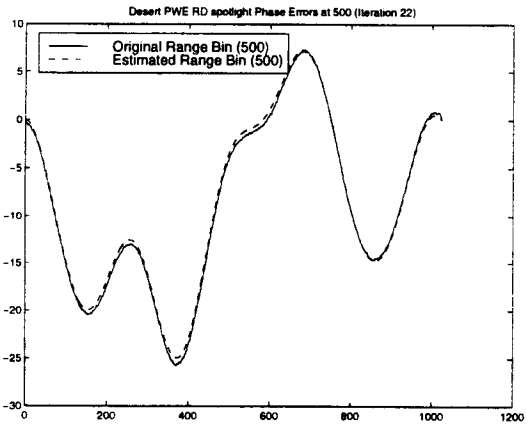

Figure 4.14: Phase error comparison.Range dependent PWE spotlight desert image. (Range Bin 500)

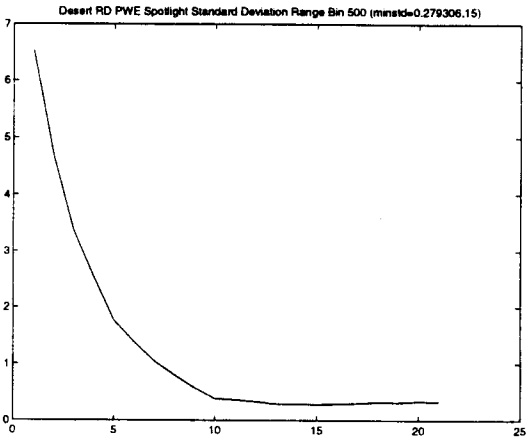

Figure 4.15: The standard deviation X. Range dependent PWE spotlight desert image. (Range Bin 500)

4.3.2 Mountain Image: Some Significant Scatterers

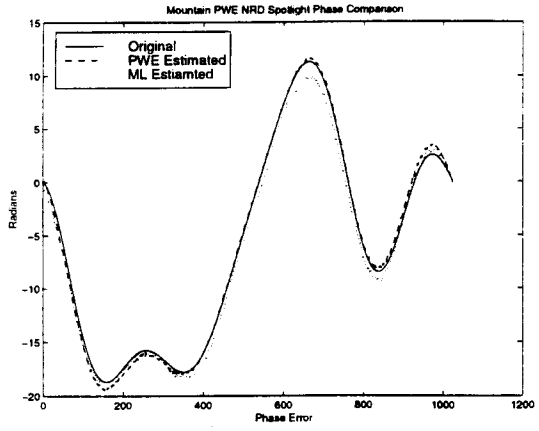

Figure 4.16: Phase error comparison. Non-range dependent PWE, ML spotlight mountain image.

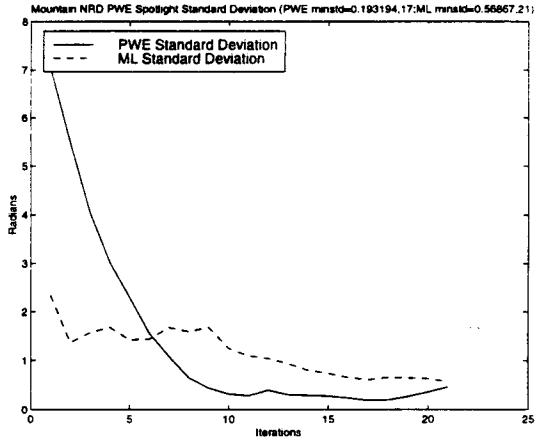

Figure 4.17: The standard deviation. Non-range dependent PWE, ML spotlight mountain image.

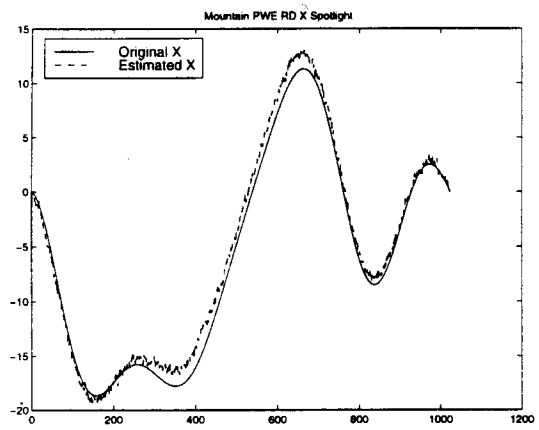

Figure 4.18: Phase error X comparison. Range dependent PWE spotlight mountain image.

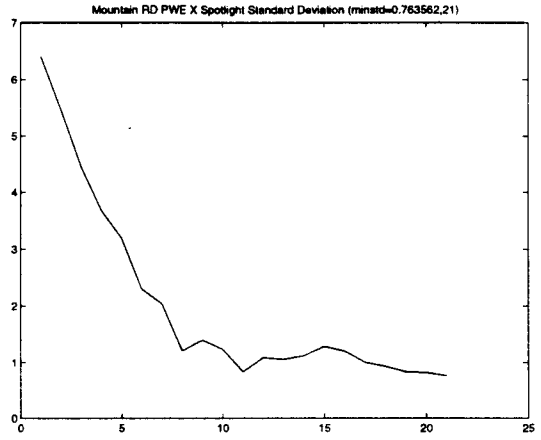

Figure 4.19: The standard deviation X comparison. Range dependent PWE spotlight mountain image.

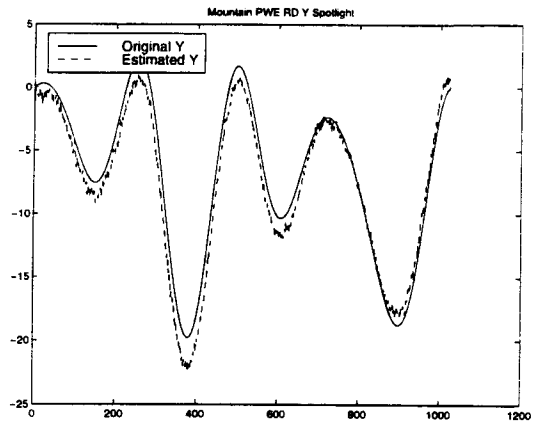

Figure 4.20: Phase error Y comparison. Range dependent PWE spotlight mountain image.

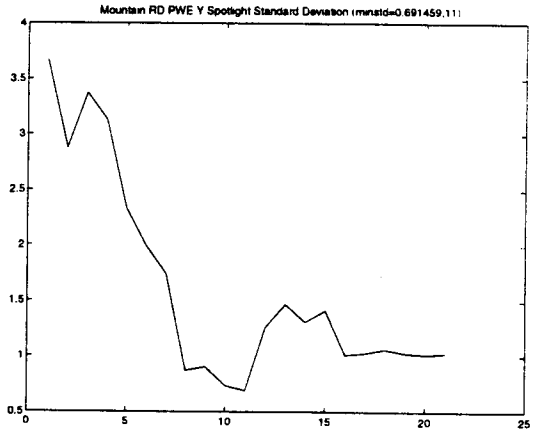

Figure 4.21: The standard deviation Y comparison. Range dependent PWE spotlight mountain image.

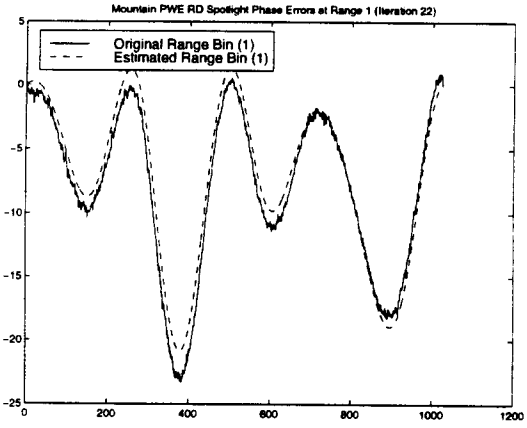

Figure 4.22: Phase error comparison. Range dependent PWE spotlight mountain image. (Range Bin 1)

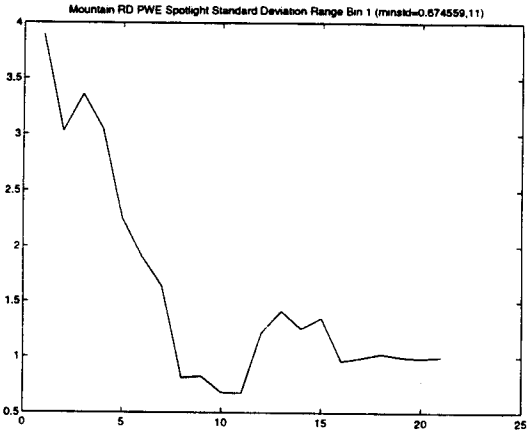

Figure 4.23: The standard deviation. Range dependent PWE spotlight mountain image. (Range Bin 1)

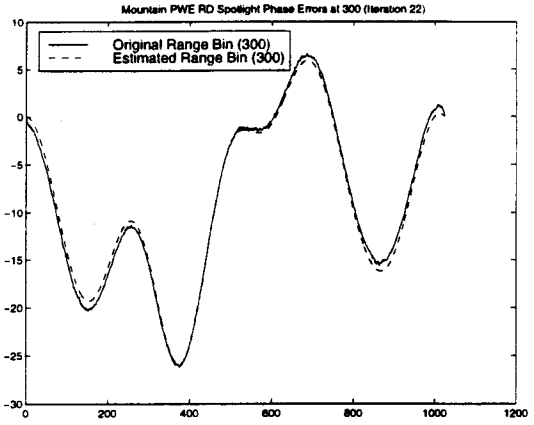

Figure 4.24: Phase error comparison. Range dependent PWE spotlight mountain image. (Range Bin 300)

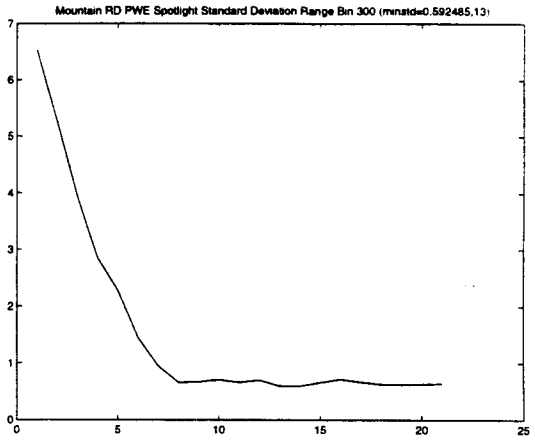

Figure 4.25: The standard deviation. Range dependent PWE spotlight mountain image. (Range Bin 300)

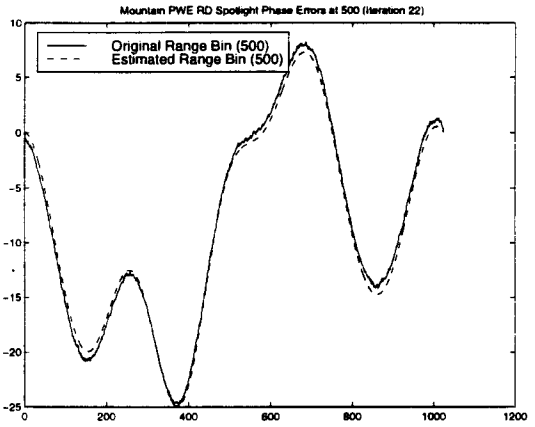

Figure 4.26: Phase error comparison. Range dependent PWE spotlight mountain image. (Range Bin 500)

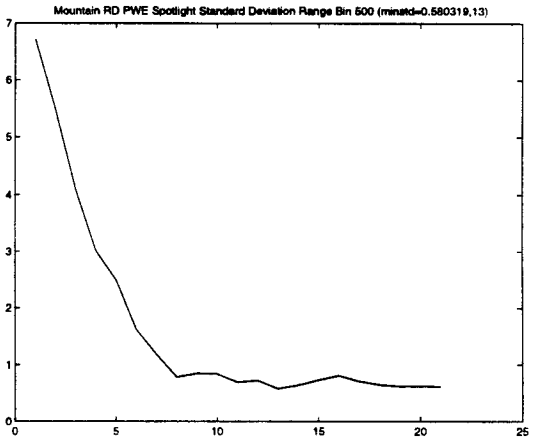

Figure 4.27: The standard deviation. Range dependent PWE spotlight mountain image. (Range Bin 500)

4.3.3 Urban Image: Many Significant Scatterers

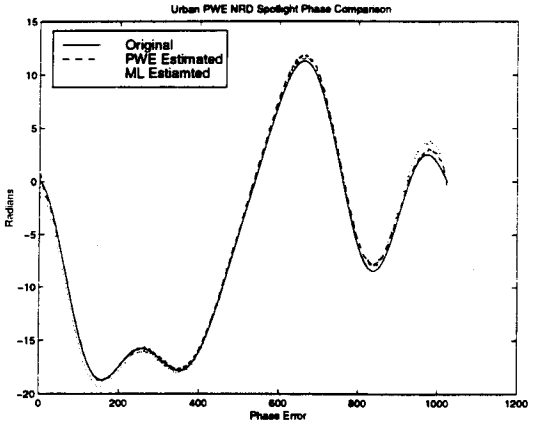

Figure 4.28: Phase error comparison. Non-range dependent PWE, ML spotlight Urban image.

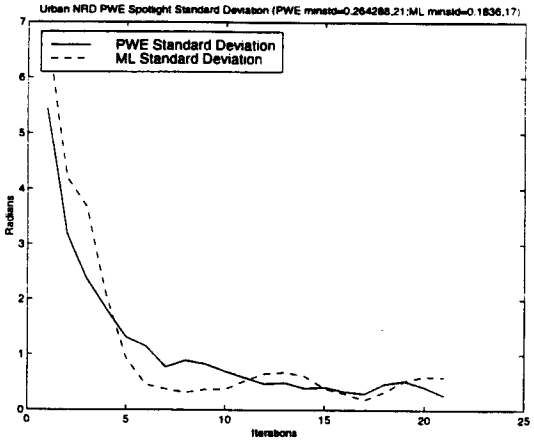

Figure 4.29: The standard deviation. Non-range dependent PWE, ML spotlightUrban image.

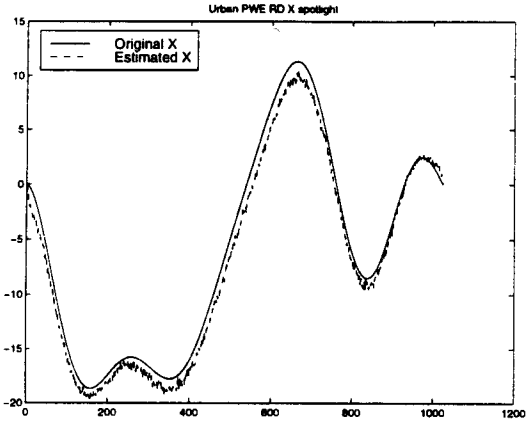

Figure 4.30: Phase error comparison X. Range dependent PWE spotlight urban image.

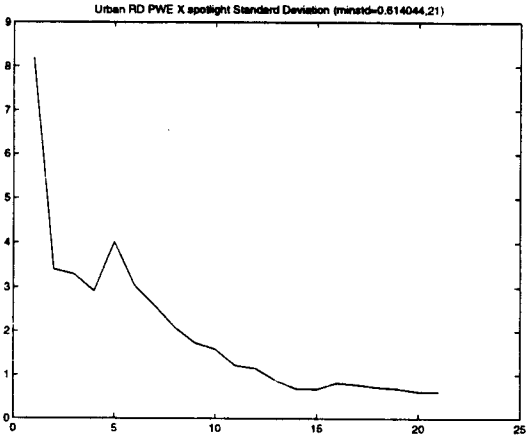

Figure 4.31: The standard deviation X. Range dependent PWE spotlight urban image.

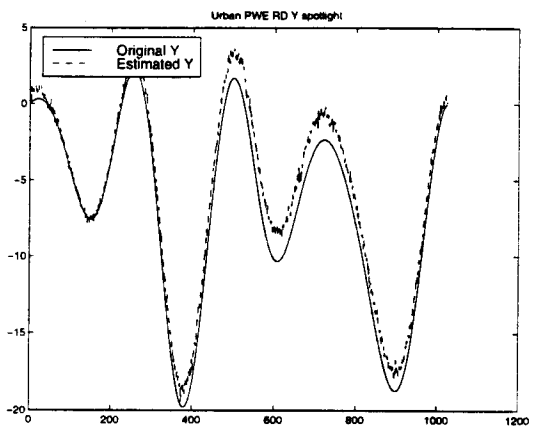

Figure 4.32: Phase error comparison Y. Range dependent PWE spotlight urban image.

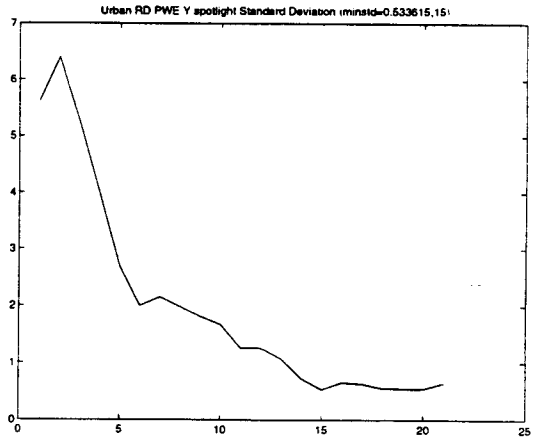

Figure 4.33: The standard deviation Y. Range dependent PWE spotlight urban image.

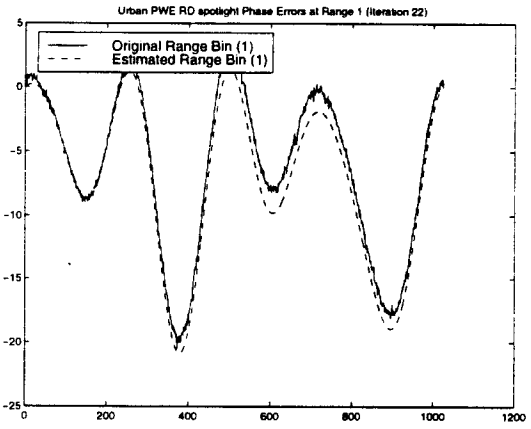

Figure 4.34: Phase error comparison. Range dependent PWE spotlight urban image. (Range Bin 1)

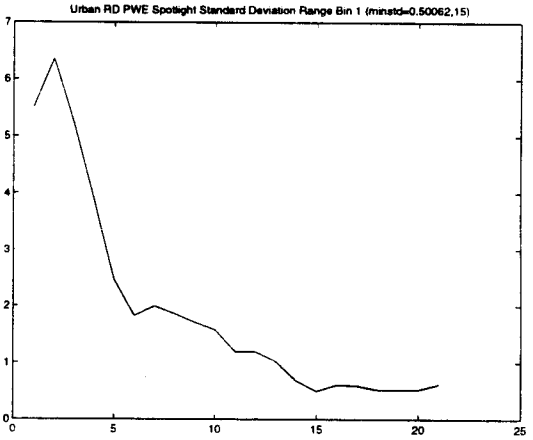

Figure 4.35: The standard deviation. Range dependent PWE spotlight urban image. (Range Bin 1)

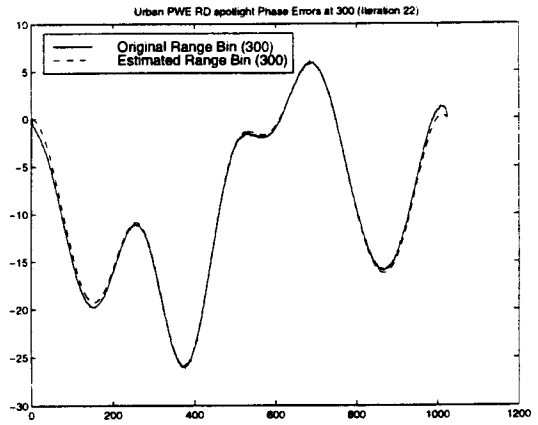

Figure 4.36: Phase error comparison. Range dependent PWE spotlight urban image. (Range Bin 300)

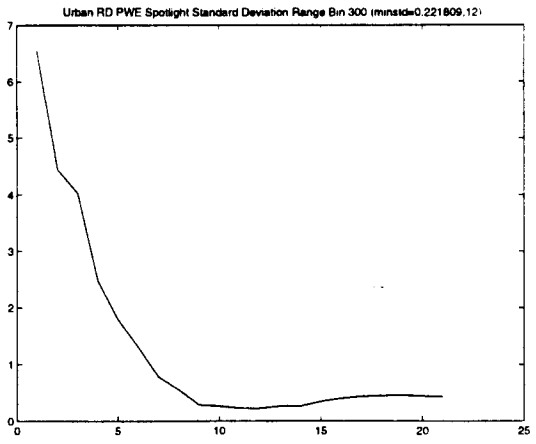

Figure 4.37: The standard deviation. Range dependent PWE spotlight urban image. (Range Bin 300)

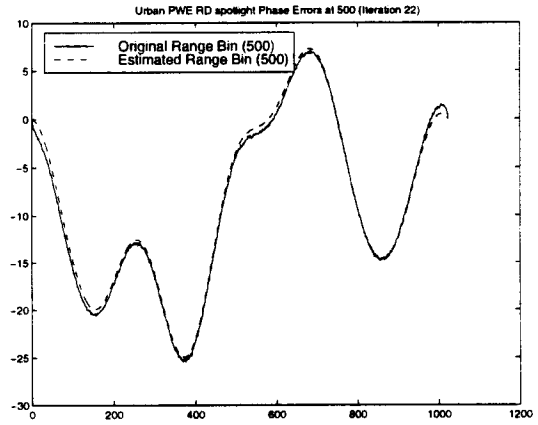

Figure 4.38: Phase error comparison. Range dependent PWE spotlight urban image. (Range Bin 500)

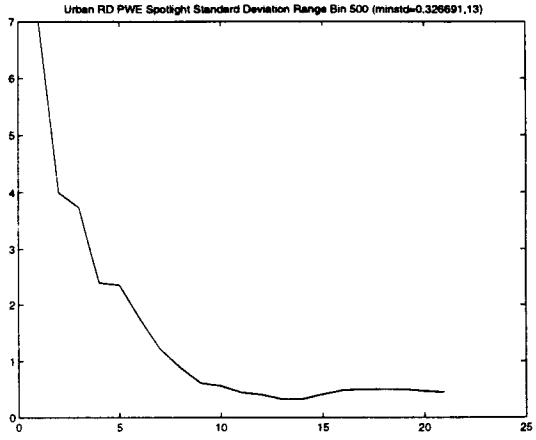

Figure 4.39: The standard deviation. Range dependent PWE spotlighturban image. (Range Bin 500)

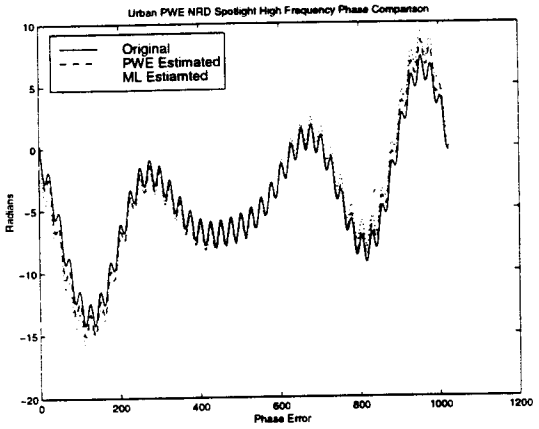

Figure 4.40: Phase error comparison. Non-range dependent high frequency error PWE, ML spotlight Urban image.

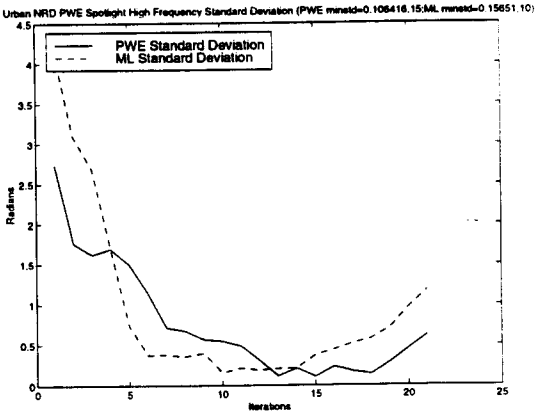

Figure 4.41: The standard deviation. Non-range dependent high frequency error PWE, ML spotlightUrban image.

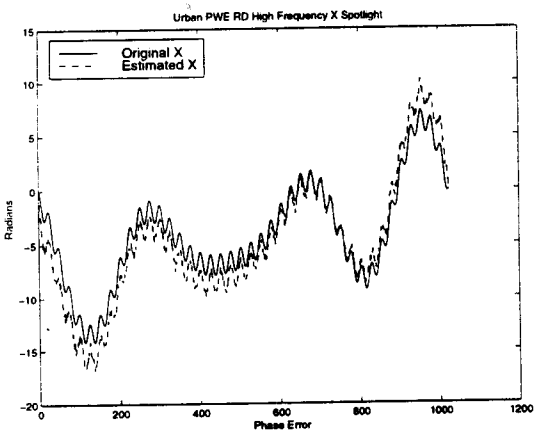

Figure 4.42: Phase error comparison X. Range dependent high frequency error PWE spotlight urban image.

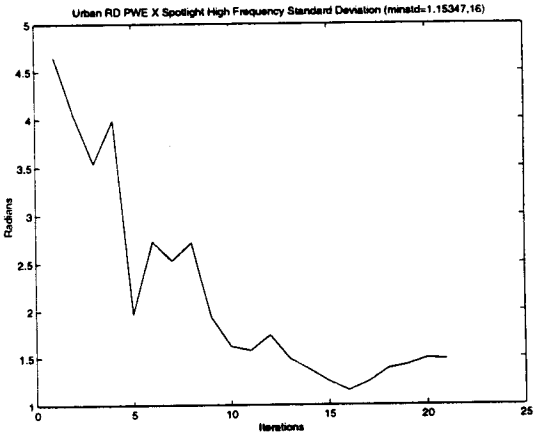

Figure 4.43: The standard deviation X. Range dependent high frequency error PWE spotlight urban image.

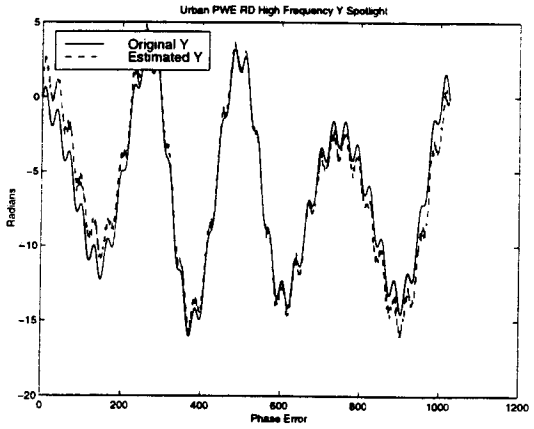

Figure 4.44: Phase error comparison Y. Range dependent high frequency error PWE spotlight urban image.

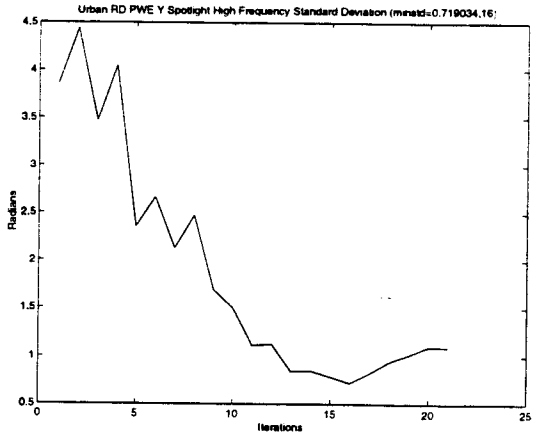

Figure 4.45: The standard deviation Y. Range dependent high frequency error PWE spotlight urban image.

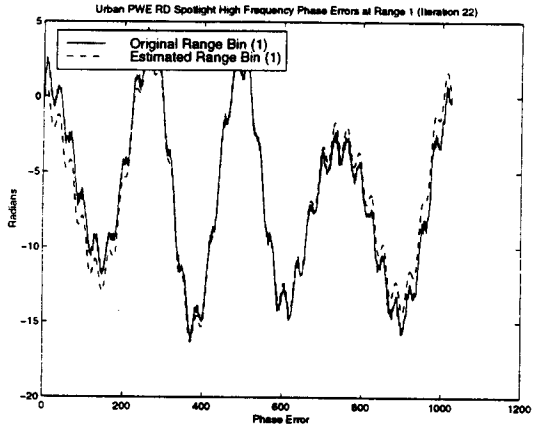

Figure 4.46: Phase error comparison. Range dependent high frequency error PWE spotlight urban image. (Range Bin 1)

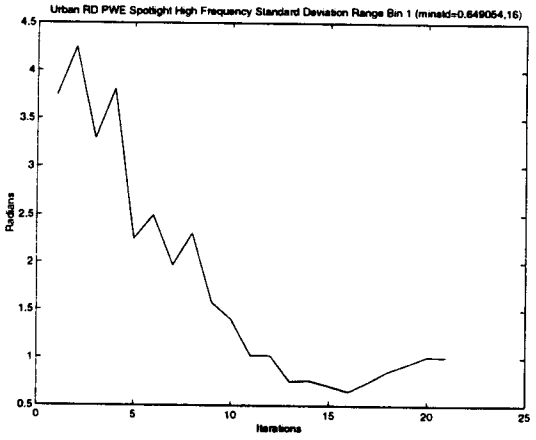

Figure 4.47: The standard deviation. Range dependent high frequency error PWE spotlight urban image. (Range Bin 1)

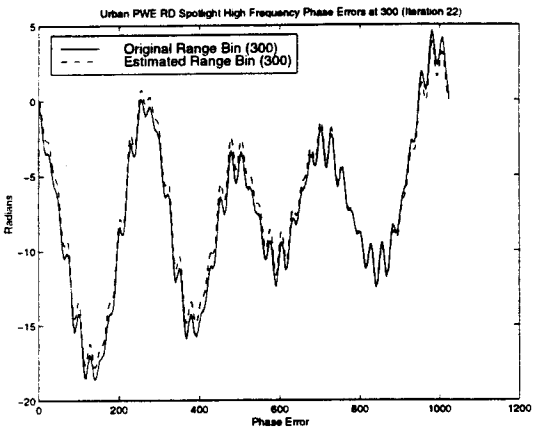

Figure 4.48: Phase error comparison. Range dependent high frequency error PWE spotlight urban image. (Range Bin 300)

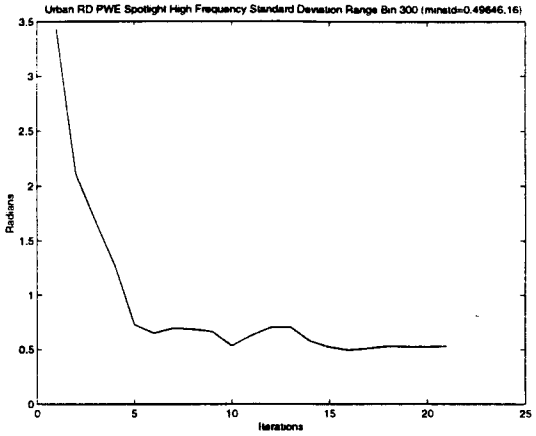

Figure 4.49: The standard deviation. Range dependent high frequency error PWE spotlight urban image. (Range Bin 300)

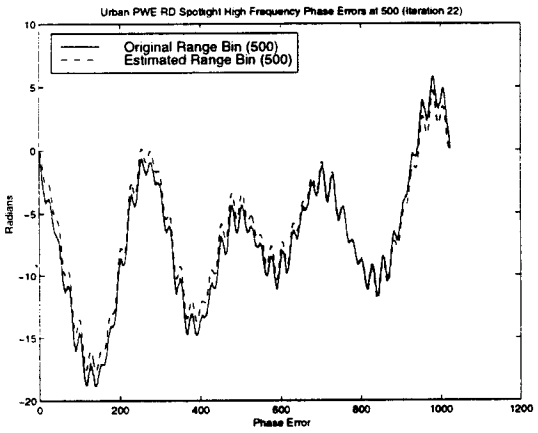

Figure 4.50: Phase error comparison. Range dependent high frequency error PWE spotlight urban image. (Range Bin 500)

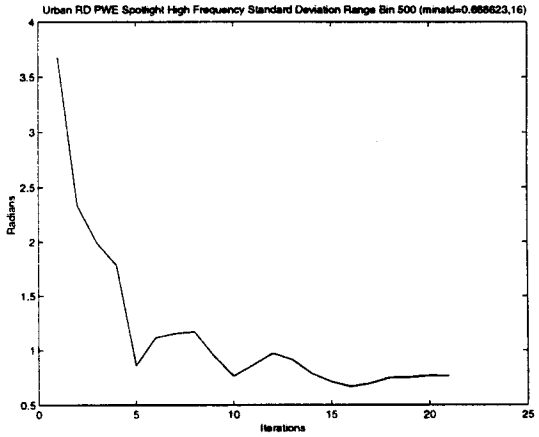

Figure 4.51: The standard deviation. Range dependent high frequency error PWE spotlight urban image. (Range Bin 500)

Chapter 5

Stripmap Phase Estimation

The autofocus algorithms discussed in Chapters 3 and 4 cannot be used with stripmap SAR. Stripmap SAR has a fixed antenna which allows for much simpler and cheaper operation. Specifically, the spotlight algorithms use a Fourier transform method to compress images and stripmap SAR uses correlation compression. In stripmap, both the fully compressed image and range compressed image are in the time domain. Therefore, the window filtering step can not be used. Other problems include the phase history. Each pixel in a spotlight image contains the phase history for the whole image, but in stripmap the phase history is only as wide as the beam width in the azimuth direction. A possible solution is to convert the data to spotlight data. Two stripmap to spotlight converters have been introduced [9] [10]. These algorithms both make a narrow beam assumption and attempt to massage the stripmap data to be used with algorithms such as the range migration algorithm and the spotlight image formation algorithm [1] [2]. These algorithms cannot be easily converted to the range dependent problem. An alternative compression algorithm will be introduced to allow an altered PWE PGA algorithm to be used to estimate and correct the phase errors for non-range or range dependent stripmap systems. This method creates a Fourier transform relationship between the fully compressed image domain and the range compressed domain similar to that of a spotlight mode SAR.

5.1 Alternative Stripmap Azimuth Compression Method

To obtain the same relationship for the stripmap case, the SSC follows four steps. The four main steps for stripmap phase estimation are: (1) Windowing the

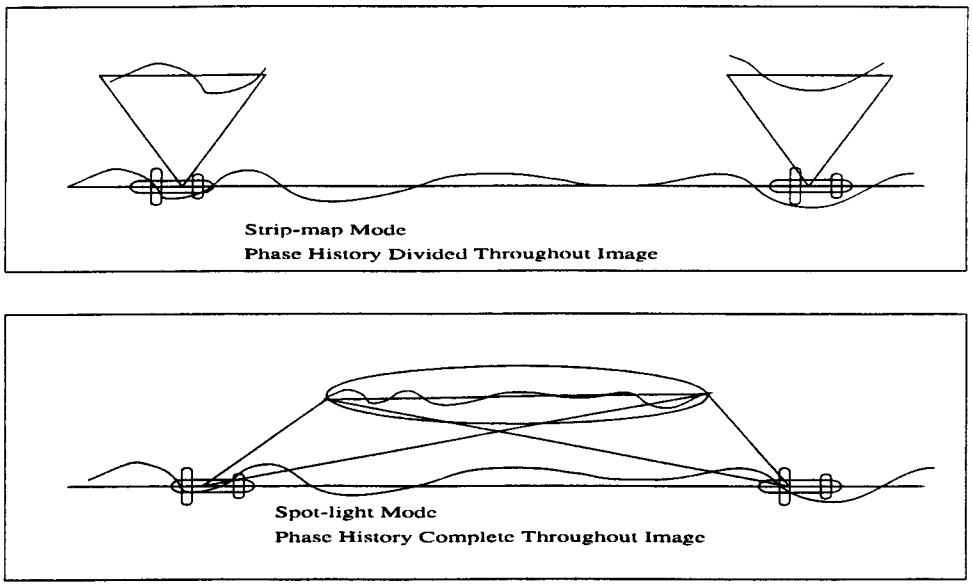

Figure 5.1: SAR Geometry Phase history Comparison

long stripmap data to smaller data chunks; (2) Multiplication by the conjugate of the chirp; (3) Fourier transform; (4) and Apply the Stripmap PWE PGA. The alternative compression method will be called the Stripmap Spotlight Compression method (SSC) because of the similarities with the general spotlight compression method. The spotlight mode range compressed data is described by

$$r_n(t) = [g_n(t)]e^{j\phi_e(t)}. \tag{5.1}$$

The azimuth compressed image domain is formed by taking the Fourier transform of $r(t)$ to yield,

$$a_n(t) = \mathcal{F}([g_n(t)]e^{j\phi_e(t)}) = \mathcal{F}g_n(\omega) \otimes \mathcal{F}e^{j\phi_e(\omega)}, \tag{5.2}$$

where $g_n(t)$ is the range compressed scatterer, $a_n(t)$ is the azimuth compressed domain or the image domain. The Fourier transform relationship between the two domains is very important to the windowing step in the PGA as discussed in Chapter 3.

5.1.1 Create Sections (Step 1)

In contrast to the spotlight case, the stripmap mode SAR does not illuminate one spot continuously. Rather the illumination changes continuously as can be seen in Fig. 5.1. The phase history in the traditionally generated fully compressed image is limited to the phase history that each pixel contains from its short illumination time. The main advantage of spotlight processing is the frequency-space relationship between the image domain and the range compressed, phase history domain. This relationship also causes the phase error to be convolved with the whole image. To achieve the same type of relationship for the stripmap case, a transform relationship between the phase history domain and the fully compressed domain must be made. Recall from Chapter 3 that the bandwidth of the spotlight SAR is much greater than that of stripmap SAR due to the immobile antenna. The measurable frequency is also limited by the sample rate in the azimuth direction of the radar. If a frequency-space relationship is made with the stripmap SAR, the size of the image is restricted by the maximum measurable frequency of the system. Starting with the model of the stripmap SAR range compressed data

$$r_{strip}(t) = [g_k(t) \otimes c(t) rect(t)] e^{j\phi_e(t)}, \tag{5.3}$$

$$c(t) = e^{\phi_{chirp}} = e^{j\frac{-2\pi v^2 t^2}{\lambda R_0}}. \tag{5.4}$$

As an example, the maximum window size will be calculated for the YSAR Israel Data case [8], i.e.,

$$\begin{aligned} sample\,rate &= sr = 400Hz \\ v &= 60m/s \\ \lambda &= .15m \\ azimuth\,spacing &= v/sr = .15m/sample. \end{aligned} \tag{5.5}$$

The frequency content of the chirp is the first derivative of the phase, given by

$$\dot{\phi}_{chirp} = \frac{4\pi v^2(t)}{R_0 \lambda} \leq sr. \tag{5.6}$$

The maximum allowable frequency is the Nyquist frequency which is determined by the sample rate. The data collected is complex so that the Nyquist frequency is equal to the sample rate. Solving for t and converting from radians to pixels gives

$$\begin{aligned} \dot{\phi}_{chirp} &\leq sr \\ t &\leq \frac{R_0 \lambda\, sr^2}{2v^2}\, samples = 1000\, pixels. \end{aligned} \tag{5.7}$$

This shows that for the YSAR Israel data, the maximum allowable image size is 1000 pixels.

5.1.2 Chirp Multiplication (Step 2)

Chapter 2 showed the spotlight and stripmap processing data models. The main difference between the stripmap and spotlight models is the band limiting in the stripmap equation caused by the antenna pattern. Using the same method as spotlight, the stripmap data may be compressed. The image vector consists of delta functions located at each scatterer's center point. Thus, the motion induced convolution between the delta functions and the chirp produces a chirp centered at each delta function. The compression method dechirps the image by correlating the chirp with the image. Let $g(t) = A\delta(t)e^{j\theta_A} + B\delta(t - t_2)e^{j\theta_B}$ represent two scatterers, one at the origin and one at t_2. The length of the $rect(t)$ is not included in the derivation because it is a constant in each range line with the only phase introduction given by its location.

$$a_{strip}(t) = [(A\delta(t)e^{j\theta_A} + B\delta(t - t_2)e^{j\theta_B}) \otimes c(t)rect(t)]e^{j\phi_e(t)} \otimes c^*(t)rect \tag{5.8}$$

A similar compression is achieved by selecting a section of range compressed data the length found in Eq. (5.7) and multiplying it by a chirp that is centered on the image. A derivation is as follows for the case of two scatterers A and B.

If we start with the initial range compressed data, each pixel is represented by the azimuth chirp associated with it and the phase error as,

$$r(t) = [g_n(t) \otimes c(t)rect]e^{j\phi_e(t)}. \tag{5.9}$$

Using the new SSC processing, a chirp the length derived in step 1 is multiplied point by point with range compressed data.

$$r(t) = [(A\delta(t)e^{j\theta_A} + B\delta(t-t_2)e^{j\theta_B}) \otimes c(t)rect(t)]e^{j\phi_e(t)}c^*(t) \tag{5.10}$$

Implementing the convolution and multiplication steps, the above equation reduces to

$$\begin{aligned}
r(t) &= [Ac(t)e^{j\theta_A}rect(t) + Bc(t-t_2)e^{j\theta_B}rect(t-t_2)]e^{j\phi_e(t)}c^*(t) \\
r(t) &= [Ae^{j\frac{-2\pi v^2(t)^2}{\lambda R}+\theta_A}rect(t) + Be^{j\frac{-j2\pi v^2(t-t_2)^2}{\lambda R}+\theta_B}rect(t-t_2)]e^{j\phi_e(t)}c^*(t) \\
r(t) &= [Ae^{j\frac{-2\pi v^2(t)^2}{\lambda R}+j\theta_A}rect(t) + Be^{j\frac{-2\pi v^2(t-t_2)^2}{\lambda R}+j\theta_B}rect(t-t_2)]e^{j\phi_e(t)}e^{j\frac{2\pi v^2(t)^2}{\lambda R}} \\
r(t) &= [Ae^{j\theta_A}rect(t) + Be^{j\frac{-2\pi v^2(t-t_2)^2}{\lambda R}+j\theta_B}e^{j\frac{2\pi v^2(t)^2}{\lambda R}}rect(t-t_2)]e^{j\phi_e(t)} \\
r(t) &= [Ae^{j\theta_A}rect(t) + Be^{j\frac{-2\pi v^2}{\lambda R}(2t_2t+t_2^2)+j\theta_B}rect(t-t_2)]e^{j\phi_e(t)} \\
r(t) &= [Ae^{j\theta_A}rect(t) + Be^{j\frac{-2\pi v^2 t_2^2}{\lambda R}+j\theta_B}e^{j\frac{-2\pi v^2}{\lambda R}(2t_2t)}rect(t-t_2)]e^{j\phi_e(t)}.
\end{aligned} \tag{5.11}$$

The above equation shows that the quadratic chirp has been replaced with a linear phase term with the accompanying constant corresponding to an azimuth position.

5.1.3 Fourier Transform (Step 3)

Equation (5.11) shows that the only t dependant phase terms are a linear term of the B scatterer and the phase error $\phi(t)$. From basic Fourier transform theory it can be seen that the $e^{j\frac{-2\pi v^2}{\lambda R}(2t_2t)}$ term will result in a shift in the frequency domain. Taking the Fourier transform of Eq. (5.11) results in,

$$a(t) = \mathcal{F}\{Ae^{j\theta_A}e^{j\phi_e(t)}rect(t) + Be^{jc_1t_2^2+\theta_B}e^{j(c_1 2t_2t)}e^{j\phi_e(t)}rect(t-t_2)\} \tag{5.12}$$

$$\begin{aligned}
a(t) &= Ae^{j\theta_A}sinc(\omega) \otimes e^{j\phi_e(\omega)} + Be^{jc_1t_2^2+\theta_B}sinc(\omega - 2c_1t_2)e^{(j\omega t_2)} \otimes e^{j\phi_e(\omega)} \\
c_1 &= \frac{-2\pi v^2}{\lambda R}.
\end{aligned} \tag{5.13}$$

The SSC compressed image will not necessarily map to the same pixel position as the stripmap compression. The mapping from the time domain to the frequency domain is dependent on many factors. The main determining factor is the constant c_1 which contains all the parameters of the SAR. The second factor is the size of the azimuth

section used. The discrete Fourier transform has a time frequency scale factor given by.

$$Frequency\,Scaling = FS = \frac{Sample\,Rate}{Total\,Length} = \frac{sr}{tl}. \tag{5.14}$$

The mapping from $2c_1t_2$ to pixel number in the frequency domain is

$$\begin{aligned} t_2\,seconds &= \frac{t_2}{sr}\,samples \\ 2c_1t_2 &= \frac{2\,v^2\,t_2\,tl}{\lambda\,R\,sr^2}\,pixels. \end{aligned} \tag{5.15}$$

Figure 5.3 shows the non-range dependant SSC steps. The original Fig. 5.2 image is reconstructed flawlessly with the non-range dependent chirp in Fig. 5.3. When the narrow beam assumption is not made, the image is distorted by the frequency scaling changing with range as seen in Fig. 5.4.

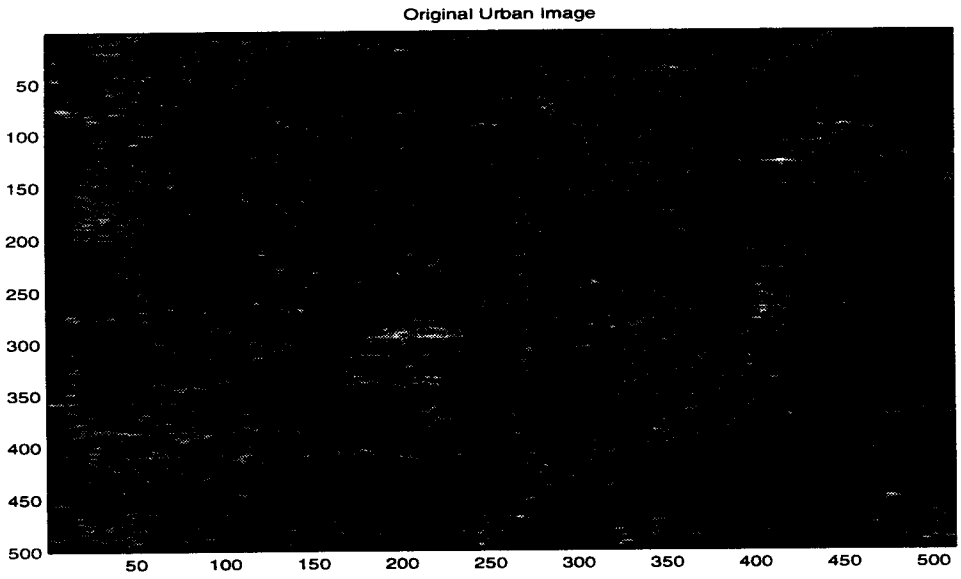

Figure 5.2: Original urban image with traditional stripmap compression method.

Using the SSC method with range dependent images creates a linearly decreasing mapping as can be observed in Eq. (5.15). This chirp distorts the image

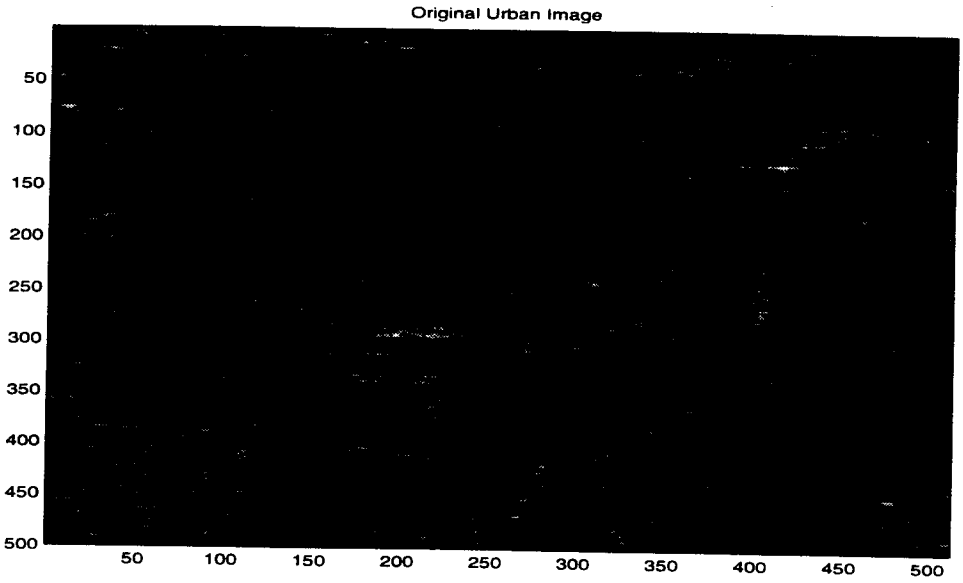

Figure 5.3: Non-range dependent chirp used in the stripmap SAR compressed with Strip-spot compression method.

as can be seen in Fig. 5.4. This distortion does not effect the PGA algorithm if the circular shift is adjusted to remove empty space. The distortion does cause a lower signal to clutter ratio, causing results to deteriorate slightly. Thus, the points, though compressed differently for different range lines, contain the same unaffected phase error.

5.2 Applying the PWE PGA

The PWE PGA may be applied to the range dependent, non-range dependent SSC compressed stripmap images by compensating for the changed space-frequency relationship of the farthest azimuth position. The total length of each azimuth line is shortened to its calculated size, and the circular shift is preformed. Zeros are then inserted in the high frequency sections to return the image to its original azimuth size. Figure 5.5 depicts the steps described above. The phase error estimation step is similar to the spotlight case, except that the mean is removed from the first derivative before integration to remove the linear term. The linear term causes discontinuities

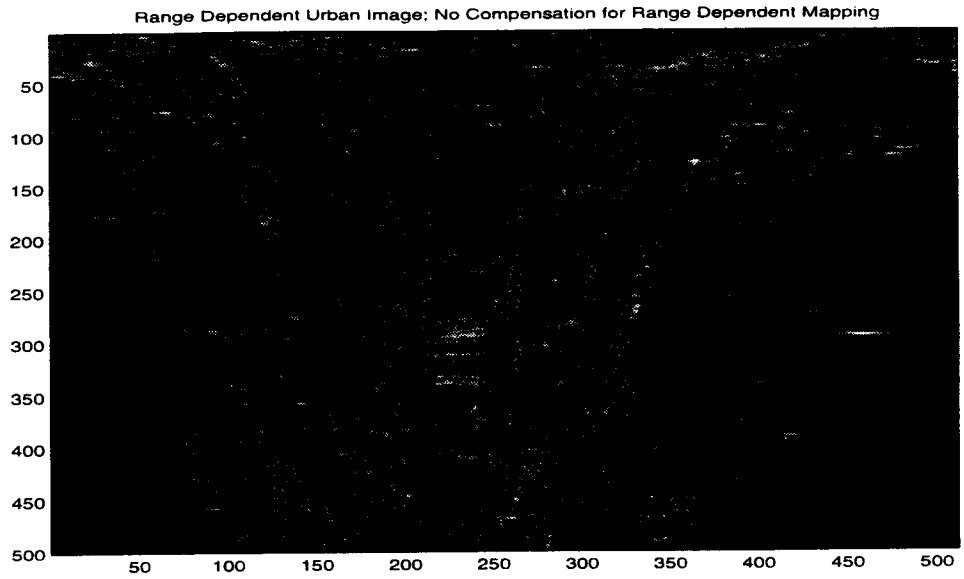

Figure 5.4: Range Dependent Chirp used in the Stripmap SAR compressed with Strip-spot compression method.

between the divided sections of the image. Figure 5.6 shows the effect of the removed mean.

5.3 Stripmap Results

The same images that were used in the Spotlight ML testing were used with the new strip-spot method. All three images were restored to their near original quality. The urban image had the highest signal to clutter ratio which gave the slightly better results then the other two images. The non-range dependent simulations compare the maximum likelihood estimation method with the PWE in stripmap images. These results are comparable with the results of the spotlight mode SAR. The PWE produced a lower standard deviation than the ML, but the ML converged faster.

In Figs. 5.9-5.12, 5.23-5.26, 5.37-5.40, and 5.49-5.52 the applied phase error is compared with the maximum likelihood and the phase weighted estimation. For these tests, the PWE has a final better convergence than the ML algorithm, but has a significantly slower convergence rate, requiring more iterations. The three images

are blurred with the range dependent phase error model derived in Eq. (4.8). Using the range dependent PWE, the errors are removed with the same accuracy as the non-range dependent spotlight maximum likelihood PGA. The estimated and applied phase errors for ϕ_x and ϕ_y are shown for the stripmap desert images in Figs. 5.13 through 5.20, the mountain images in 5.27 through 5.34 and for the urban images in 5.41 through 5.60. The ϕ_x and ϕ_y sometimes vary from the original error, but the combinations in the different range lines are accurate below one radian standard deviation.

The X and Y values in the range dependent cases were sometimes different then the respective error introduced because the pseudo inverse taken in the range dependent PWE does not give a unique solution. Three different range lines are presented as examples of the success of the algorithm. The three range lines are the closest distance, the middle distance and the farthest distance from the platform. The starting size of the window was determined by finding the calculated length of the shortest azimuth line in the image.

A high frequency phase error was applied to the urban image to test the high frequency estimation of the algorithm. The high frequency was estimated to the same accuracy as the low frequency phase errors shown in Figs. 5.49 through 5.60.

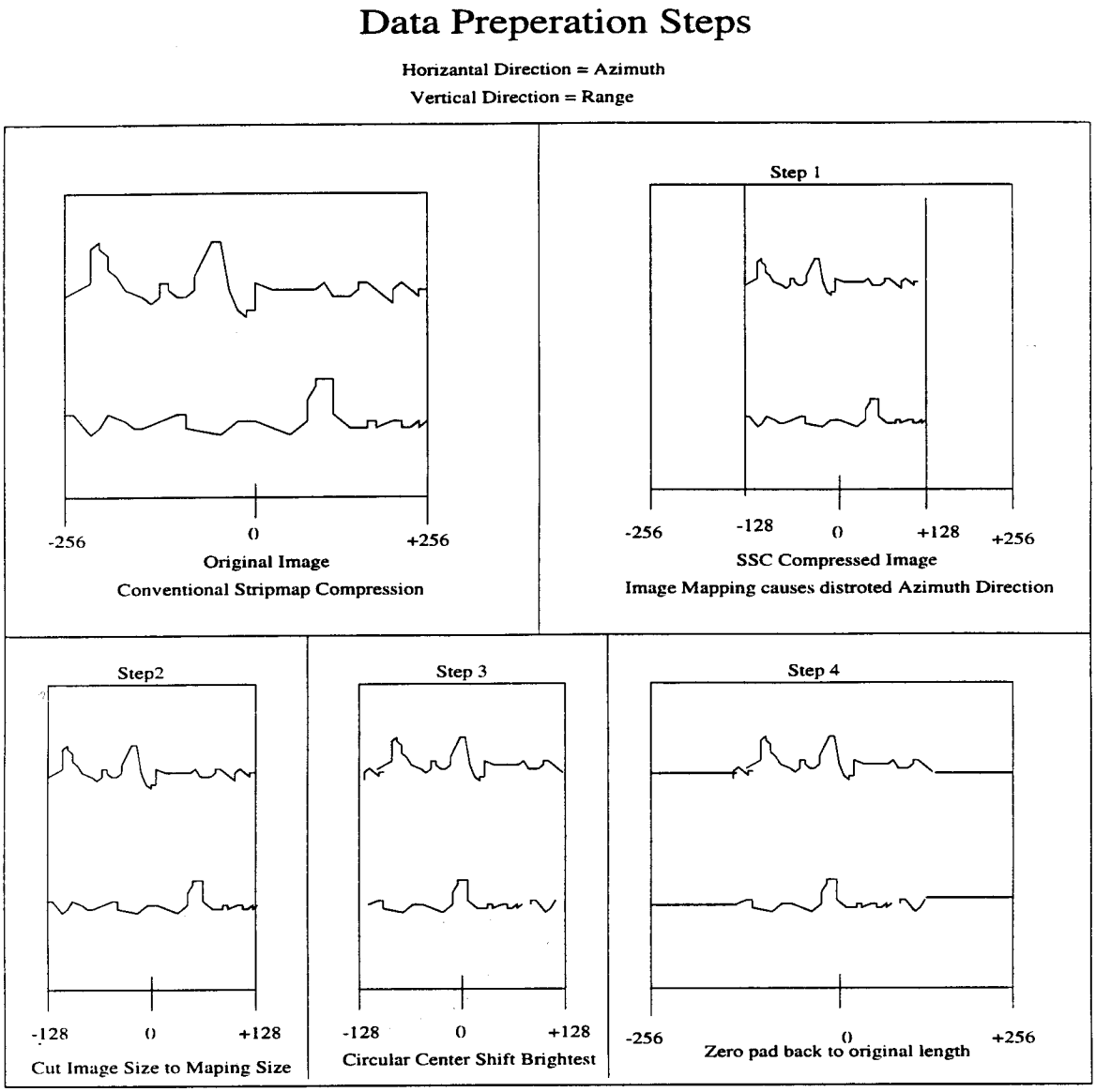

Figure 5.5: The steps of phase estimation. The PWE PGA may be applied to the range dependent or non-range dependent SSC compressed stripmap images by calculating the space-frequency relationship of the farthest azimuth position from the center for each range bin in the image. The total length of each azimuth line is shortened to its calculated size, and the circular shift is preformed. Zeros are then inserted in the high frequency sections to return the image to the original azimuth size. The first derivative estimation is take as discussed in the PWE or ML derivations with the mean removed before integration.

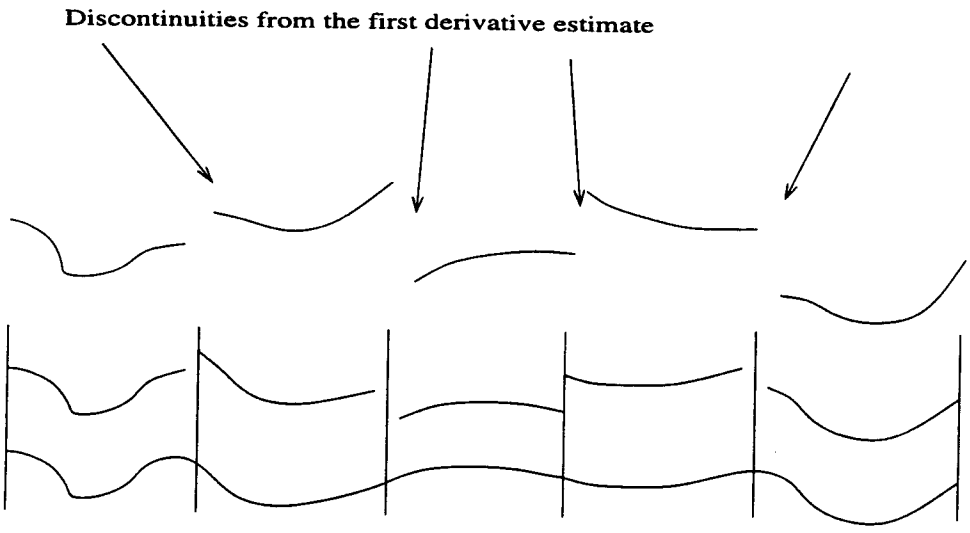

Figure 5.6: The discontinuities in the first derivative without removing the mean.

5.3.1 Desert Image: No Significant Scatterers

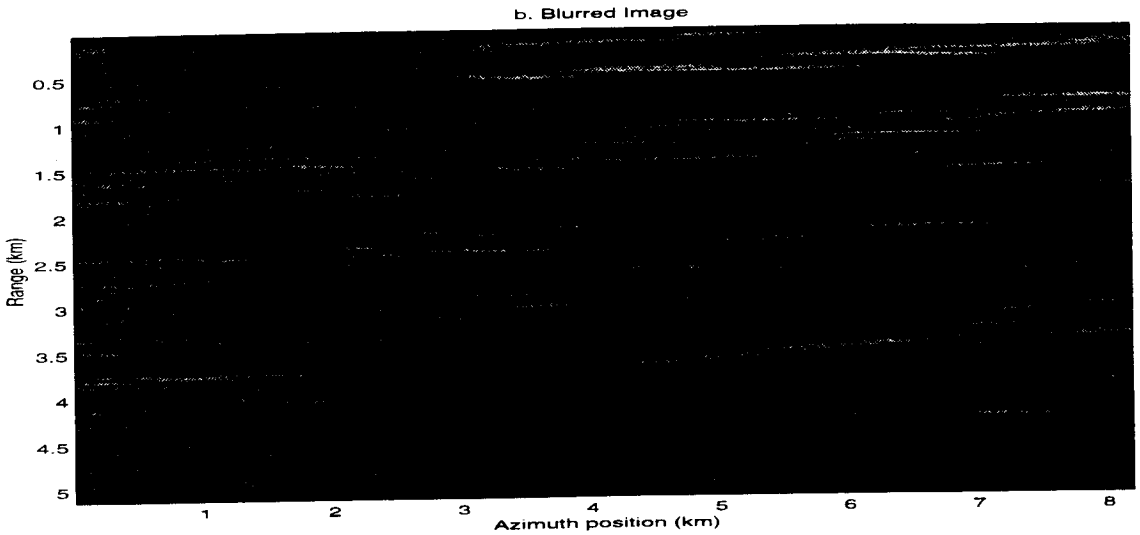

Figure 5.7: The phase corrupted desert image.

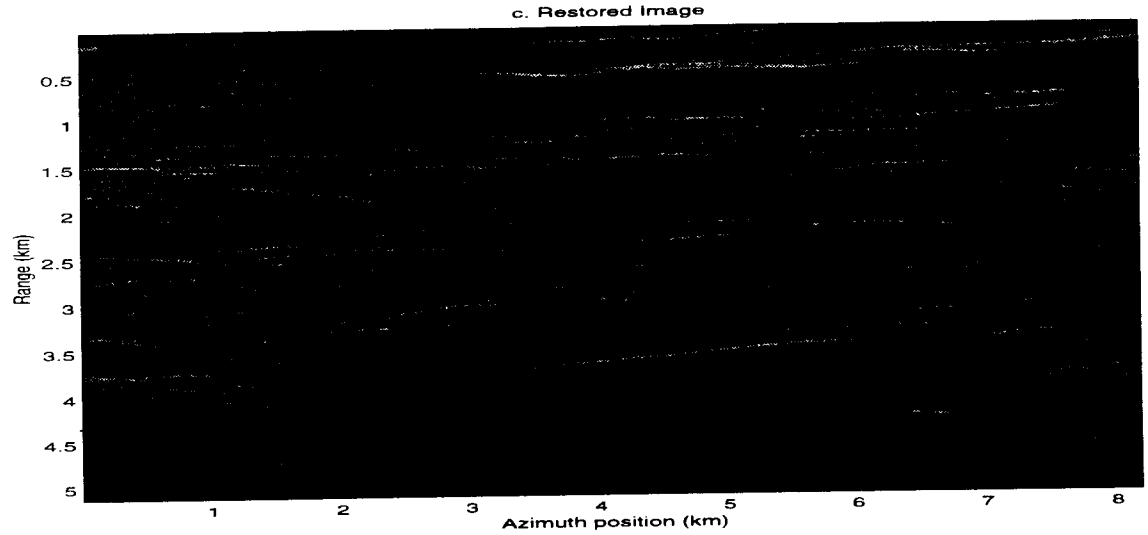

Figure 5.8: The restored desert image using the stripmap RD PWE PGA algorithm.

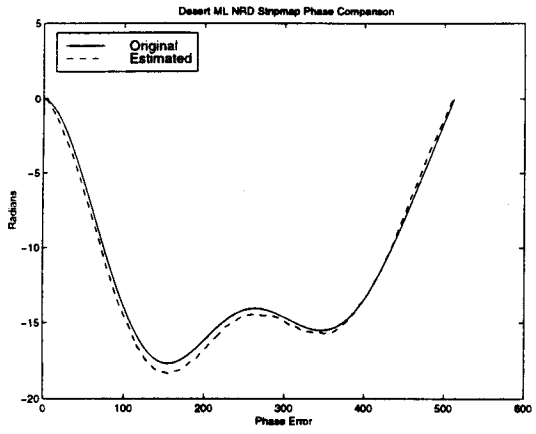

Figure 5.9: Phase error comparison. Non-range dependent ML stripmap desert image.

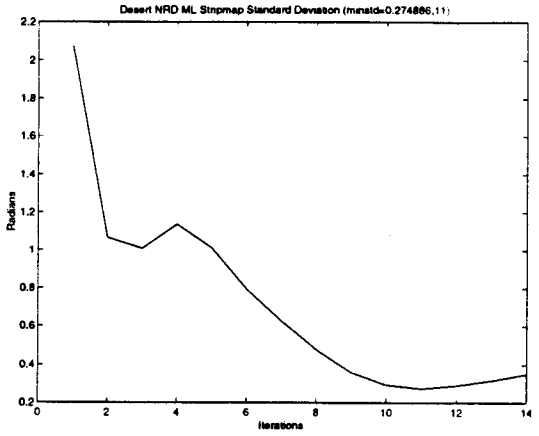

Figure 5.10: The standard deviation. Non-range dependent ML stripmap desert image.

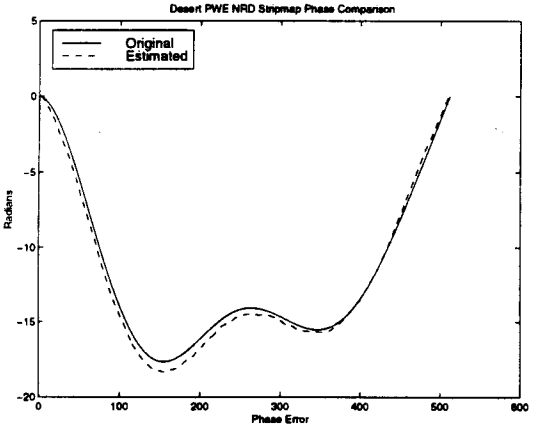

Figure 5.11: Phase error comparison. Non-range dependent PWE stripmap desert image.

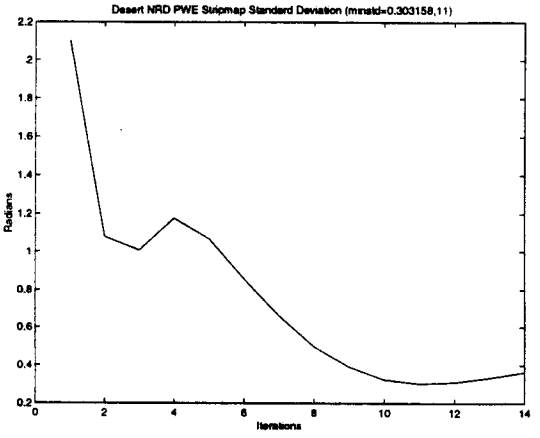

Figure 5.12: The standard deviation. Non-range dependent PWE stripmap desert image.

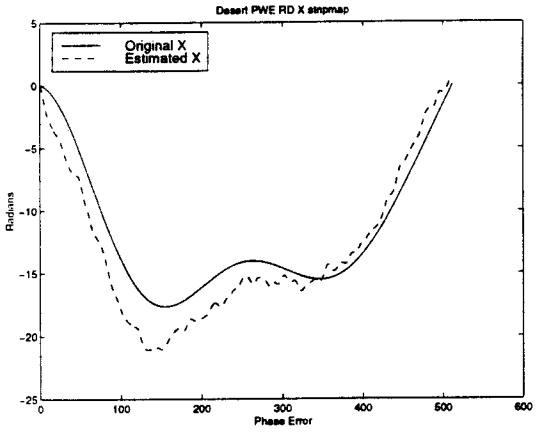

Figure 5.13: Phase error comparison X. Range dependent PWE stripmap desert image.

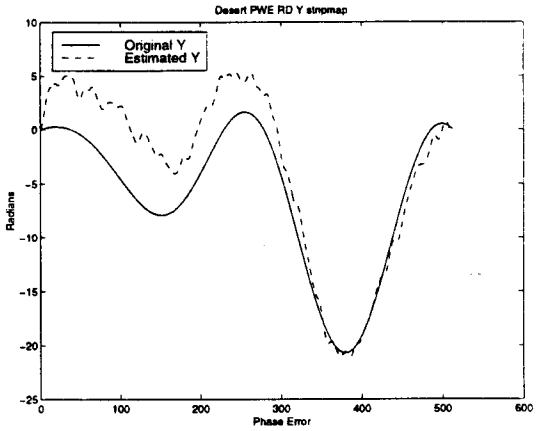

Figure 5.14: Phase error comparison Y. Range dependent PWE stripmap desert image.

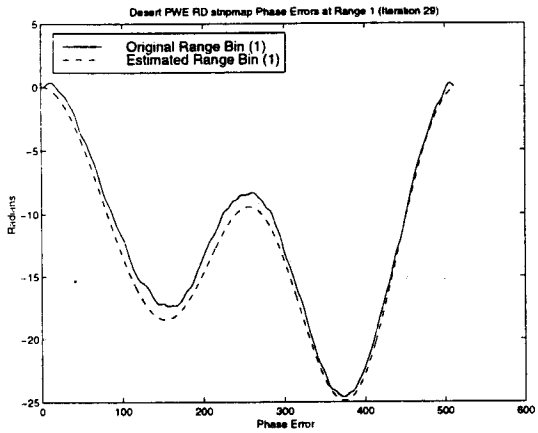

Figure 5.15: Phase error comparison. Range dependent PWE stripmap desert image. (Range Bin 1)

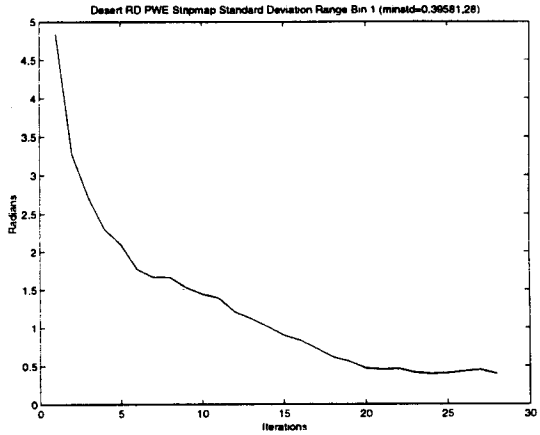

Figure 5.16: The standard deviation. Range dependent PWE stripmap desert image. (Range Bin 1)

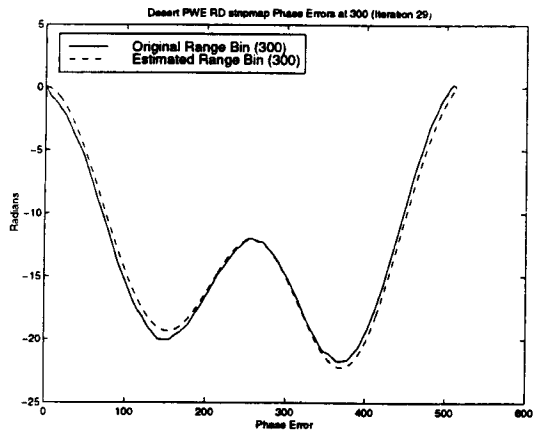

Figure 5.17: Phase error comparison. Range dependent PWE stripmap desert image. (Range Bin 300)

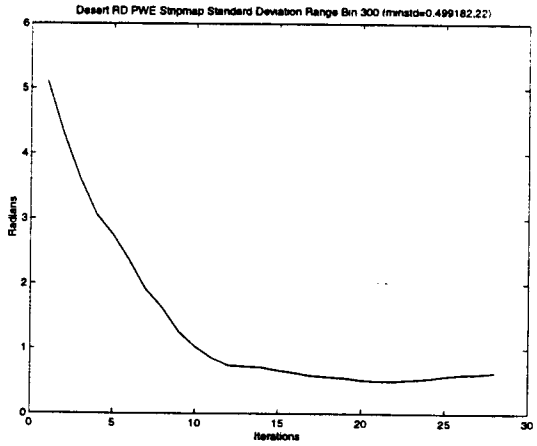

Figure 5.18: The standard deviation. Range dependent PWE stripmap desert image. (Range Bin 300)

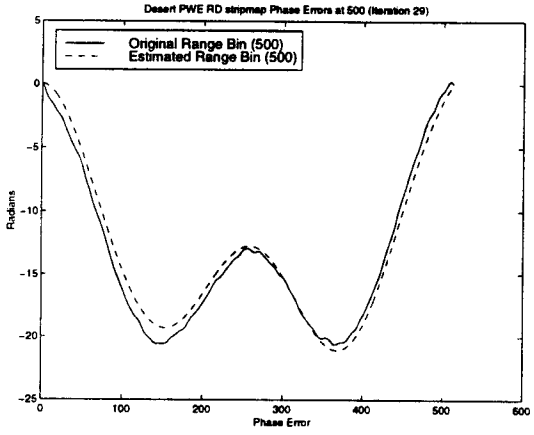

Figure 5.19: Phase error comparison. Range dependent PWE stripmap desert image. (Range Bin 500)

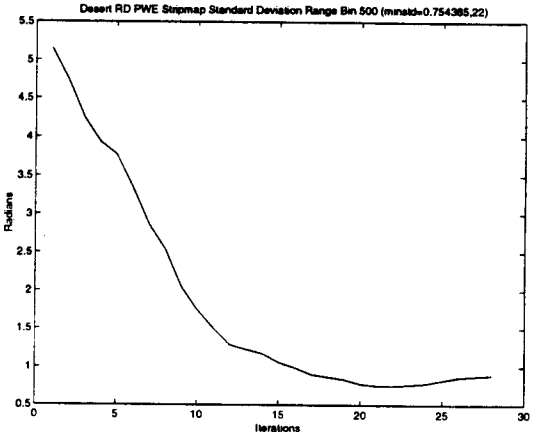

Figure 5.20: The standard deviation. Range dependent PWE stripmap desert image. (Range Bin 500)

5.3.2 Mountain Image: Some Significant Scatterers

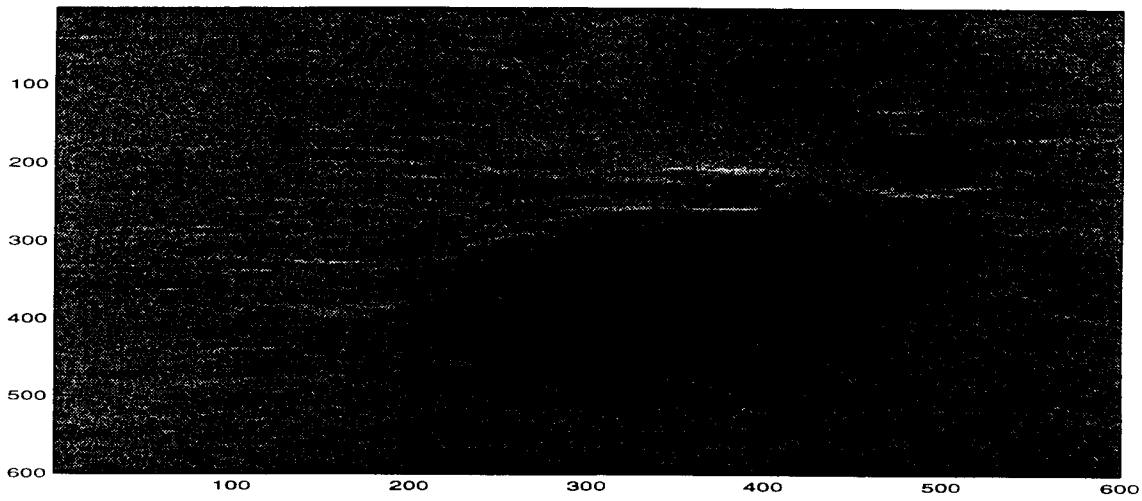

Figure 5.21: The phase corrupted mountain image.

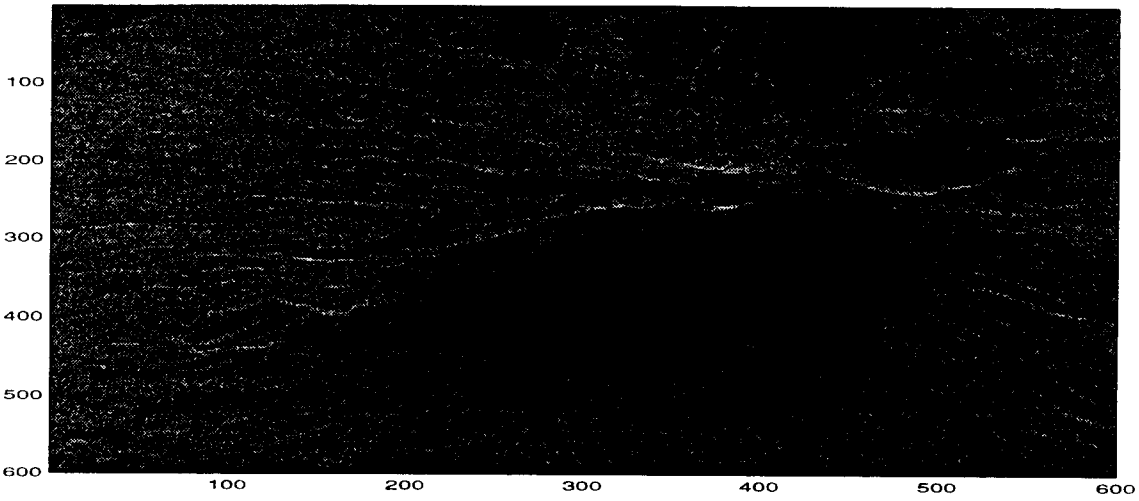

Figure 5.22: The restored mountain image using the Stripmap Range Dependent PWE PGA algorithm.

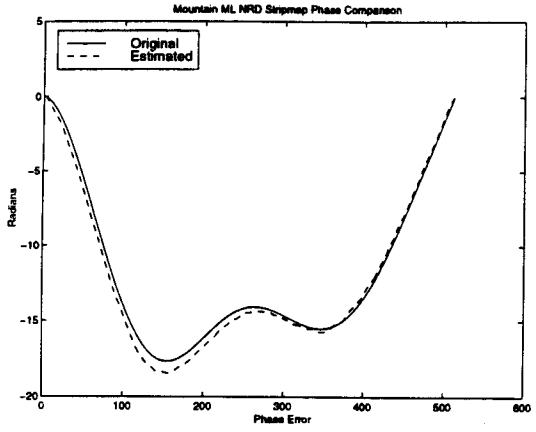

Figure 5.23: Phase error comparison. Non-range dependent ML stripmap mountain image.

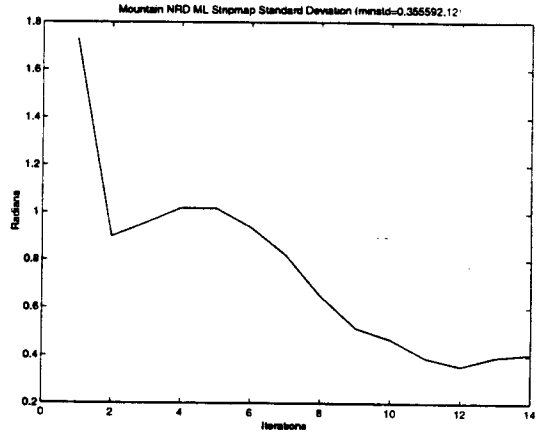

Figure 5.24: The standard deviation. Non-range dependent ML stripmap mountain image.

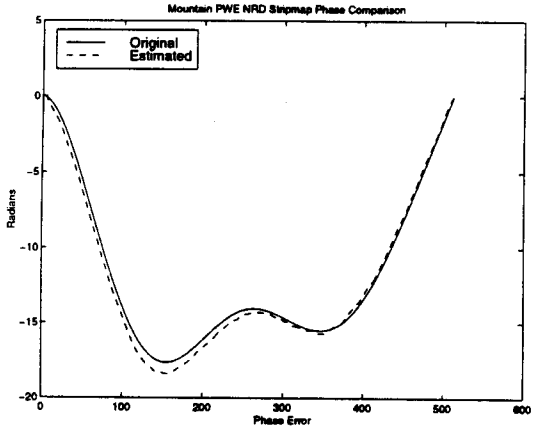

Figure 5.25: Phase error comparison. Non-range dependent PWE stripmap mountain image.

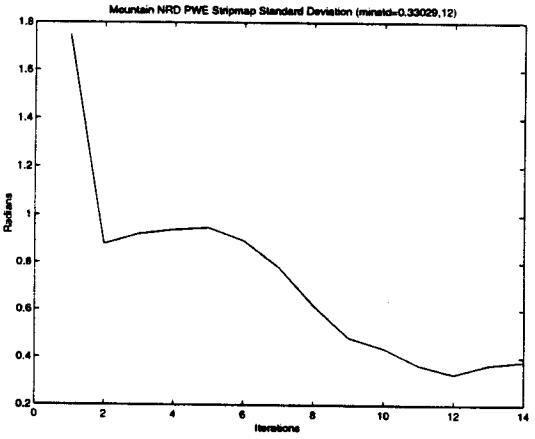

Figure 5.26: The standard deviation. Non-range dependent PWE stripmap mountain image.

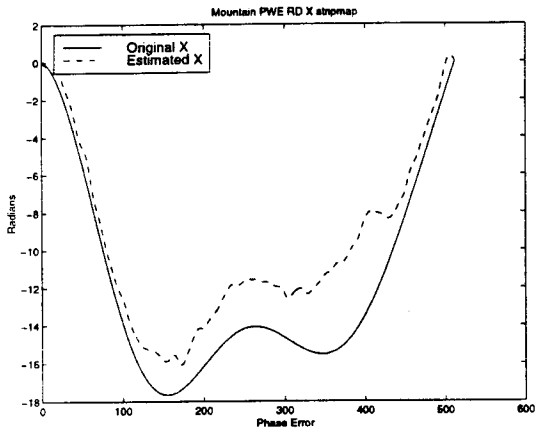

Figure 5.27: Phase error X comparison. Range dependent PWE stripmap mountain image.

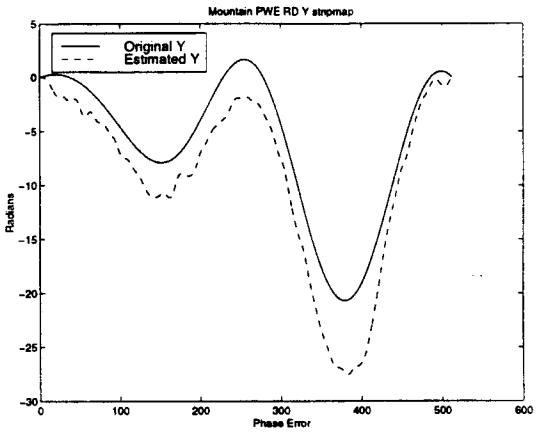

Figure 5.28: The error Y comparison. Range dependent PWE stripmap mountainimage.

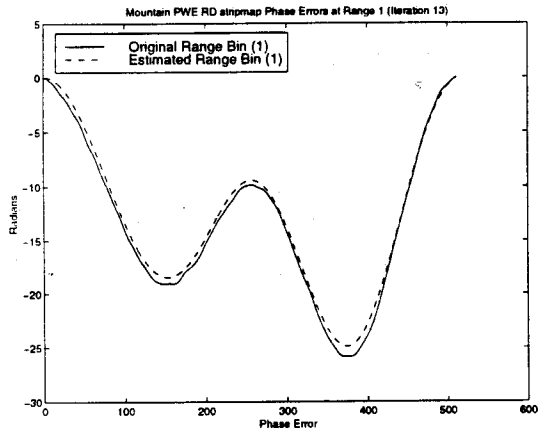

Figure 5.29: Phase error comparison. Range dependent PWE stripmap mountain image. (Range Bin 1)

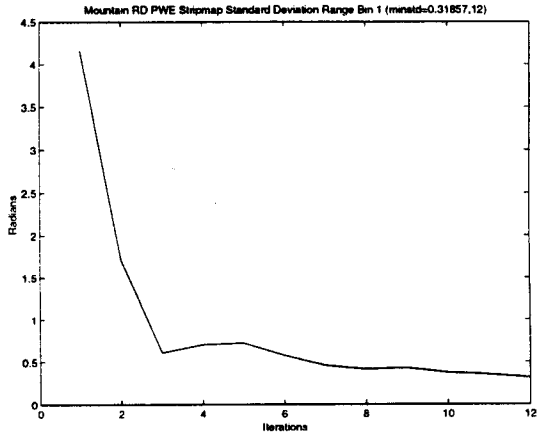

Figure 5.30: The standard deviation. Range dependent PWE stripmap mountain image. (Range Bin 1)

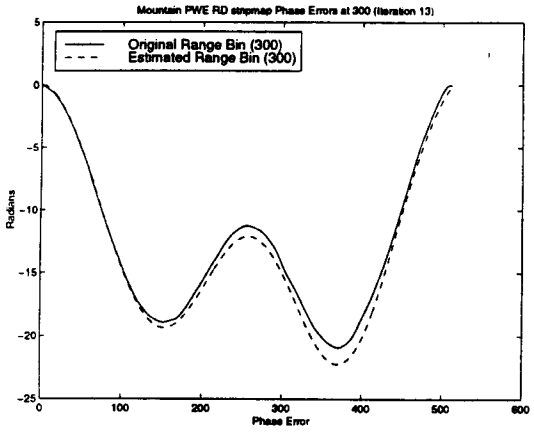

Figure 5.31: Phase error comparison. Range dependent PWE stripmap mountain image. (Range Bin 300)

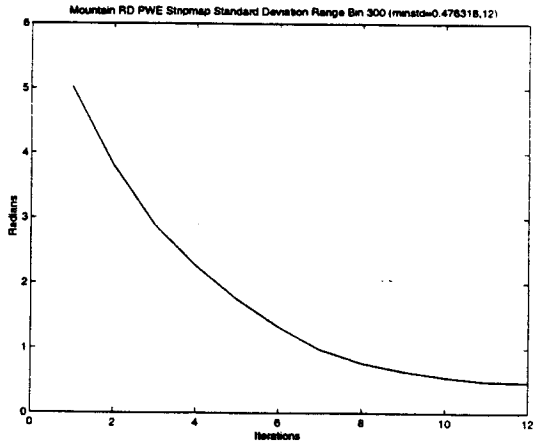

Figure 5.32: The standard deviation. Range dependent PWE stripmap mountain image. (Range Bin 300)

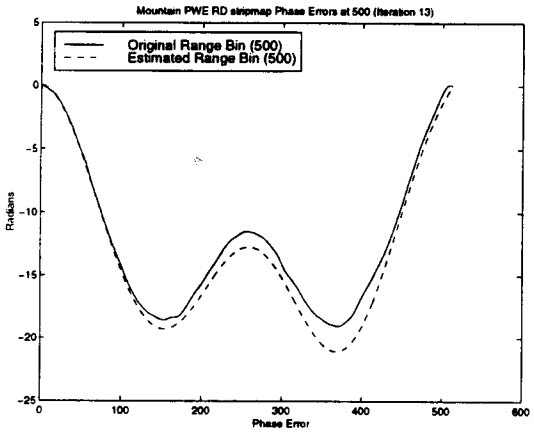

Figure 5.33: Phase error comparison. Range dependent PWE stripmap mountain image. (Range Bin 500)

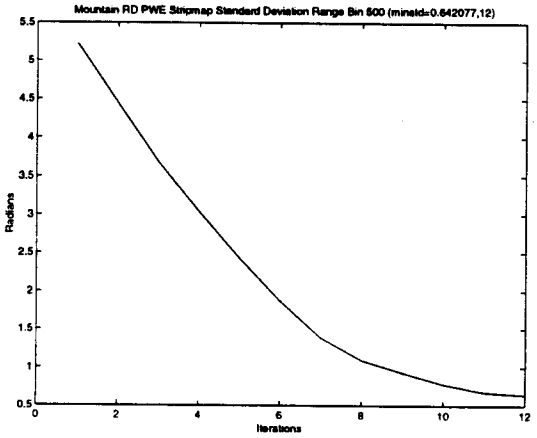

Figure 5.34: The standard deviation. Range dependent PWE stripmap mountain image. (Range Bin 500)

5.3.3 Urban Image: Many Significant Scatterers

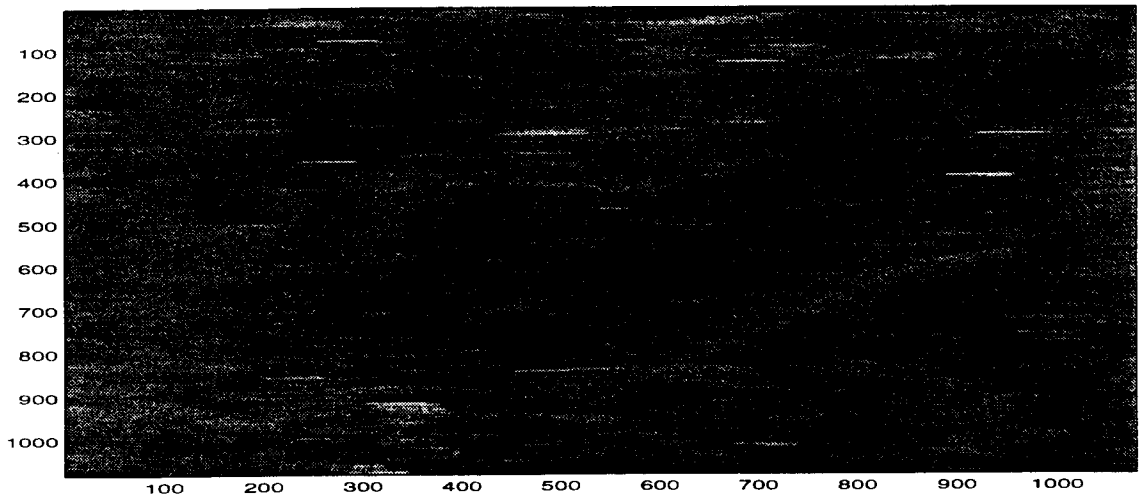

Figure 5.35: Blurred stripmap range dependent urban image.

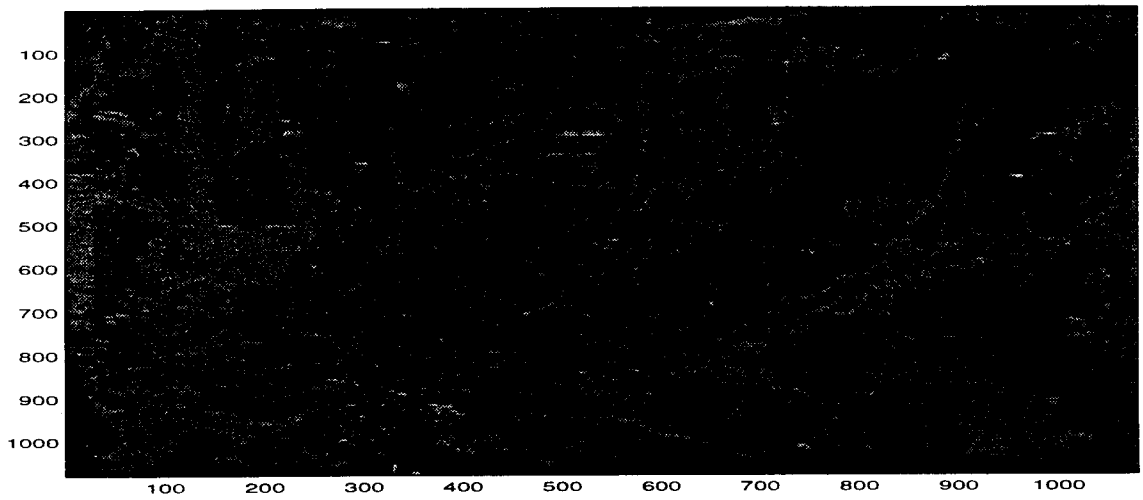

Figure 5.36: The restored urban image using the Stripmap Range Dependent PWE PGA algorithm.

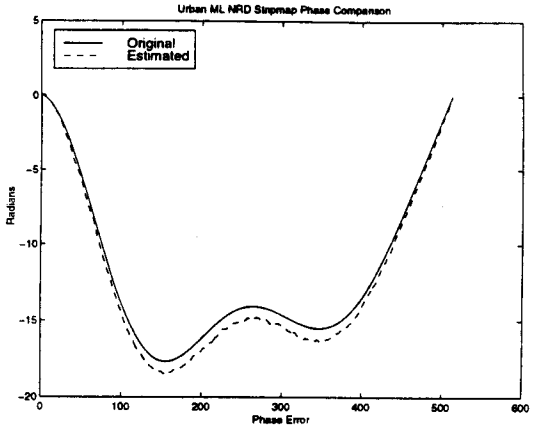

Figure 5.37: Phase error comparison. Non-range dependent ML stripmap Urban image.

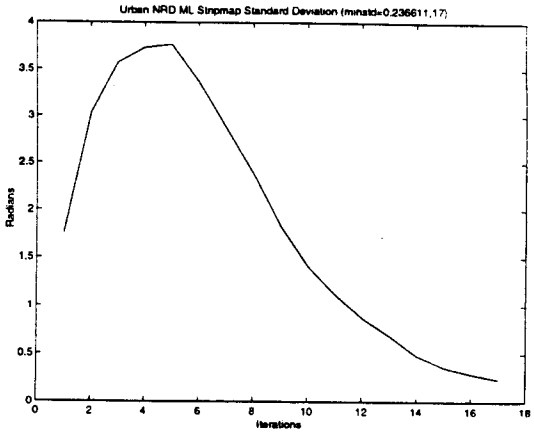

Figure 5.38: The standard deviation. Non-range dependent ML stripmap Urban image.

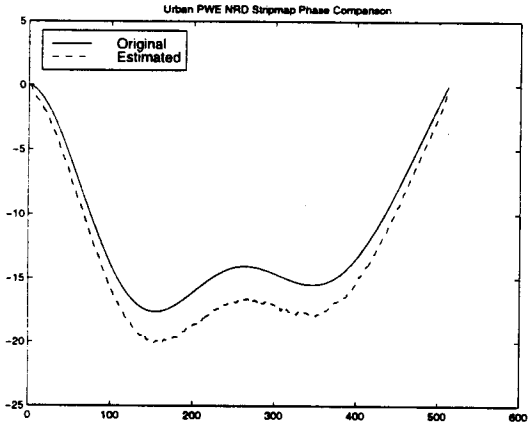

Figure 5.39: Phase error comparison. Non-range dependent PWE stripmap urban image.

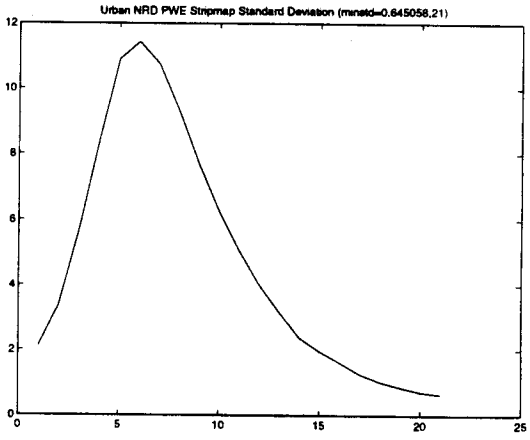

Figure 5.40: The standard deviation. Non-range dependent PWE stripmap urban image.

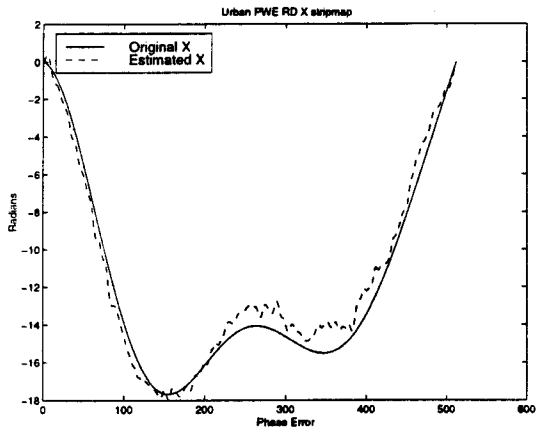

Figure 5.41: Phase error comparison X. Range dependent PWE stripmap urban image.

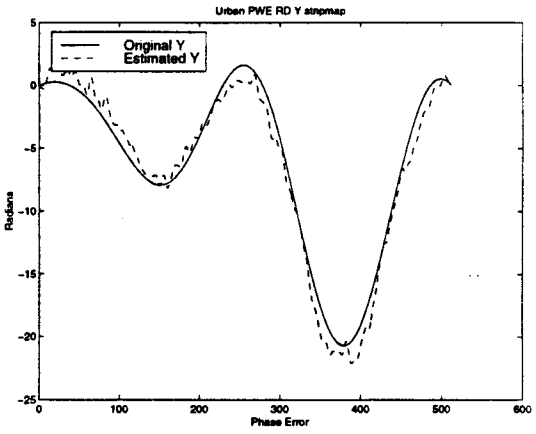

Figure 5.42: The error comparison Y. Range dependent PWE stripmap urban image.

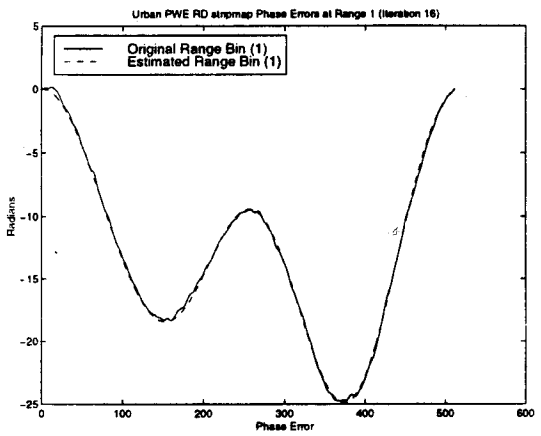

Figure 5.43: Phase error comparison. Range dependent PWE stripmap urban image. (Range Bin 1)

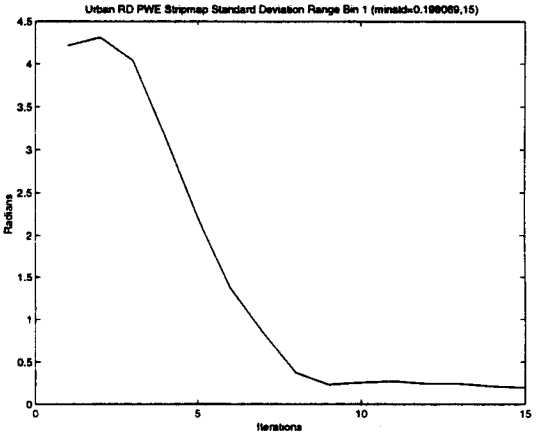

Figure 5.44: The standard deviation. Range dependent PWE stripmap urban image. (Range Bin 1)

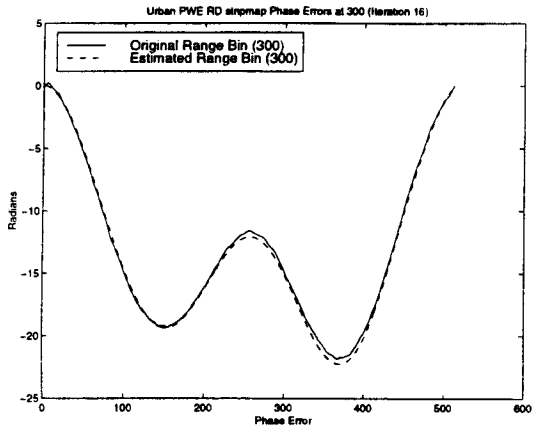

Figure 5.45: Phase error comparison. Range dependent PWE stripmap urban image. (Range Bin 300)

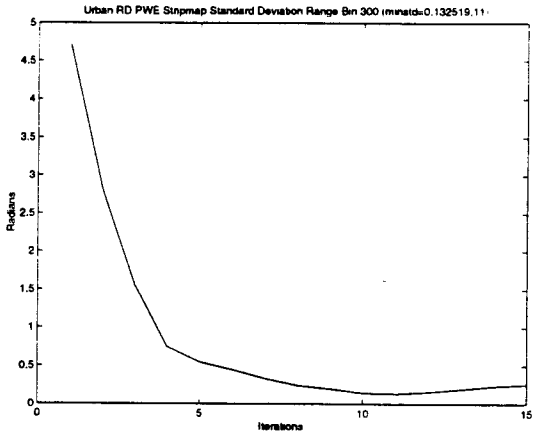

Figure 5.46: The standard deviation. Range dependent PWE stripmap urban image. (Range Bin 300)

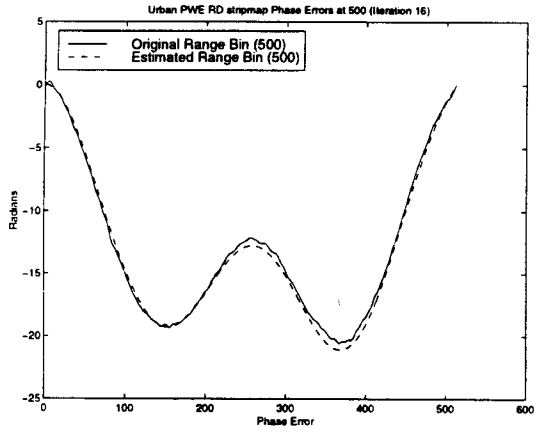

Figure 5.47: Phase error comparison. Range dependent PWE stripmap urban image. (Range Bin 500)

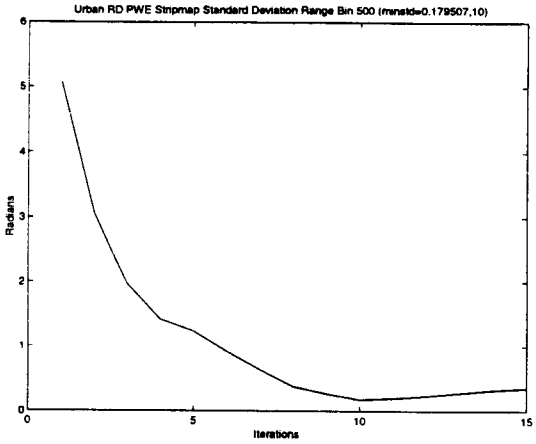

Figure 5.48: The standard deviation. Range dependent PWE stripmap urban image. (Range Bin 500)

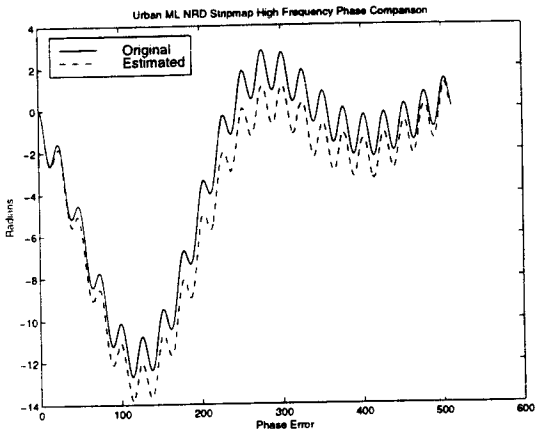

Figure 5.49: High frequency phase error comparison. Non-range dependent ML stripmap Urban image.

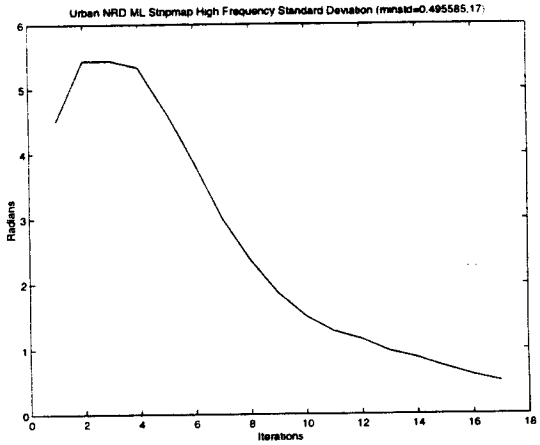

Figure 5.50: The standard deviation. Non-range dependent high frequency phase error ML stripmap Urban image.

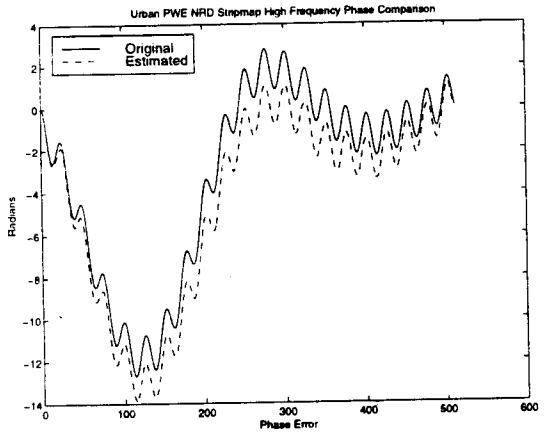

Figure 5.51: High frequency phase error comparison. Non-range dependent PWE stripmap urban image.

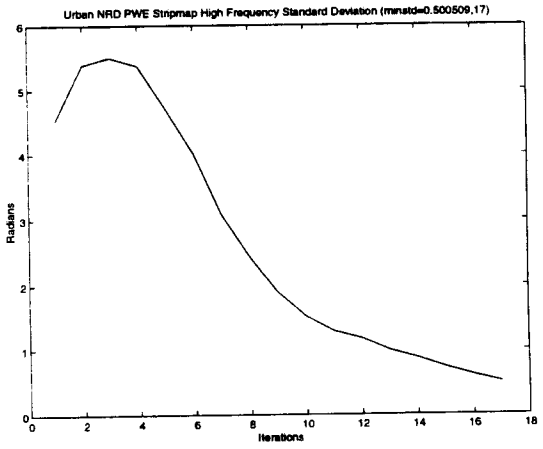

Figure 5.52: The standard deviation. Non-range dependent high frequency phase error PWE stripmap urban image.

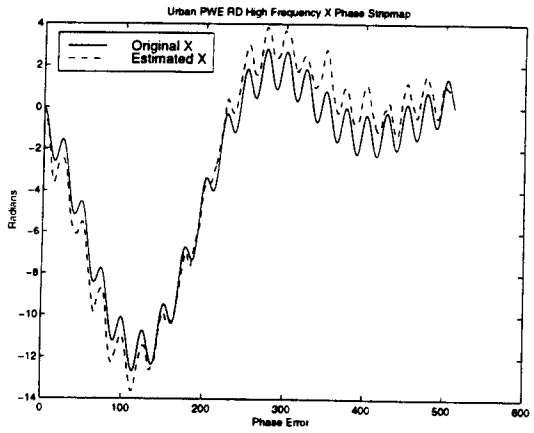

Figure 5.53: High frequency phase error comparison X. Range dependent PWE stripmap urban image.

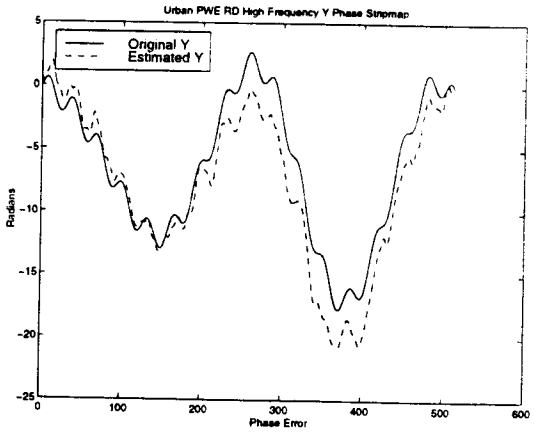

Figure 5.54: The error comparison Y. Range dependent high frequency phase error PWE stripmap urban image.

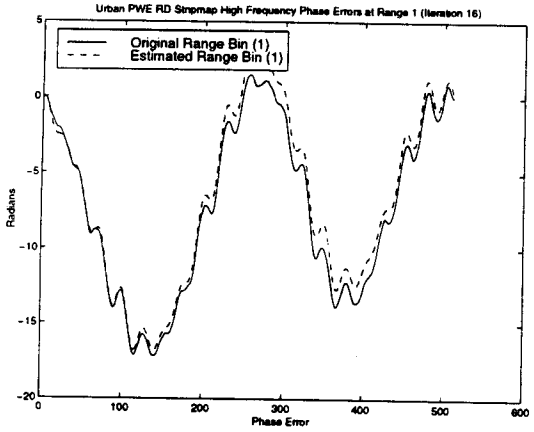

Figure 5.55: High frequency phase error comparison. Range dependent PWE stripmap urban image. (Range Bin 1)

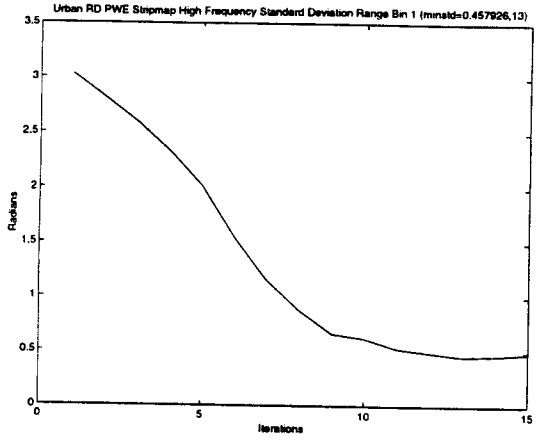

Figure 5.56: The standard deviation. Range dependent high frequency phase error PWE stripmap urban image. (Range Bin 1)

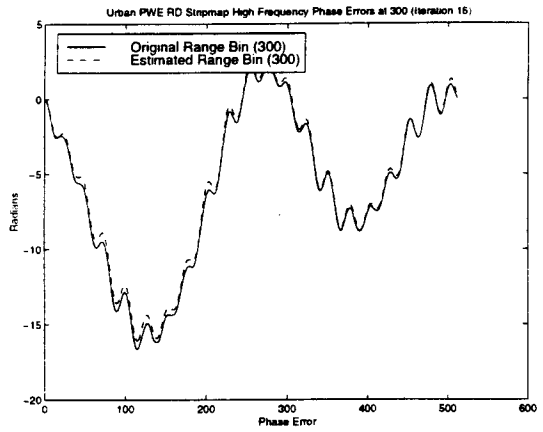

Figure 5.57: Phase error comparison. Range dependent high frequency phase error PWE stripmap urban image. (Range Bin 300)

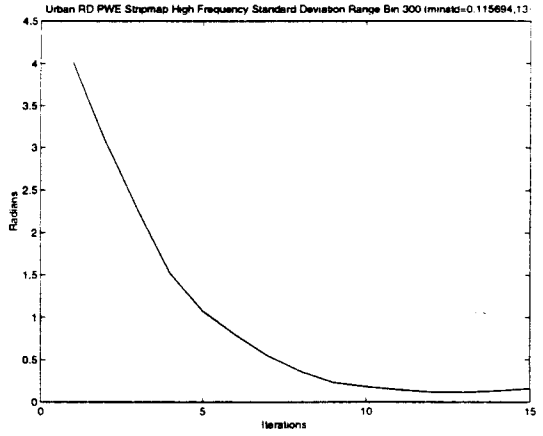

Figure 5.58: The standard deviation. Range dependent high frequency phase error PWE stripmap urban image. (Range Bin 300)

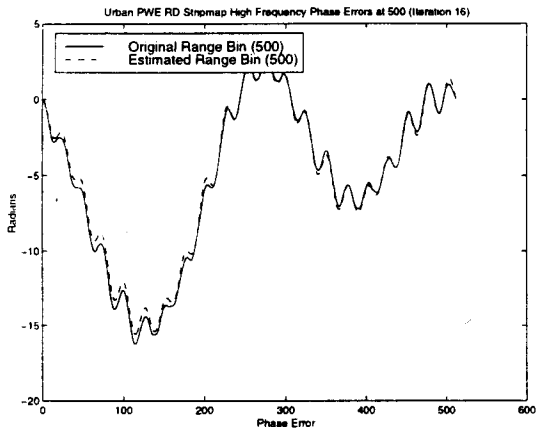

Figure 5.59: Phase error comparison. Range dependent high frequency phase error PWE stripmap urban image. (Range Bin 500)

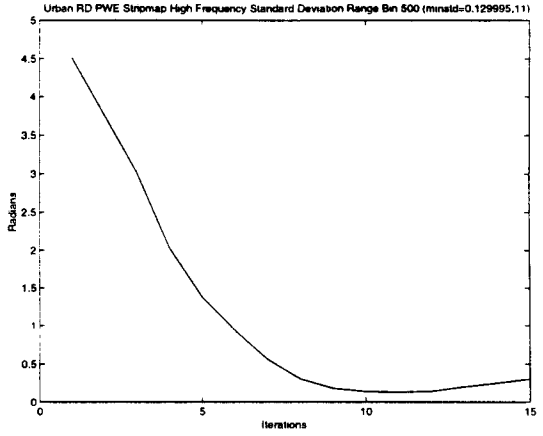

Figure 5.60: The standard deviation. Range dependent high frequency phase error PWE stripmap urban image. (Range Bin 500)

Chapter 6

Conclusions

The most successful spotlight SAR autofucus method is called the Phase Gradient Autofocus (PGA) Algorithm [4]. The term autofocus refers to the algorithms ability to focus the image with only the data itself. The Maximum Likelihood PGA (ML PGA) has been shown to be a very robust algorithm that works with both images having bright targets such as an urban setting and images such as a desert that has no significantly bright targets. The PGA does not require a phase error model estimation; therefore both high order and low order phase errors may be estimated accurately.

The four main steps in the PGA algorithm are all used in the range dependent stripmap model. The four steps defined are center shifting, windowing, phase estimation and iteration. The best known phase estimator for the noise model used in the PGA, is the Maximum Likelihood (ML) method [4]. The PGA assumes all phase and clutter noise as white Gaussian noise. This assumption seem seems to work well for most phase errors and images. The ML-PGA estimates the first difference of the phase.

6.1 Summary of Contributions

The PGA was designed for and has been used extensively in high flying spotlight aircraft. The PGA was not designed for low altitude systems because it makes a narrow beam assumption. The PGA was extended to range dependent systems by deriving a different phase gradient estimator called Phase Weighted Estimation-Phase Gradient Autofocus (PWE PGA). The gradient estimator named Phase Weighted

Estimation (PWE) surpasses the ML in the final standard deviation sense. In three different images, each testing the versatility of the algorithm through different image types, the PWE surpasses the ML in ten iterations. The ML converges, on the average, twice as fast as the PWE, but leveled out after 5 iterations. The PWE has been extended to the range dependent case. The results mentioned above have been repeated in this case. The PWE has worked extreamely well and has shown to be very versatile.

Stripmap images were compressed with a new strip-spot (SSC) algorithm technique. This processing creates a frequency-space relationship much like the original spotlight SAR processing. The new processing technique was successful for estimating phase errors in the stripmap images. When this algorithm was extended to range dependent stripmap, it was comparable to the earlier results only with high signal to clutter ratio images like the urban image. The PWE is capable of estimating high frequency and low frequency errors in both stripmap and spotlight mode.

6.2 Future Research

Israel images taken by YSAR [8] contain many problems for the PGA. These images need to be processed so that the new PWE stripmap PGA can be used with them. YSAR images were taken with the aircraft squinted. Compensation and effects of the squint on the YSAR data must be inspected. A detailed analysis of the edges of the images produces with the SSC algorithm is needed to know the exact effect of the blur caused by chirps cut short by the edge of the images. The bandlimited stripmap images contain an extra phase term. What effect do these phase terms have on the PGA. than the spotlight mode. An analysis on the best step size and starting and stopping points for maximum convergence in all images is needed.

Bibliography

[1] Walter G. Carrara, Ron S. Goodman, and Ronald M. Majewski, *Spotlight Synthetic Aperture Radar: Signal Processing Algorithms*, Artech House, Norwood, Massachussetts, 1995.

[2] Charles V. Jakowatz, Daniel E. Wahl, Paul H. Eichel, Dennis C. Ghiglia, and Paul A. Thompson, *Spotlight-mode Synthetic Aperture Radar: A signal processing approach*, Kluwer Academic Publishers, Norwell, Massachussetts, 1996.

[3] P. H. Eichel and Jr. C. V. Jakowatz, "Phase-gradient algorithm as an optimal estimator of the phase derivative", *Optics Letters*, vol. 14, no. 20, pp. 1101–1103, October 1989.

[4] Jr. Charles V. Jakowatz and Daniel E. Wahl, "Eigenvector method for maximum-likelihood estimation of phase errors in synthetic-aperture-radar imagery", *Journal of the Optical Society of America A*, vol. 10, no. 12, pp. 2539–2546, December 1993.

[5] D. E. Wahl, Jr. C. V. Jakowatz, and P. A. Thompson, "New approach to strip-map sar autofocus", in *Proceedings of the 1994 6th IEEE Digital Signal Processing Workshop*, Yosemite, CA, October 1994.

[6] D. W. Holcomb, "Shuttle imaging radar and archaeological survey in china's taklamakan desert", *Journal of Field Archaeology*, vol. 19, pp. 129–138, 1992.

[7] JR. David C. Munson and Robert L. Visentin, "A signal processing view of strip-mapping synthetic aperture radar", *IEEE Transactions on Acoustics, Speech, and Signal Processing*, pp. 2131–2141, 1989.

[8] D. G. Thompson, D. V. Arnold, D. G. Long, G. F. Miner, and T. W. Karlinsey. "Ysar: A compact, low-cost synthetic aperture radar", in *Proceedings of the 1996 International Geoscience and Remote Sensing Symposium*, Lincoln, Nebraska, May 1996, pp. 1892–1894.

[9] Lu YH Yeo TS, Tan NL and Zhang CB, "A stripmap to spotlight data converting algorithm", in *Proceedings of the 1997 International Geoscience and Remote Sensing Symposium*, Seatle, Aug 1998, pp. 1168–1170.

[10] M. Soumekh, "Digital spotlighting and coherent subaperture formation for stripmap synthetic aperture radar", *IEEE Transactions on Image Processing*, vol. 21, no. 12, pp. 476–480, December 1994.

[11] Adam Robertson, "Multi-Baseline SAR Interferometric Height Estimation", Master's thesis, Brigham Young University, Provo, Utah, 1998.

[12] Howard A. Zebker and Richard M Goldstein, "Topographic mapping from interferometric synthetic aperture radar observations", *Geophysical Research*, vol. 91, no. 15, pp. 4993–4999, April 1986.

[13] Dieter Just and Richard Balmer, "Phase statistics of interferograms with applications to synthetic aperture radar", *Applied Optics*, vol. 33, no. 20, pp. 4361–4368, July 1994.